TAMPEREEN TEKNILLINEN YLIOPISTO
TAMPERE UNIVERSITY OF TECHNOLOGY

Juha Tommila

Nanoscale Architecture for Site-controlled Epitaxy and Antireflective Coatings

Julkaisu 1159 • Publication 1159

Tampere 2013

Tampereen teknillinen yliopisto. Julkaisu 1159
Tampere University of Technology. Publication 1159

Juha Tommila

Nanoscale Architecture for Site-controlled Epitaxy and Antireflective Coatings

Thesis for the degree of Doctor of Science in Technology to be presented with due permission for public examination and criticism in Konetalo Building, Auditorium K1703, at Tampere University of Technology, on the 4th of October 2013, at 12 noon.

Tampereen teknillinen yliopisto - Tampere University of Technology
Tampere 2013

ISBN 978-952-15-3139-2 (printed)
ISBN 978-952-15-3150-7 (PDF)
ISSN 1459-2045

Abstract

The deployment of novel nanofabrication and -characterization techniques has paved the way for tunable functionalities of materials by engineering the size of the structures at the nanoscale. The key concepts in this thesis are the exploitation of quantum mechanical properties in nanostructures and sub-wavelength optical materials. This thesis covers nanoimprint lithography based fabrication techniques for the realization of quantum dot based semiconductor devices and the formation of sub-wavelength antireflection coatings for high efficiency solar cells. Both types of patterning processes were developed aiming for the integration with molecular beam epitaxy, which was used for the material fabrication. The structural and optical properties of the quantum dots fabricated by this new method indicated excellent suitability of the fabrication process for large scale quantum dot based devices.

The increasing demand of renewable energy sources has led to rapid development in the field of photovoltaics. In addition to the significant improvements in the preparation of active materials, the performance of a solar cell is directly increased by carefully designing the antireflection coating on the surface of the cell. The reflectivity of the solar cell surface has to be minimized in order to transfer the maximum amount of solar energy into the cell to be converted into electricity. In this thesis, a novel nanostructured antireflection coating was developed. The antireflective properties of the coating were outstanding within a broad spectral range and a clear increase in the solar cell performance was achieved.

Acknowledgments

The work presented in this thesis was carried out at the Optoelectronics Research Centre (ORC) at Tampere University of Technology (TUT) during the years 2009-2013. The research was funded by the Academy of Finland and the Finnish Funding Agency for Technology and Innovation (TEKES), to which I wish to express my gratitude. I would also like to thank the National Doctoral Programme in Nanoscience (NGS-NANO), the Pirkanmaa Regional Fund of the Finnish Cultural Foundation, the Industrial Research Fund at Tampere University of Technology (Tuula and Yrjö Neuvo fund), the Vilho, Yrjö and Kalle Väisälä Foundation, the Ulla Tuominen Foundation, the Jenny and Antti Wihuri Foundation, the Emil Aaltonen Foundation and the KAUTE Foundation for the financial support.

During the years at ORC I have had an honor to work with professionals in various fields related to photonics and received indispensable guidance and support. First, I wish to thank Prof. Tapio Niemi, my supervisor, for the guidance during my work. I would like to thank Prof. Emeritus Markus Pessa, the founder of ORC, and Dr. Pekka Savolainen, the current director of ORC, for the opportunity to work in this high-class, international research atmosphere. I express my gratitude to Prof. Mircea Guina for all the ideas, support and encouragement, and to Docent Mihail Dumitrescu, who conceived of the site-controlled quantum dot studies at ORC. I am grateful to Dr. Jukka Viheriälä for the supervision and dedicated guidance in the beginning of my research career and particularly in nanoimprint lithography related tasks. Without the colleagues working with nanoimprint lithography, Tuomo Rytkönen, Juha Kontio and Milla-Riina Viljanen, the development of the fabrication techniques used in this thesis would have been impossible. I greatly acknowledge the recently founded quantum dot team, Dr. Andreas Schramm and Teemu Hakkarainen for the huge amount of growth experiments presented in this thesis and all the shared ideas and fruitful discussions. I am very grateful to the solar cell team, Dr. Antti Tukiainen, Arto Aho – to whom I wish to express my gratitude also for the

fundamental studies related to quantum dots – Ville Polojärvi and Joel Salmi, who prepared the materials for the solar cells presented in this thesis and helped in the characterization. I wish to thank Tobias Kibb and Christian Strelow from University of Hamburg, Germany, for the optical measurements of the quantum dots. I would like to thank Esa Heinonen from University of Oulu for the precise focused ion beam processing. I am grateful to Ilkka Hirvonen and Bengt Holmström for the upkeep and help in maintenance of the research equipment. I am grateful to Maija Karjalainen and Mariia Bister for the aid in cleanroom activities, and to Anne Viherkoski and Eija Heliniemi for the great assistance in administrative issues.

I wish to thank Prof. Changsi Peng and Chunlei Tan for all the arrangements during my research visit to Soochow University, China, and Xiaofeng Yuan, Soochow University, China and Yuxiang Zhang, Chinese Academy of Sciences, China, for their help in laser interference lithography experiments. I want to thank Wei Zhang, Soochow University, China for the help in μPL measurements.

Many thanks goes to my friends, who have provided me valuable counterbalance to the work and studies, and teammates in Hiisirasti for pushing me into the limits also far away from work and the memorable events shared in Jukola relays.

Finally, I want to express my deepest gratitude to my family, especially to my beloved wife Heidi and our wonderful son Lassi for all the delight and support.

Tampere, September 2013
Juha Tommila

Table of Contents

List of Publications

The following publications are included in this thesis as appendices and in the text they are referred to as [P1] – [P6].

[P1] J. Tommila, A. Tukiainen, J. Viheriälä, A. Schramm, T. Hakkarainen, A. Aho, P. Stenberg, M. Dumitrescu and M. Guina, "Nanoimprint lithography patterned GaAs templates for site-controlled InAs quantum dots," *Journal of Crystal Growth*, vol. 323, no. 1, pp. 183-186, 2011.

[P2] J. Tommila, A. Schramm, T. V. Hakkarainen, M. Dumitrescu, and M. Guina, "Size-dependent properties of single InAs quantum dots grown in nanoimprint lithography patterned GaAs pits," *Nanotechnology*, vol. 24, 235204 (5pp), 2013.

[P3] J. Tommila, C. Strelow, A. Schramm, T. V. Hakkarainen, M. Dumitrescu, T. Kipp and M. Guina, "The influence of temperature on the photoluminescence properties of single InAs quantum dots grown on patterned GaAs," *Nanoscale Research Letters*, vol. 7, no. 313, pp. 1-4, 2012.

[P4] A. Schramm, J. Tommila, C. Sterlow, T.V. Hakkarainen, A. Tukiainen, M. Dumitrescu, A. Mews, T. Kipp and M. Guina, "Large array of single, site-controlled InAs quantum dots fabricated by UV-nanoimprint lithography and molecular beam epitaxy," *Nanotechnology*, vol. 23, 175701 (4pp), 2012

[P5] J. Tommila, V. Polojärvi, A. Aho, A. Tukiainen, J. Viheriälä, J. Salmi, A. Schramm, J. M. Kontio, A. Turtiainen, T. Niemi and M. Guina, "Nanostructured broadband antireflection coatings on AlInP fabricated by nanoimprint lithography," *Solar Energy Materials and Solar Cells*, vol. 94, no. 10, pp. 1845-1848, 2010.

[P6] J. Tommila, A. Aho, A. Tukiainen, V. Polojärvi, J. Salmi, T. Niemi and M. Guina, "Moth-eye antireflection coating fabricated by nanoimprint lithography on 1 eV dilute nitride solar cell," *Progress in Photovoltaics: Research and Applications*, vol. 21, no. 5, pp. 1158–1162, 2013.

Author's Contribution

This thesis is a compilation of six research articles published in international peer-reviewed journals. The thesis also includes minor parts from other supplementary publications, which are included in the bibliography, as well as some unpublished results. The author has played a key role in designing the experiments, preparing the samples, characterizing them and writing the publications. However, the results presented in this thesis are the outcome of organized teamwork. The main aspects provided by the coworkers listed in the publications, include semiconductor growths, measurement system preparations and numerical simulations.

In [P1], the author developed the surface cleaning processes and related nanoimprint lithography patterning processes, and performed the surface studies and ensemble photoluminescence measurements. In [P2], the author designed the structure, performed nanoimprint lithography patterning and measured the structural and optical properties of the quantum dots. In [P3] and [P4], the author carried out nanoimprint lithography patterning and participated in design and data analysis.

In [P5] and [P6], the author designed the fabrication processes for the antireflection structures, manufactured them, and performed the reflectivity, photoluminescence and structural measurements as well as the main part of the numerical simulations. In [P1], [P2], [P3], [P5] and [P6] the author drafted the manuscripts as the corresponding author and in [P4] the author took part in the preparation of the manuscript as a co-author.

List of Abbreviations and Symbols

AlGaAs	Aluminum gallium arsenide
AlInP	Aluminum indium phosphide
AFM	Atomic force microscopy
CCD	Charge-coupled device
CVD	Chemical vapor deposition
DBR	Distributed Bragg reflector
DVD	Digital versatile disk
EBL	Electron beam lithography
FDTD	Finite-difference time-domain method
FIB	Focused ion beam lithography
FSS	Fine-structure splitting
GaAs	Gallium arsenide
GaInAsN	Gallium indium arsenide nitride
GaInP	Gallium indium phosphide
IC	Integrated circuit
ICP-RIE	Inductively coupled plasma reactive ion etching
InAs	Indium arsenide
InGaAs	Indium gallium arsenide
InP	Indium phosphide
LIL	Laser interference lithography
MBE	Molecular beam epitaxy
ML	Monolayer
MOVPE	Metalorganic vapor phase epitaxy
NIL	Nanoimprint lithography
ORC	Optoelectronics Research Centre

PDMS	Polydimethylsiloxane
PET	Polyethylene terephthalate
PECVD	Plasma-enhanced chemical vapor deposition
PhC	Photonic crystal
PL	Photoluminescence
µPL	Micrometer scale photoluminescence measurement
PVD	Physical vapor deposition
QD	Quantum dot
QW	Quantum well
R2PNIL	Roll-to-plate NIL
R2RNIL	Roll-to-roll NIL
RIE	Reactive ion etching
SAG	Selective area growth
SAQD	Self-assembled quantum dot
SCQD	Site-controlled quantum dot
SEM	Scanning electron microscopy
S-FIL	Step and flash imprint lithography
SK	Stranski-Krastanov growth mode
SPM	Scanning probe lithography
S-SIL	Step and stamp imprint lithography
STM	Scanning tunneling microscopy
TEM	Tunneling electron microscopy
UV	Ultraviolet
UV-NIL	Ultraviolet nanoimprint lithography
WL	Wetting layer

Symbols

α	Fitting parameter
α_{laser}	Absorption coefficient for incident laser
α_{PL}	Absorption coefficient for GaAs PL
β	Fitting parameter

E_g	Band gap energy
E_0	Band gap energy at 0 K
g(Energy)	Density of states
h	Planck's constant
$I_{PL}^{eq}(\lambda)$	Equalized PL intensity
$I_{PL}^{meas}(\lambda)$	Measured PL intensity
k_1	Process constant
$\kappa(\lambda)$	Extinction coefficient
λ	Wavelength of light
M_{if}	Optical matrix element
R	Lateral resolution
R_{laser}	Surface reflectivity at laser wavelength
$R(\lambda)$	Wavelength dependent surface reflectivity
T	Temperature
W_{if}	Transition rate between initial and final states
x	Effective thickness of the AlInP layer

Chapter 1

1 Introduction

The increase in machining accuracy has paved the way for the development of manufacturing via microfabrication to the advent of nanotechnology. In 1959 Richard Feynman gave a lecture titled “There’s Plenty of Room at the Bottom” [1], which is often referred to as a revolutionary event in the history of nanotechnology. Nanotechnology is described to cover all the fields where structures are controlled within the scale of 1 - 100 nm, and novel properties appear because of the small size [2]. As the fabrication and characterization technologies have developed rapidly during the past decades, it has become possible to manipulate materials at the nanoscale. This brings out new functionalities such as exploitation of quantum mechanical properties and sub-wavelength optical materials. Fabrication of nanostructures is realized by various types of high resolution nanolithography techniques such as nanoimprint lithography (NIL), which has gained enormous interest within the scientific community and industry since its introduction in 1995 [3]. It was chosen among the “10 Emerging Technologies That Will Change the World” in Massachusetts Institute of Technology technology review [4] and it has been included in the international technology roadmap of semiconductors as a candidate for 22 nm and 16 nm half-pitch nodes [5]. Fabrication of 2 nm structures and a very high throughput has been demonstrated by nanoimprint lithography [6-8]. In this thesis, NIL based patterning processes are utilized in quantum dot (QD) fabrication and in the formation of sub-wavelength antireflection coatings for high efficiency solar cells. Both types of patterning processes were developed aiming towards the integration with molecular beam epitaxy (MBE), which was used for the material fabrication. Material deposition was controlled with atomic layer precision by MBE.

Observation of quantum-size effects in III-V semiconductors in the 1970's led to the demonstration of first quantum well (QW) laser in 1975 [9]. QW lasers exploit quantum confinement in one dimension. Since then quantum phenomena in 2D and 3D semiconductor structures have been studied extensively. Semiconductor quantum dots exhibit a strong 3D confinement for electrons and holes causing atomic like properties, which can be adjusted in the fabrication process. Although having sizes up to a couple of tens of nanometers, the carriers can be strongly confined in all directions because of the relatively large Bohr radius. The Bohr radius of an electron-hole pair, i.e. exciton, in a typical Indium Arsenide (InAs) QD is in the order of 30 nm [10]. QDs offer an attractive platform for the future quantum information technology platforms because their fabrication can be integrated into well-established semiconductor fabrication processes. Most of the demonstrations based on single QDs have been performed with QDs which were randomly positioned on the surface of a semiconductor wafer. However, it is obvious that for device integration, the QD position has to be controlled.

Solar energy harvesting and especially the field of photovoltaics have drawn a lot of interest lately because of the environmental concerns and requests for renewable energy sources. The development of high efficiency solar cells has lifted the conversion efficiencies of multijunction III-V solar cells up to 44 % [11]. These solar cells operate within a wide absorption spectrum ranging from 300 nm to beyond 1800 nm. Wide operation range sets demanding requirements for the antireflection coating on the solar cell surface. Because of the high discontinuity of the refractive index from air to the semiconductor, the reflectivity of the uncoated solar cell surface is in the order of 30 %. The reflectivity of the solar cell surface has to be minimized in order to transfer the maximum amount of solar energy into the cell to be converted into electricity. Nanostructured antireflection surfaces can be tailored to gradually convert the refractive index from air to semiconductor, and thus efficiently reduce the amount of reflected light. They have wider spectral bandwidth with larger incident angle than regular thin-film coatings.

1.1 Motivation and aim of this thesis

This thesis is a combination of results obtained by the author and presented in the attached international peer-reviewed journal papers [P1-P6]. Supplementary publications closely related to the topics in this thesis and with author's contribution are included in the bibliography. The

aim of this thesis is to give an introduction to the topics presented in the papers and summarize the key results.

The motivation of this thesis was to develop NIL based patterning processes for site-controlled epitaxy of quantum dots and for antireflective nanostructures. Despite its appealing properties and cost effectiveness, NIL has not been widely used in the field of quantum dot fabrication. The aim of this thesis was to prove the suitability of NIL patterning for the large-scale fabrication of site-controlled QDs. As an indication of the high throughput, hundreds of wafers have been patterned by NIL for various regrowth tests during the preparation of this thesis. Additionally, antireflective coatings were developed in order to increase the efficiency of multijunction solar cells. The fabrication of nanostructured coatings was developed by utilizing three dimensional patterning – a unique feature of NIL.

1.2 Thesis outline

This thesis is organized obeying the following structure. The key nanopatterning technologies are presented in chapter 2, with the emphasis being on nanoimprint lithography. Since other nanolithography techniques are mandatory when using nanoimprint lithography, the most common complementary techniques are presented. Chapter 3 covers the field of site-controlled quantum dots. An overview of the novel device applications based on quantum mechanics and quantum dots is given. The fabrication details and optical characteristics of quantum dots realized by UV-NIL and MBE are discussed. More detailed description about the results is given in publications [P1-P4]. In chapter 4, the fabrication and performance of nanostructured antireflection coatings for high efficiency solar cells are shown. The results are covered in publications [P5-P6]. Concluding remarks are combined in chapter 5.

Chapter 2

2 Nanolithography Techniques

Most of the novel functionalities in the future devices based on nanotechnology require high resolution patterning, i.e. lithography. Nanometer scale precision has been widely exploited in the synthesis of various materials, such as thin film fabrication, but this typically leads to nanometer scale control only in one dimension. Recent development in nanolithography techniques allows the fabrication of nanometer sized structures in three dimensions. The purpose of this chapter is to give an introduction to the most common nanolithography techniques, which are nanoimprint lithography, optical lithography, electron beam lithography, focused ion beam lithography, laser interference lithography and scanning probe lithography. The key technology in this thesis is nanoimprint lithography, but most of the other techniques presented here are also utilized in the thesis.

2.1 Nanoimprint lithography

Nanoimprint lithography was first introduced by Professor Stephen Chou in the University of Minnesota in the mid-90s [3]. After the invention, a rapid development in the field has been reported and numerous variations of the technique have been demonstrated. NIL is based on mechanical replication of a surface structure from a master template onto the sample. First, a nanopattern is fabricated on the master, which is usually made up of silicon or quartz, by some high resolution technique, such as electron beam lithography or laser interference lithography. Subsequently, the pattern is transferred to a stamp by molding. The polarity of the pattern is

reversed in the stamp as compared to the master. Finally, an identical replica of the master can be formed on the resist, which is spin coated on the sample, by bringing the stamp into contact with the sample. Alternatively, the master template can be used as a stamp in the imprint process, but then the polarity of the pattern is reversed on the sample as compared to the master. Nanopatterns with 2 nm features [6], a high throughput of 8 DVD discs/s [7] and patterning on a 12 inch wafer [8] have been demonstrated earlier by NIL. The cost of ownership for high resolution NIL equipment can be very low, and it can be integrated into a regular low cost mask aligner.

The two main categories of NIL are the variations based on thermal and ultraviolet (UV) curing of the resist. The original method was based on thermal curing, in which a thermoplastic polymer (imprint resist) is spin coated on the sample. Then the stamp is pressed on the polymer, which is softened by heating it above its glass transition temperature. The resist takes the form of the pattern in the stamp, which is peeled away after cooling down the resist. The pattern is then transferred to the sample by etching.

UV-NIL process is similar to the thermal NIL process, but is based on a resist, which is cured by UV light [12]. Therefore, either the stamp or the master has to be transparent in the UV regime. Soft UV-NIL utilizes soft stamps that are able to adapt to the roughness and curvature of the sample [13]. Figure 2.1 describes the main steps of soft UV-NIL process used in this thesis. First (1), a stamp is fabricated on a carrier glass plate. The stamp consists of three functional layers: a silicone cushion layer (Sylgard 184, Dow Corning Inc., USA), which distributes the imprint pressure and adapts to the shape of the sample in large scale; a thin glass (thickness 50 – 150 µm) layer, which is attached on the silicone layer, and prevents the lateral deformation of the pattern during the imprint [14]; and the patterned layer, which has inverted nanostructure on the surface. In this thesis, the patterned layer consisted either of thermally curable hard polydimethylsiloxane (PDMS) [15, 16] or UV curable OrmoStamp (Micro resist technology GmbH, Germany). The patterned layer was coated with fluorine containing molecule layer, which improves the antiadhesive properties. Perfluorodecyltrichlorosilane was used with PDMS and Optool DSX (Daikin Industries Ltd., Japan) with OrmoStamp. Second (2), resist is spin coated on the sample and the stamp is pressed on the resist. The applied pressure is typically in the range of 10 – 900 mbar. During the imprint, the resist is exposed to UV light and cured forming a replica of the master template. EVG 620 mask aligner (EV Group) was used for pattern alignment and UV exposure in this thesis. Third (3), the pattern is transferred

from the cured resist to the sample by etching. A unique feature for NIL processing is the residual resist layer, which is present under the protrusions of the stamp. Removal of this unwanted layer before transferring the pattern to the sample degrades the lateral quality of the pattern. We have studied the minimization of the residual layer in Ref. [16].

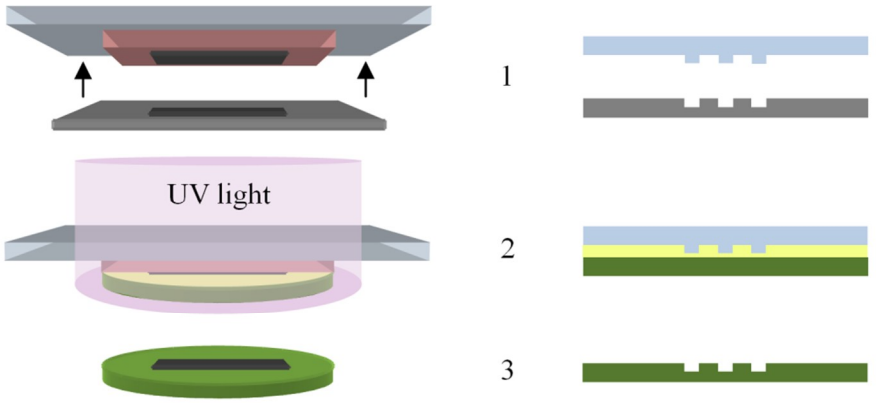

Figure 2.1: A schematic process flow of soft UV-NIL patterning. 1) Stamp fabrication, 2) Imprint process, 3) Patterned sample. : stamp, : master, : Sylgard 184, : resist, : sample.

Other variations of NIL are mainly based on the above mentioned curing methods, but differ in other technological aspects, such as stamp geometry. The imprint area can be extended by continuous imprinting such as roll-to-roll NIL (R2RNIL) and roll-to-plate NIL (R2PNIL), which utilize roll shaped stamps [17]. The area can also be increased by repeating small area imprint steps several times. Step and flash imprint lithography (S-FIL) technique is based on UV curing [18] and step and stamp imprint lithography (S-SIL) on thermal curing [19].

2.2 Optical lithography

Optical lithography techniques have been used in the fabrication of integrated circuits (IC) since 1970's. They are based on UV light that is shone through a mask to a resist layer on the sample. The mask has transparent and opaque areas, which define the pattern to be formed on the resist. The resolution for optical lithography is determined by diffraction and is

$$R = k_1 \frac{\lambda}{NA}, \tag{2.1}$$

where R is the lateral resolution, k_1 is a constant describing the process, λ is the wavelength of light and NA is the numerical aperture [20]. Current development towards the nanoscale has been driven by decreasing the wavelength of the exposure light with deep- or extreme-UV sources, increasing the NA of the system with immersion techniques, and using phase shift masks and double exposure schemes [21]. This has led to the fabrication of current IC devices with 22 nm resolution. However, achieving sub 50 nm resolution with optical lithography systems requires equipment investments in the order of tens of millions of dollars. In this thesis, low resolution optical lithography was utilized in the fabrication of alignment marks, electrical contacts and micrometer scale mesas.

2.3 Electron beam lithography

Electron beam lithography (EBL) is a direct writing method, where a focused beam of electrons is used to cure the resist. The pattern is formed on a dedicated resist according to the distribution of the incident electrons and transferred to the sample by etching. The resolution of this method is very high, because of the short wavelength of electrons. Feature sizes below 5 nm have been demonstrated [22]. Factors typically limiting the resolution are reflection and scattering of the electrons in the resist and in the sample, and charge accumulation [20]. The electron beam is controlled digitally, and computer aided design makes this technique very flexible. The serial nature of EBL means dramatically increasing writing times with increasing patterned areas, making it unsuitable for volume production. However, systems comprising of several electron beams have been developed in order to increase the throughput of EBL [23]. EBL is mainly used for NIL master templates, photolithography masks and prototyping. In this thesis, EBL was utilized in UV-NIL master fabrication.

2.4 Focused ion beam lithography

Focused ion beam lithography (FIB) is a writing technique very similar to the electron beam lithography but instead of electrons a focused ion beam is utilized for patterning. Typically, the

beam consists of gallium ions (Ga^+), but also argon (Ar^+) and krypton ions (Kr^+) are used [20]. The ion beam can be applied to resist exposure, ion implantation, material deposition and chemical etching, but the main application in the field of microfabrication is direct removal of material by physical sputtering. The sputtering technique is enabled by energetic ions, which cause erosion on most of the materials. Sputtering resolution is in the order of ten nanometers depending on the material [24]. Ion beam induced material deposition or etching is achieved by introducing a precursor gas to the ion beam. The incident ions break the chemical bond in the gas molecules and e.g. a metal layer is deposited or an etch gas is released. For example, $W(CO)_6$ and $C_9H_{17}Pt$ are used for tungsten and platinum deposition, respectively, and XeF_2 for fluorine based etching. Typical applications for FIB are prototype circuit repairing and fabrication of cross sectional tunneling electron microscopy (TEM) samples. In this thesis, the ion beam induced deposition was utilized to form etch masks for micropillar fabrication.

2.5 Laser interference lithography

In laser interference lithography (LIL), two or more coherent laser beams are directed on the sample. The beams form an interference pattern which is recorded to the resist on the sample surface. This maskless technique is used to pattern large areas and has a very high throughput. LIL is suitable for fabricating periodic structures and the pattern complexity can be increased by increasing the number of interfering laser beams [25]. The resolution is limited by the wavelength of the laser light. Feature sizes of 22 nm have been demonstrated using an immersion technique in combination with LIL [26]. Typical applications of LIL include photonic crystals, micro-lens arrays and optical storage media. In this thesis, LIL was utilized in UV-NIL master fabrication.

2.6 Scanning probe lithography

In scanning probe lithography (SPM) a sharp tip of an atomic force microscope (AFM) or scanning tunneling microscope (STM) is utilized for patterning. The tip is either brought into contact with the sample surface and a pattern is mechanically formed, or electric current or chemical reactions are exploited without a contact between the tip and the sample surface.

Electric current and chemical reactions are used in material deposition, removal and manipulation. In STM based lithography, the sensitivity of the tunneling current used for lithography provides extremely high resolution and many similar functions to EBL. AFM based lithography allows more materials to be processed and gives higher throughput than the STM based lithography but has lower resolution. Nanometer scale resolution and manipulation of single atoms have been demonstrated by this technique [27, 28]. Since controlling the tip position on a sample is very time-consuming, this technique is only suitable for very small scale applications. The throughput can be increased, for example, by utilizing multiple tips in parallel [29].

Chapter 3

3 Site-controlled Quantum Dots

The fabrication and key characteristics of site-controlled semiconductor quantum dots (SCQDs) as well as their most appealing device applications are presented in this chapter. The focus is on single III-V quantum dots and their fabrication for novel quantum information processing schemes. In the first section, an overview of the single SCQD applications is given. The following sections describe the realization of SCQDs by combining UV-NIL and molecular beam epitaxy, and their main structural and optical properties.

3.1 Quantum dot applications

Semiconductor quantum dots are expected to be the building blocks for the future information technology platforms. The main concepts exploiting the quantum mechanical properties of QDs are quantum computing and quantum cryptography. Quantum computing is based on qubits, for which the semiconductor QDs were the first solid state candidates [30]. Quantum cryptography provides a secure method for information exchange that is based on single or entangled photons emitted from QDs [31-33]. In addition, QDs find applications in low threshold lasers [34] and nanophotonic waveguides [35].

The idea and application of a quantum computer has increasingly attracted the research community from the 1990's. Before that time the quantum computer was only a theoretical model, but as the nanotechnology has greatly developed in the past two decades, it has become a near future device. In classical computers, the logical unit corresponding to a physical system

is the bit, which can have two separate states. E.g. charged or discharged capacitor or a voltage pulse above or below certain level. The speed-up of the calculations of present-day computers has been achieved by decreasing the size of the physical systems [20]. However, the limiting dimensions set by nature are about to hamper the development. The utilization of quantum physics may provide a solution for further development. In a quantum computer, the logical unit is called quantum bit or qubit. It is a two-level quantum mechanical unit, which can be in the superposition of the two states. Qubit can be formed of, for example, a photon with two-levels being the vertical and horizontal polarizations, or an electron having the spin up or down [36, 37]. Quantum computation with single photons was proposed already in the late 1980's [38] and electrical and optical addressing of single spin states in QDs has been demonstrated [39-41]. The superposition property and quantum parallelism provide in certain situations exponentially more efficient information processing with a quantum computer when compared to a classical computer. Because of the superposition property, a quantum system with N qubits can be in the superposition of 2^N states and by careful design and controlling the quantum dynamics of the system, operations can be made on the states in parallel. Controlling qubits based on single photons as well as spin states in QDs has been demonstrated [42-44].

In addition to single qubit operations, quantum mechanics offer a unique and essential property called entanglement. Entangled photon pairs are emitted from a single quantum dot utilizing a radiative decay of a biexciton state in the dot. A biexciton state is comprised of two bound electron-hole pairs (excitons). More detailed discussion about the energy levels in a QD is presented in section 3.4.1. The biexcitonic decay has been shown to proceed in two consecutive steps: first, the biexciton photon (2X) and after that, the exciton photon (X) are emitted [45, 46]. The photon entanglement is based on two possible decay paths for the recombinations, determined by the spin of the intermediate exciton state. Time-resolved photoluminescence experiments have shown that for an ideal, symmetric QD the left-hand circularly polarized 2X photon is followed by a right-hand circularly polarized X photon and vice versa [47, 48]. The photons are indistinguishable in energy and can be produced on demand, which makes this process an attractive candidate for an entangled photon source. However, if the dot is asymmetric, these two paths are distinguishable in energy and produce linearly polarized photons with orthogonal polarizations between the paths. QD asymmetry is tolerated if a cavity with certain mode structure is used [45]. An entangled photon source based on a semiconductor QD, and entanglement between a QD spin and a single photon were demonstrated lately [49-51].

Principles of producing polarization entangled photons are discussed in more detail in section 3.4.2.

3.2 Quantum dot fabrication

III-V quantum dots, such as InAs and InGaAs QDs, are typically fabricated by epitaxial growth methods. Epitaxial growth means that the crystal structure of the underlying substrate is reproduced to the new material layer formed on the substrate by bringing atoms of desired elements onto the surface. In favorable growth conditions, at high temperature, with proper material fluxes and in ultra-high vacuum, the growth proceeds in two-dimensional (2D) growth mode. Very abrupt interfaces can be produced between different material compounds. If the natural lattice constant of the grown compound differs from the lattice constant of the substrate, the overgrown layer is strained. In QD growth, the lattice constants have significant difference and the strain is relieved by the formation of three-dimensional islands, which minimizes the surface energy. Islands comprised of certain materials, such as InAs, and grown under suitable conditions are called quantum dots. The QDs are typically randomly positioned, i.e. self-assembled, on the surface. The QDs are between 20 and 40 nm in diameter and up to 15 nm in height. The lattice constant mismatch for InAs/GaAs material system studied in this thesis is 7 % [52]. The most studied technique to fabricate quantum dots by MBE or by metalorganic vapor phase epitaxy (MOVPE) is an intermediate growth method of 2D and 3D growths, called Stranski-Krastanov (SK) growth mode [53]. In SK growth of InAs QDs on GaAs, a two dimensional layer of InAs, known as the wetting layer (WL), is formed all over the surface before the formation of 3D QDs. The thickness of the WL is a couple of monolayers (ML). In this thesis, MBE and SK growth were exploited to grow InAs QDs. Figure 3.1 shows an exemplary AFM image of randomly positioned InAs QDs on GaAs surface and tables listing the main growth parameters and structural properties of the QDs. Typically, the adjustment of one growth parameter affects several structural properties simultaneously and the combined effect defines the structural properties which, in turn, determine the optical and electrical properties of the QDs.

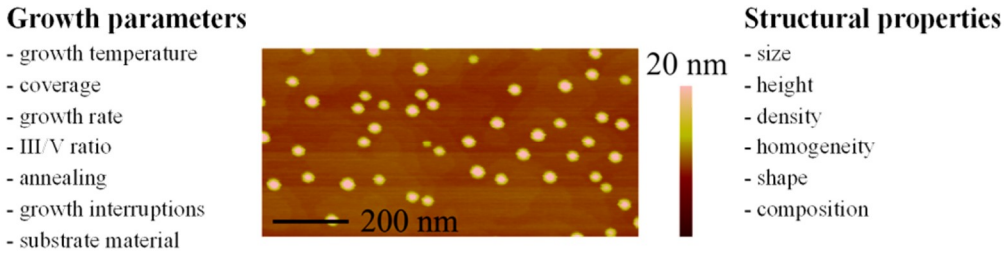

Figure 3.1: An AFM image of InAs QDs randomly positioned on GaAs surface. Surrounding lists indicate the main growth parameters and the structural properties of the QDs.

3.3 Quantum dot position control

In order to make quantum dots practical for advanced applications, precise control of the lateral position of a single QD, simultaneously with the control of its optical and electrical properties is required. Quantum information processing demonstrations introduced in section 3.1 were based on self-assembled, randomly positioned QDs. In order to attain scalability and practical devices, position control of the QDs is essential. In SK growth of QDs, the nucleation takes place at random locations induced e.g. by atomic layer steps or local strain fields. In site-controlled SK growth of QDs, the nucleation sites are defined by a lithographic step [54]. Local oxidation by atomic force nanolithography [55], focused ion beam lithography [56] and especially electron beam lithography [57-60] have been used to predefine the nucleation sites on the semiconductor surface. Techniques to form preferential nucleation sites for QDs include QD formation in small pits [55, 57, 58, 61], on preferential crystal planes [60, 62], in selective growth windows [63] and on locally modified strain fields by seed QDs [59, 61] or buried stressors [64]. Narrow exciton emission linewidths, single photon emission and coupling to a micropillar and photonic crystal (PhC) cavity have been demonstrated with SCQDs [55, 58-60, 65-67].

In this thesis, an UV-NIL based patterning process is utilized to form preferential nucleation sites for QDs. Approaches based on growth on etched pits and selective area growth are discussed in this section. The main focus is on SCQDs grown into GaAs pits. A schematic illustration of the SCQD growth is presented in Figure 3.2. Minimizing the surface energy and higher number of atomic layer steps in the pits than on the planar surface facilitates the QD growth in the pits. However, growth parameters have to be optimized for each structure to

control arsenic pressure and indium atom desorption from the surface and migration on the surface as indicated by the arrows in Figure 3.2(a). In addition to the growth parameters presented in Figure 3.1 in site-controlled QD growth, the properties of the pattern, such as size and shape of the pits and the periodicity, affect the structural properties of the QDs.

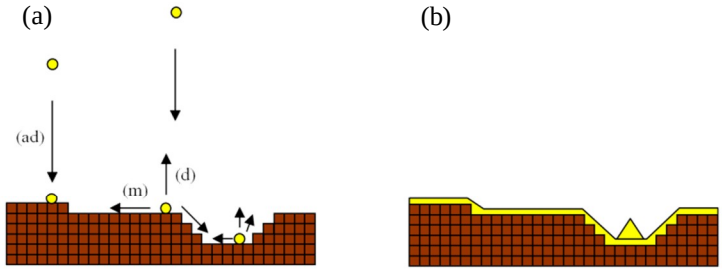

Figure 3.2: (a) Indium atom adsorption (ad), desorption (d) and migration (m) on GaAs (brown) surface. (b) 2D wetting layer of InAs (yellow) and a quantum dot formed in the pit.

3.3.1 Etched nanostructures for quantum dots

In order to facilitate SCQD formation, the pattern dimensions have to be in the same range as the size of the QD. UV-NIL provides the required resolution, but also the etching process needs to be controlled with nanometer accuracy. For etching GaAs(100) surface, several etch chemistries based on wet chemical etching and dry etching with inductively coupled plasma reactive ion etching (ICP-RIE) were explored in terms of etch profile and surface roughness [68]. Diluted solutions based on H_2SO_4, H_3PO_4, NH_4OH, HBr and H_2O_2, and plasma chemistries based on $SiCl_4$, BCl_3 and Cl_2 were studied, respectively. Wet etching is based on chemical reaction whereas plasma assisted dry etching is a combination of chemical and physical removal of the target material. The best nanoscale etching was achieved using BCl_3/Ar based chemistry and ICP-RIE with very low physical etch component [P1]. The process flow of an UV-NIL process for preparing pits on GaAs(100) surface is shown in Figure 3.3(a). 1) Stamp was brought into contact with the resist (mr-UVCur06, Micro Resist Technology GmbH) and the resist was cured using UV exposure and EVG 620 mask aligner (EV Group). 2) Residual layer etch was performed with oxygen plasma and RIE. 3) BCl_3/Ar based chemistry and ICP-RIE was utilized for smooth and shallow GaAs etching. 4) Oxygen plasma and RIE were utilized for resist removal. Figure 3.3(b) shows scanning electron microscope (SEM) and AFM images of a patterned GaAs surface. A surface profile from the AFM scan in Figure 3.3(b)

shows an etch depth of 20 nm. Pit diameter and period of this structure were 90 nm and 180 nm, respectively.

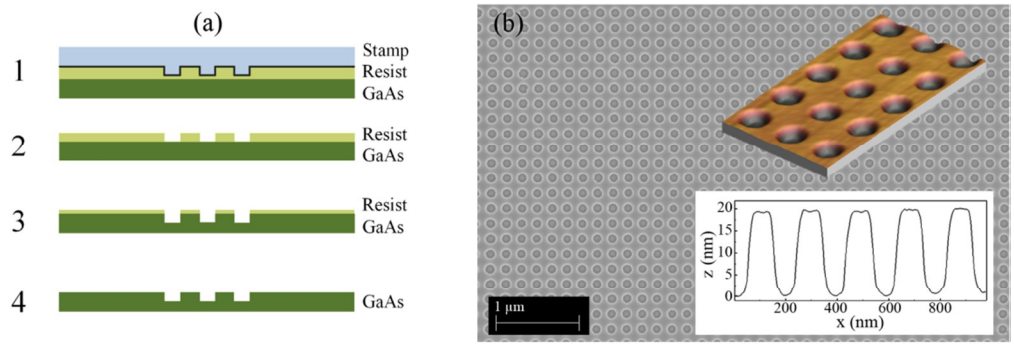

Figure 3.3: (a) 1) UV-NIL imprint, 2) Residual layer etch, 3) GaAs etch, 4) Resist removal. (b) SEM and AFM images of a patterned GaAs(100) surface. Pit diameter 90 nm, period 180 nm, depth 20 nm.

In order to address optically a single QD, more than 1 µm separation between the SCQDs is required. Patterns having periods of 0.5 – 10 µm and pit diameters of 80 – 200 nm were used. Figure 3.4 shows SEM images of the samples with periods ranging from 0.5 µm to 10 µm. Additionally, 1.5 µm deep alignment marks were fabricated for particular samples in order to facilitate the structural and optical studies of the single SCQDs as well as the integration into an optical microcavity described in Section 3.5. Figure 3.4(a) shows the modified process. First three steps and the final cleaning were identical to the process described above. In step four, the shallow pits were covered by optical lithography fabricated resist mask (resist 2) and the alignment marks were etched using UV-NIL resist (resist 1) as an etch mask and BCl_3/Cl_2 based chemistry and ICP-RIE. The patterned sample with alignment marks and a sample having a 1 µm overgrown GaAs on top of the structures are shown in Figure 3.5(b) and Figure 3.5(c), respectively. As indicated by the Figure 3.5(c), the alignment marks are clearly visible after a thick overgrowth of GaAs, which promotes the subsequent positioning.

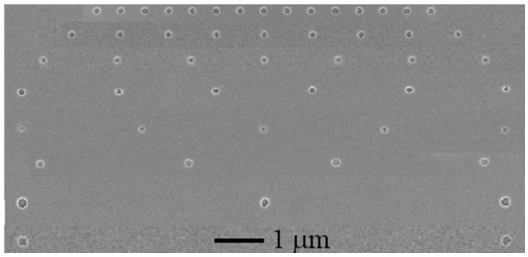

Figure 3.4: SEM images of the samples with patterns having periods of 0.5 µm, 1 µm, 1.5 µm, 2 µm, 2.5 µm, 3 µm, 5µm and 10 µm from top to the bottom, respectively.

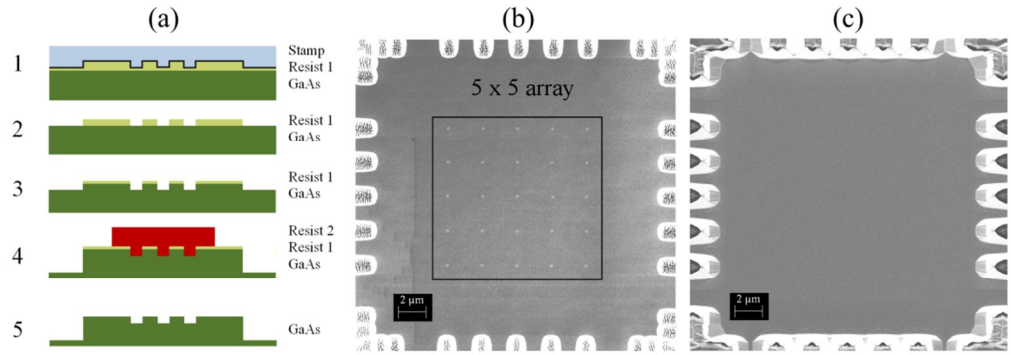

Figure 3.5: (a) The modified process for the fabrication of the alignment marks. The patterned sample with alignment marks (b) and a sample having a 1 µm overgrown GaAs on top of the structures (c).

3.3.2 Impurities and native oxides

Despite having advantageous properties described in chapter 2, UV-NIL requires polymers, which cause specific concerns for achieving epi-ready surfaces. Polymers differ in their chemical composition from those typically used in other nanopatterning methods (e.g. EBL and LIL). Usually the polymers are insoluble to solvents. Some NIL polymers contain inorganic additives that additionally complicate the ex situ surface cleaning of the process residuals. Additionally, removing the surface oxides before the MBE growth is a key issue when combining ex situ patterning and epitaxial growth.

In this thesis, removing the process residuals and native oxides was performed by combining plasma assisted cleaning, wet chemical etching and thermal annealing in the MBE chamber. The process steps are shown in Figure 3.6. Oxygen plasma and reactive ion etching (RIE) were

utilized to remove carbon-, hydrogen- and fluorine-related impurities [69]. Oxygen plasma is commonly used for volatilizing carbon and hydrogen compounds in resists. The etch parameters were optimized by studying the photoluminescence (PL) of a near surface quantum well sample exposed to oxygen plasma [P1]. The QW was separated from the surface by 50 nm GaAs layer and a decrease in the PL intensity was attributed to increased amount of defects induced by the plasma. Wet chemical treatment was utilized manly for the oxide removal, but also to remove processing related residuals that remained after the plasma treatment. Several chemicals were studied by measuring the PL from self-assembled QDs which were grown close to the processed surface [P1]. Separation between the processed surface and QDs was 5 nm. The deteriorated surface induces defects to the overgrown crystal, which degrades the optical quality of the QDs, thus reducing their PL intensity. A combination of isopropyl alcohol (IPA), HCl and NH_4OH containing solutions produced the strongest PL intensity. IPA removes organic impurities, and HCl and NH_4OH were mainly used for dissolving the oxides, i.e. As_2O_3, As_2O_5, Ga_2O_3, Ga_2O and $GaAsO_4$ [70]. The main target was to reduce the amount of Ga_2O_3, which requires high temperature for desorption and typically produces random holes on the surface during thermal desorption [71, 72]. A novel 3 M HCl:IPA solution was used since it was reported to leave arsenic rich surface which is preferable because of the low temperature needed to thermally desorb the arsenic compounds [73, 74]. Finally, thermal annealing at 590 °C in the MBE chamber was applied in order to desorb As compounds and oxides formed during the transport of the wafer in air from wet etching station into the MBE reactor. More detailed description about the cleaning procedures is presented in [68] and in [P1].

	Duration	Etch step
	10 min	Oxygen plasma, reactive ion etching
	2 min	Isopropyl alcohol (IPA)
	2 min	3 M HCl:IPA
		H_2O rinse
3x	2 min	$NH_4OH : H_2O$ 1 : 5
3x		H_2O rinse
3x	2 min	3 M HCl:IPA
	2 min	IPA
	Thermal annealing at 590 °C in the MBE chamber	

Figure 3.6. The process table describing the steps for the removal of the process residuals and native oxides.

3.3.3 Regrowth on patterned surface

After the patterning, cleaning and native oxide removal, the samples were loaded into the MBE chamber. Before the QD growth, the samples were thermally annealed at 590 °C and a buffer layer of GaAs was grown. The buffer layer was used in order to separate the QDs from the processed regrowth interface and from the defects induced by the patterning. The thickness of the buffer layer was chosen based on the pattern geometry and PL intensity measurements from QDs on samples with different regrowth buffer thicknesses. QD PL peak intensities at 1200 nm as a function of the buffer thickness are shown in Figure 3.7. PL intensity from a reference sample without a regrowth step is marked as 100 nm buffer thickness in Figure 3.7. For most of the structures, 30 nm regrowth buffers were used.

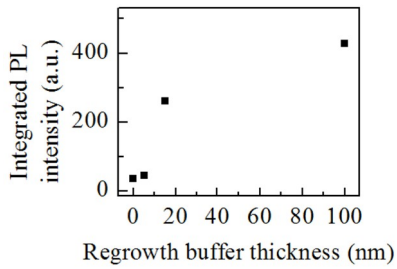

Figure 3.7: PL peak intensities at 1200 nm measured from capped QDs separated from the regrowth interface by the regrowth buffer. Intensity from a reference sample without the regrowth interface is marked as 100 nm buffer thickness.

The buffer growth temperature was observed to have a strong effect on the filling of the pits. Asymmetric filling was observed at growth temperatures above 500 °C. This was due to the anisotropic Ga atom diffusion on the surface and orientation dependent attachment rate [75]. Figure 3.8 illustrates the effect of the buffer growth temperature and the optimization of the amount of deposited InAs on a pattern presented in Figure 3.3(b). GaAs buffer thickness for the samples was 30 nm. The buffer growth temperature was reduced from 540 °C in Figure 3.8(a) to 470 °C in Figure 3.8(b) and the amount of InAs from 1.8 ML in Figure 3.8(a) and (b) to 1.65 ML in Figure 3.8(c). For 540 °C the pits were merged into grooves along [-110] crystal direction and for 470 °C the shape was preserved. Moreover, pits occupied primarily by single QDs were achieved with 1.65 ML InAs coverage.

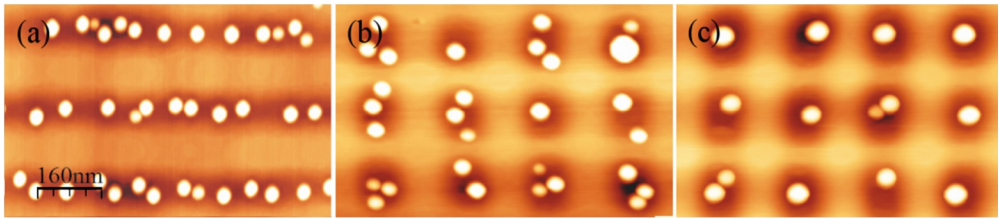

Figure 3.8: AFM micrographs after GaAs buffer growth at 540 °C (a) and at 470 °C (b), (c) and InAs deposition of 1.8 ML (a), (b) and 1.65 ML (c).

Though having preferential nucleation sites, the amount of InAs has to be closely matched to the density of the patterned structure. To further enhance the selectivity between the pits and the planar area, growth interrupted MBE [76] was utilized in the cases with low density QDs [P1, P4]. For optical studies of the single QDs, we used patterns with periods of 1.5 µm and 2.5 µm. 70 % probability of occupying each pit with a single SCQD was achieved for 2.5 µm period and pit diameter of 100 nm after patterning [P2]. Even higher probability (90 %) of single QD occupancy was achieved for 1.5 µm period [P4]. Figure 3.9(a) shows SEM and AFM images of an array of single SCQDs with period of 2.5 µm. The pit size was reported to influence on the properties of SCQDs [P2]. The diameter of the pit was observed to double during the overgrowth of the 30 nm GaAs layer and the depth was reduced more for small pits than for the larger ones. Figure 3.9(b) shows the depth and diameter of the pit as a function of the initial pit diameter after UV-NIL patterning. AFM profiles of GaAs surface after patterning and after GaAs buffer and QD growth are shown in the inset.

The size of a single QD grown in the pit was observed to depend on the pit size. Figure 3.10 shows the QD height as a function of pit dimensions measured from AFM line scans. Lower surface energy caused by the concave surface curvature assisted the indium migration towards the bottom of the pit producing QDs, which were proportional to the size of the pit [77], [P2]. This was also confirmed by micrometer scale PL (µPL) measurements which are discussed in more detail in section 3.4.

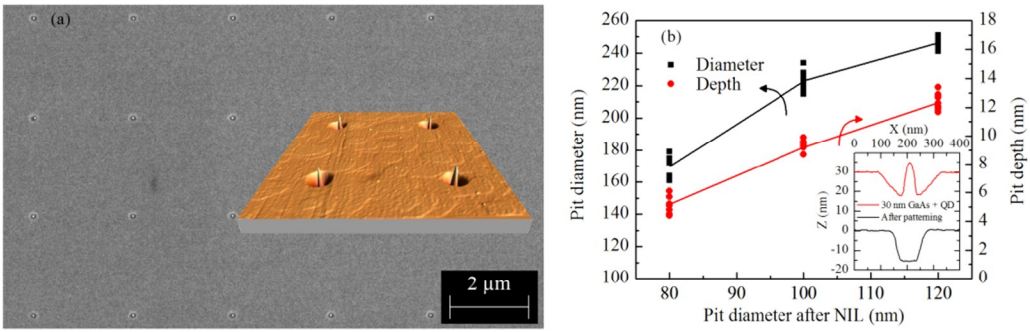

Figure 3.9: (a) SEM and AFM images of an array of single SCQDs with period of 2.5 µm and initial diameter of 100 nm. (b) The depth and diameter of the pits after GaAs buffer deposition as a function of the initial pit diameter after UV-NIL patterning. Inset shows surface profiles of GaAs surface after patterning and after GaAs buffer and QD growth.

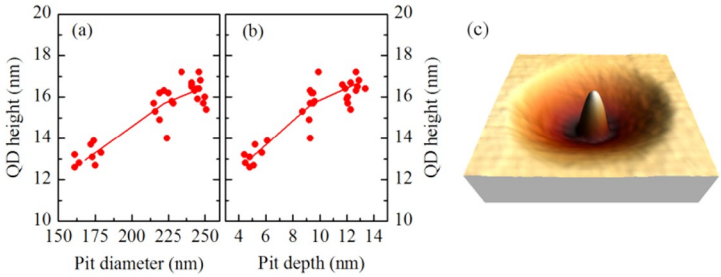

Figure 3.10: QD height as a function of pit diameter (a) and depth (b). Solid lines indicate the average values. (c) AFM image of a SCQD in pit with diameter of 250 nm.

For an alternative to dry etching, UV-NIL and anisotropic wet etching were utilized to form pits on GaAs(111)B surface. First, a SiO_2 hard mask was fabricated on GaAs surface by UV-NIL. Second, a crystallographic etch consisting of bromine and methanol was utilized. The etching proceeds at different rates on (111)B and (111)A orientations, finally forming triangular shaped inverted pyramids on the surface [78]. The pyramids have (111)A type sidewalls and extremely sharp tips with vanishing differences between the pyramids. Extremely homogeneous SCQDs have been previously fabricated by MOVPE into inverted pyramids [79, 80]. Figure 3.11 shows SEM images of bromine methanol etched pits on GaAs(111)B surface and a pit filled with MBE grown InAs. It is extremely difficult to use MOVPE for growth on planar (111)B surface, which restrains from the device fabrication. Here, MBE is supposed to provide a solution, but there are also factors making growth on (111)B surface more complicated than on (100).

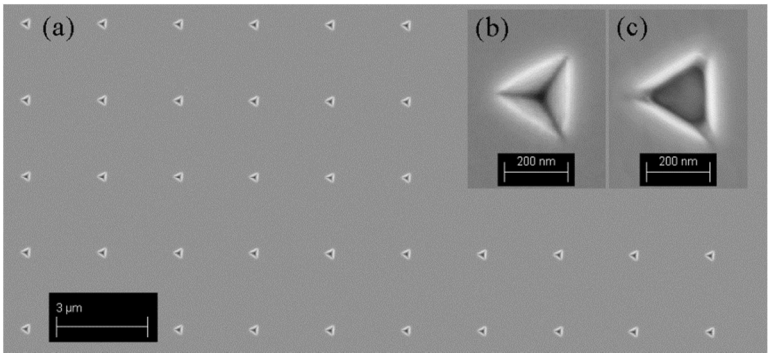

Figure 3.11: (a), (b) SEM images of bromine methanol etched pits on GaAs(111)B surface. (c) SEM image of an inverted pyramid filled with MBE grown InAs.

Etched GaAs surface provides an excellent framework also for various applications consisting of double or multiple SCQDs as shown in Figure 3.12. We have studied the formation of InAs QDs on etched grooves on GaAs(100) along [011], [01-1], [010] and [001] crystal directions by varying the growth temperature and the thickness of the regrowth buffer [81]. We observed that these quantum dot chains had anisotropic optical properties induced by the pattern [82]. Additionally, we studied the effect of post growth annealing and strain reducing layer to the optical properties of quantum dot chains [83, 84]. Figure 3.12(b) shows InAs QD chains in [001] direction and a combination of [010] and [001] oriented grooves is presented in Figure 3.12(c).

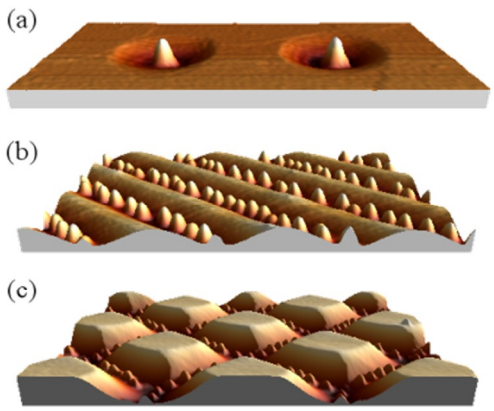

Figure 3.12: AFM images of SCQDs with various pattern geometries with periods of 300 nm (a), 180 nm (b) and 500 nm (c).

3.3.4 Selective area growth

Furthermore, we achieved lateral position control of the QDs without etching the semiconductor surface using selective area growth (SAG). In SAG the pattern is defined by a mask layer exposing the surface on predefined locations. With suitable growth conditions the sticking coefficient of gallium atoms on SiO_2 surface is reduced and GaAs is grown selectively in SiO_2 openings [85, 86]. We have used UV-NIL process for SiO_2 mask fabrication and subsequent SAG of GaAs mesas for guided self-assembly of InAs QDs [87]. The size, shape and facets of the mesa define the number of QDs grown on it. Figure 3.13 shows single InAs QDs on selectively grown GaAs mesas in SiO_2 openings. We observed that after SAG the SiO_2 mask was difficult to remove in standard hydrofluoric-based chemicals, which restricts the use of SAG in device applications. This was attributed to the diffusion of Ga onto SiO_2. Furthermore, we used identical UV-NIL patterning process for SAG of indium phosphide (InP) on InP and silicon wafers [88, 89]. QD growth on InP substrates has been developed in order to achieve emission wavelengths suitable for telecommunication bands (i.e. 1.3 – 1.55 μm) [90].

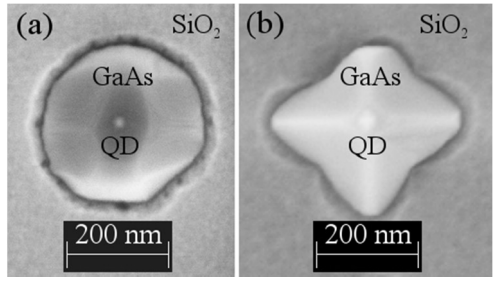

Figure 3.13: SEM images of single InAs QDs on selectively grown GaAs mesas in circular (a) and cross shaped (b) SiO2 openings.

3.4 Optical properties of single site-controlled quantum dots

The optical properties of quantum dots are defined by their electronic structure. The density of states for electrons and holes, which describes the number of quantum states per unit energy, is an important parameter when specifying the optical properties of semiconductors. The density of states is strongly modified when the dimensions of the structure become small and the

confinement for electrons and holes is increased in one or several dimensions. Figure 3.14 describes the density of states function when the dimensionality of the structure is reduced from 3D to 2D, 1D and 0D.

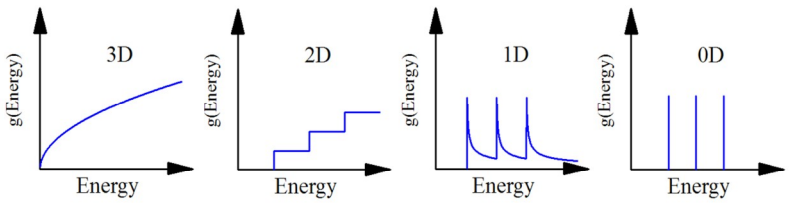

Figure 3.14: Schematic illustrations of the density of states function g(Energy) for 3D, 2D, 1D and 0D structures.

Already in the 1970's, quantum confinement of carriers in one dimension (2D structure in Figure 3.14) led to the application of quantum well (QW) laser [9]. In QW lasers the threshold current was reduced by an order of magnitude as compared to a bulk double heterostructure laser (3D structure in Figure 3.14) [10]. Confinement in two and three dimensions opened quantum wire (1D structure in Figure 3.14) and quantum dot (0D structure in Figure 3.14) research, respectively. When the confinement increases, the number of available states near the band edge is increased. In addition to the increased overlapping of electron and hole wave functions due to the spatial localization, this increases the probability of the optical transition. This effect is illustrated by the Fermi's golden rule, shown in Equation (3.1), describing the rate of the spontaneous emission.

$$W_{if} = \frac{4\pi^2}{h}\left|M_{if}\right|^2 g(Energy), \tag{3.1}$$

where W_{if} is the transition rate between initial and final states, M_{if} is the optical matrix element and *g(Energy)* is the density of final states. M_{if} is increased by the spatial localization of carriers and *g(Energy)* near the band edge by the confinement as discussed above [10].

In quantum dots, the carriers are confined in all three dimensions resulting in atomic like energy levels as shown in 0D structure in Figure 3.14. The band gap of InAs is smaller than the band gap of GaAs facilitating the capture of both electrons and holes into the InAs QD. Schematics of the band structure of an InAs QD in GaAs matrix is shown in Figure 3.15(a). Depending on the size of the potential well formed by the QD, different amount of energy states for electrons

and holes are accommodated within the QD. Typically, the carriers are injected optically or electrically into GaAs, from which they are captured by the QD via the WL. In the QD, the carriers are rapidly relaxed to the ground state and recombined emitting a photon (red arrow in Figure 3.15(a)). The capture and relaxation of carriers takes place in the order of ps, whereas the radiative lifetime for the carriers is in the order of ns. Multiple electrons and holes can be trapped simultaneously into the QD if the carrier injection is substantial. This causes state filling and recombination from the excited states takes place. Allowed transitions between the electron and hole states are described by the selection rules, which depend on the QD properties. For InAs QDs on GaAs it has been shown that the excited state emission occurs between the electron and hole states with the same quantum number [91]. The states are often referred to as s-, p- and d-shells consistent with atomic orbitals. A µPL measurement of the s-shell of a single QD is shown in Figure 3.17. Furthermore, the hole states are divided into so called heavy-hole and light-hole states depending on their effective mass. Additionally, the degeneracy between the heavy-holes and light-holes is lifted in compressively strained InAs, where the hole ground state consequently has more heavy-hole characteristics [92].

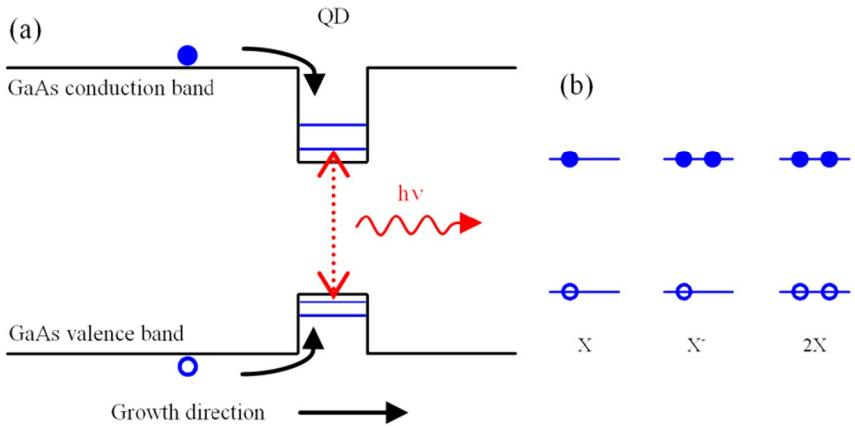

Figure 3.15: (a) A schematic illustration of the band structure of InAs QD in GaAs matrix and possible exciton configurations (b) for neutral single exciton (X), charged single exciton (X^*) and biexciton (2X).

3.4.1 Emission energy and linewidth

In order to incorporate QDs into optoelectronic devices they are capped by a semiconductor layer. This reduces efficiently the unwanted non-radiative recombination at the surface states.

QD properties are strongly affected by the overgrowth parameters during the capping. In radiative recombination process of an electron-hole pair (exciton) in QD, a photon is emitted. The energy and wavelength of the emitted photon is defined by the energy separation of the electron and hole states. The main parameters affecting the energy states in QD are the composition and height of the QD. For InAs QDs on GaAs, the emission energy has been reported to range from 1.4 eV, for very shallow QDs, to 0.8 eV for high QDs [93]. In single QD spectroscopy the energy states of one quantum dot are probed by injecting carriers into the QD and measuring the emitted photons. The emission spectrum of a single quantum dot shows several extremely narrow peaks associated with excitonic states such as neutral single exciton (X), charged single exciton (X^*), biexciton (2X) and charged biexciton ($2X^*$). The excitonic states are schematically shown in Figure 3.15(b). Neutral single exciton consists of one electron-hole pair whereas a charged exciton has an extra electron or hole and the biexciton two electron-hole pairs confined in the QD. Perturbations caused by the electrostatic interactions separate the excitonic states in energy [94]. Coulomb interactions cause e.g. the biexciton emission energy to differ from the exciton emission energy by the biexciton binding energy, which is typically in the order of a few meV. The excitonic states are identified by using either resonant or non-resonant excitation, and temperature, polarization or excitation power dependent measurements [95-97], as described in more detail later in this section and in the following section. The prospect of emitting single photons from a QD is based on the cascaded emission process and slightly different emission energies of the excitonic energy states. The last photon emitted after a short excitation pulse is separated in energy from the other ones, which facilitates the isolation of those photons [94]. This makes the QD a potential source of triggered single photons.

The homogeneous linewidth of the ground state exciton is in the order of a few μeV as studied by resonant optical excitation [98]. However, when using non-resonant optical excitation in PL studies, the linewidth is strongly increased by the fluctuating charge distribution in the QD environment. This effect is commonly referred to as spectral diffusion. In the case of site-controlled QDs, the regrowth interface and ex-situ patterning induce defects very close to the QD environment. This causes reduction in the luminescence intensity and broadening of the linewidth. Intense and spectrally narrow luminescence peaks are desired when spectrally selecting a single line, coupling an emission state and an optical cavity mode [99] or generating indistinguishable photons [59].

In QD ensembles the size and composition distribution causes inhomogeneous broadening to the emission energy spectrum, which consists of the emission peaks from several QDs. The inhomogeneous broadening typically varies from 15 meV up to 100 meV depending on the growth conditions. However, values down to 4 meV have been reported when using site-controlled growth on inverted pyramids on GaAs(111) wafers [79]. In this thesis, integrated QD ensemble PL was utilized when optimizing the surface cleaning, as discussed in section 3.3.2, and choosing the regrowth buffer thickness, as discussed in section 3.3.1.

Schematic of the µPL setup used in this thesis for the optical measurements of single QDs is shown in Figure 3.16. The sample was mounted in a low vibration closed-cycle helium cryostat and cooled down to 5 K. The laser beam used for optical excitation at 532 nm was focused down to a spot size of 1 µm on the sample with a 50x high numerical aperture objective. The emitted PL light was collected by the same objective and dispersed with a 0.75 m spectrometer equipped with a 1800 lines/mm grating and a cooled CCD detector. The spectral resolution of the setup was 30 µeV. A typical excitation power dependent µPL measurement of a capped InAs/GaAs single SCQD is shown in Figure 3.17. The QDs were fabricated with 2.5 µm separation and they were surrounded by alignment marks facilitating the optical addressing and identification of each individual QD. The corresponding surface SCQDs were shown in Figure 3.9. The integrated intensities obtained from the µPL spectra shown in Figure 3.17(a) are plotted as a function of the laser power for the X, 2X and X* peaks in Figure 3.17(b). The inset in Figure 3.17(a) shows a linewidth of 41 µeV. We achieved recently a resolution limited linewidth of 32 µeV for another SCQD [100]. The solid lines in Figure 3.17(b) represent fitting the data to the relation $I \propto P^n$, where I is the integrated intensity for the peak and P is the excitation power. For n, we obtained values of 0.7, 0.9 and 1.4 for X, X* and 2X peaks, respectively. Theoretical estimations based on rate equations would lead to n values of one and two for X and 2X, respectively [101]. However, deviations from those values have been reported previously and the fact that the intensities of the 2X peak are proportional to the square of the intensities of the X peak, as shown in the inset in Figure 3.17(b), confirm the identification [102, 103]. Additionally, the fine-structure splitting (FSS) measurement discussed in more detail in section 3.4.2 resulted in symmetric polarization dependence for X and 2X peaks. The biexciton binding energy for this SCQD was 2.1 meV.

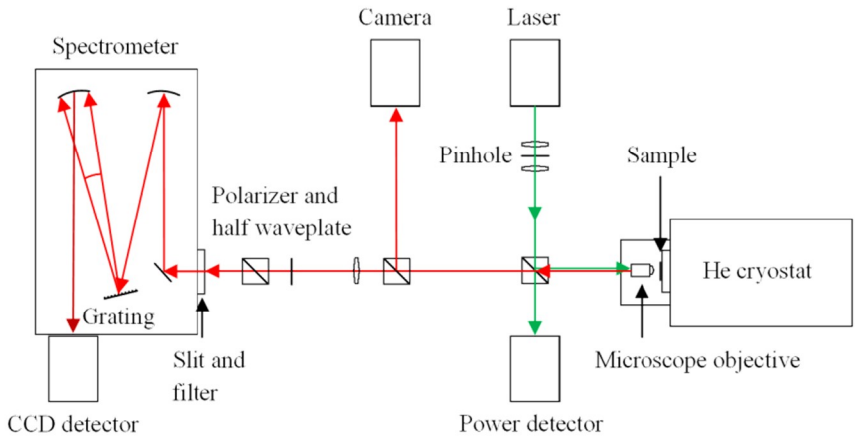

Figure 3.16: A schematic illustration of the µPL setup for optical measurements of single QDs. The excitation wavelength was 532 nm and the sample was mounted on a precision piezo stage in the He cryostat. An external light source (not shown) and the camera were used for coarse sample alignment. The polarizer and a rotating half waveplate were used for polarization dependent measurements.

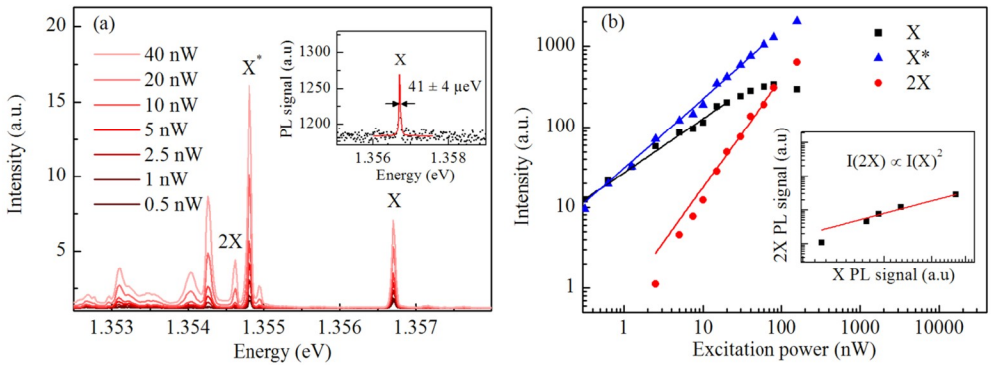

Figure 3.17: (a) Measured µPL spectra at different excitation powers using excitation at 532 nm. The inset shows a spectrum of the SCQD measured at 7 K and at 0.25 nW excitation power. The Lorentzian fit to the exciton peak shows a linewidth of 41 µeV. (b) The integrated intensities as a function of the laser power for X, 2X and X* peaks for a single SCQD. The inset shows intensities of the 2X peak as a function of the intensity of the X peak.

Several single SCQDs in pits with diameters of 80 nm, 100 nm and 120 nm were measured in order to study the SCQD size dependence on the pit size. QD height before capping as a function of the pit diameter and depth were shown in Figure 3.10. The SCQDs were capped at

relatively high temperature (540 °C), which strongly reduced the QD height and caused In/Ga intermixing. It allowed measurements within the charge-coupled device (CCD) detector range below the wavelength of 1000 nm (above 1.24 eV). Figure 3.18 shows the emission energy related to the X peak as well as the linewidth of the peak as a function of the pit diameter after patterning. The emission energy decreased with increasing pit size. This was due to the increasing QD height with increasing pit size as observed in the AFM measurements in section 3.3.1 [P2]. Additionally, the linewidth was observed to decrease with increasing pit size. This was attributed to the spectral diffusion caused by charged defects in the QD environment.

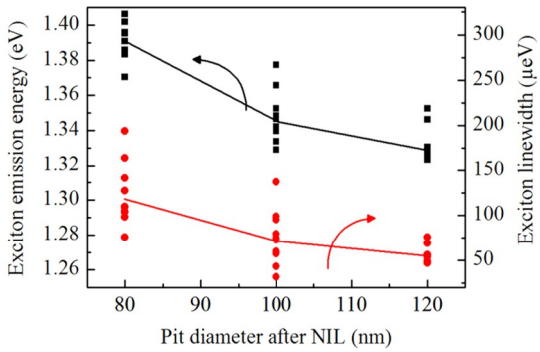

Figure 3.18: Emission energy and linewidth of the X peak in a SCQD as a function of the pit diameter after patterning measured at 40 K. Average values are indicated by solid lines.

In addition to the single linewidth measurement, the optical quality of SCQDs was evaluated by measuring time-resolved μPL and temperature dependent optical properties of the QDs [P4, P3]. Defects induced by the patterning process cause non-radiative recombination channels, which were assessed by measuring the PL decay time and the optical properties as a function of temperature. Decay time provides a sensitive method to evaluate structural differences between QDs because it is affected by non-radiative recombination channels. For SCQDs in an array, an average decay time of 669 ps was obtained. It is consistent with previous results for self-assembled quantum dots (SAQDs) [104, 105].

Figure 3.19 shows PL intensity images at 5 K, 40 K and 70 K from an area with diameter of 30 μm, including the edge of an array of SCQDs and a few SAQDs outside the array. Regular bright spots with the period of 1.5 μm were observed, reproducing the patterned array. Only a few interstitial QDs were observed within an array of more than one hundred SCQDs. At 5 K, the image was dominated by the emission from WL. At 40 K, the WL emission was reduced

and emission from SCQDs pronounced with an increase in the intensity related to the single exciton emission. At 70 K, most of the QDs exhibited bright luminescence but emission from some individual QDs was strongly decreased due to the thermal escape of carriers.

We selected randomly a SCQD and a SAQD from the area shown in Figure 3.19 and performed temperature dependent μPL measurements on the QDs. Figure 3.20 shows the energy (a) and linewidth (b) of the exciton emission peaks as a function of temperature. The X emission energies and linewidths for both QDs had very similar temperature dependencies. The band gap of InAs is decreased with increasing temperature as described by Varshni's empirical law [106], shown in Equation (3.2).

$$E_g(T) = E_0 - \frac{\alpha T^2}{(T+\beta)}, \tag{3.2}$$

where E_g is the band gap energy, E_0 is the band gap energy at 0 K, T is temperature, and α and β are fitting parameters. The solid lines in Figure 3.20(a) representing Varshni's law shifted in energy and with InAs parameters agree well with the measured data points [107-109]. Below 30 K the exciton linewidth was limited by the spectral resolution of the setup (66 μeV). Above 30 K the linewidth increased rapidly due to phonon scattering [110], consistent with previous results for SAQDs [111] and SCQDs [112, 113].

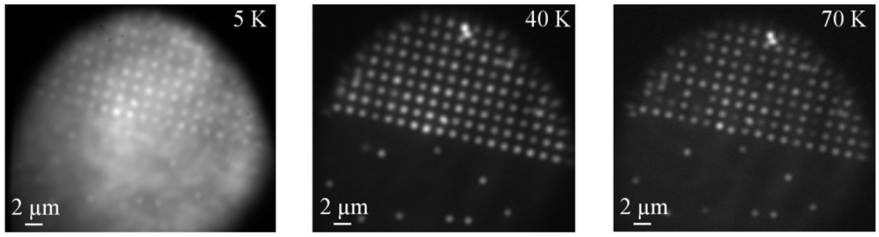

Figure 3.19: PL intensity images at 5 K, 40 K and 70 K from the edge of an array of SCQDs with the period of 1.5 μm. The intensity was measured within the spectral range of 850 – 1000 nm and excitation power of 1.77 μW and wavelength of 532 nm was used.

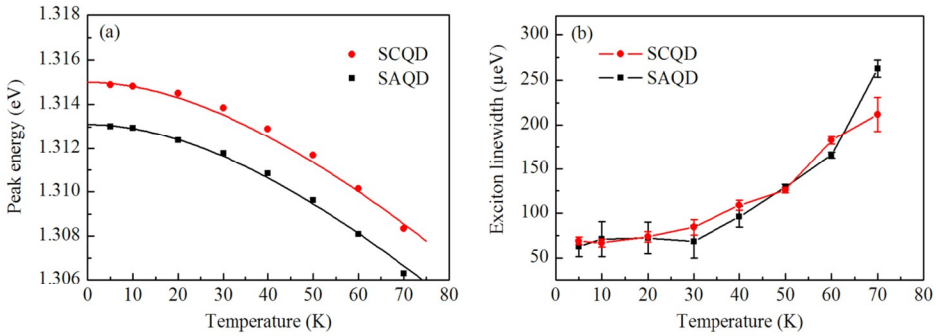

Figure 3.20: (a) Exciton emission energy as a function of temperature. Solid lines represent fits to Varshni's law. (b) Exciton linewidth as a function of temperature.

3.4.2 Exciton fine-structure splitting

The exciton state in an ideal symmetric QD consists of degenerate spin-up and spin-down states. However, the degeneracy in a typical QD is lifted because of the electron-hole exchange interaction and an in-plane asymmetry of the QD [114]. Due to the splitting of the levels, linearly polarized emission along the lateral crystallographic axes is observed [10]. The energy separation of the levels is called exciton fine-structure splitting (FSS). Minimization of the FSS to the order of a few μeV is essential in order to produce polarization entangled photons by biexciton-exciton cascade [47, 48]. A schematic illustration of the energy levels, polarizations and FSS as well as polarization resolved μPL measurements of a SCQD are shown in Figure 3.21. In a QD without FSS in exciton state (Figure 3.21(a)) circularly polarized light is emitted in both X and 2X recombinations. For a QD with FSS (Figure 3.21(b)), two possible recombination paths exist, both emitting linearly polarized light with orthogonal polarizations [115]. The biexciton state has no splitting because the net spin of the electrons and holes is zero, but the splitting of the X state causes linearly polarized 2X emission with 90 degree phase shift as compared to the X emission, as shown in Figure 3.21(d). Figure 3.21(c) shows two μPL measurements with orthogonal polarizations from a SCQD. The position of the 2X peak is shifted to higher energy when changing from x- to y-polarization and the position of the X peak is shifted by the same amount but in the opposite direction. Figure 3.21(d) shows relative peak positions for X and 2X peaks as a function of the polarization angle obtained from Lorentzian fits to the data. Error bars indicate the error in Lorentzian fitting and fitted sine functions are

presented by solid lines for both of the peaks. FSS was deduced from the peak to peak values of the sinusoidal fits. The FSS value for this SCQD was 11 μeV.

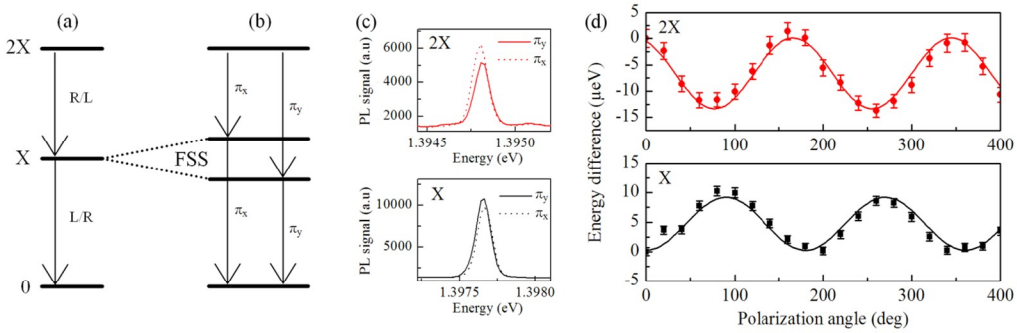

Figure 3.21: Schematic illustrations of the energy levels in a QD without FSS (a) and with FSS (b). (c) μPL spectra showing X and 2X peaks from a SCQD. Solid and dotted lines represent y- and x-polarized detection, respectively. (d) Relative X and 2X peak positions as a function of the polarization angle obtained from Lorentzian fits to the data. Error bars indicate the error in Lorentzian fitting and fitted sine functions are presented by solid lines for both of the peaks.

Polarization dependent measurements of 17 single SCQDs were performed in order to statistically assess the FSS in the SCQDs fabricated by UV-NIL and MBE [P2]. FSS values from 4 μeV up to 27 μeV were obtained and the average value was 15.7 μeV, which is a very low value since typical FSS values for SCQDs on GaAs(100) surface have been reported to range from 20 μeV to 60 μeV [58, 116]. Summary of the FSS values as a function of the emission energy and an exemplary measurement providing the FSS value of 4.4 μeV are presented in Figure 3.22. We did not observe any dependence of the FSS on the emission energy as was previously reported [115, 117]. This was attributed to the relatively small FSS and small QDs due to capping at high temperature [P2].

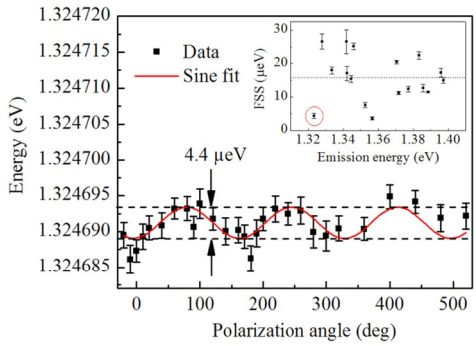

Figure 3.22: Exciton peak energies as a function of the polarization angle obtained from Lorentzian fits to the polarization dependent μPL measurement of a SCQD. The solid line represents a sinusoidal fit from which the FSS value was calculated and marked as a red circle in the inset. The inset shows FSS values for 17 single SCQDs as a function of the emission energy and the average value of 15.7 μeV as a dashed line. The error bars indicate the error in fitting to the data.

InAs QDs on GaAs(100) surface are typically elongated along [1-10] direction causing polarization orientations along [1-10] and [110] crystal directions but also other orientations have been observed [118, 119]. In addition, a small FSS is predicted even for structurally symmetric QDs due to anisotropic strain field, piezoelectric effect and reduced atomistic symmetry [120]. Several post growth methods, such as thermal annealing and the application of electric or magnetic field, to tune FSS have been demonstrated [118, 121-123]. Thermal annealing is based on the reduced long-range exchange interaction due to the reduction in the confinement potential and effects on the shape- and piezoelectricity-induced exciton asymmetry. An in-plane electric field is used to tune the overlap of the electron and hole wave functions and Zeeman splitting is utilized in magnetic field tuning.

3.5 Quantum dot integration into an optical cavity

Coupling an emitter to the ambient light field defined by an optical cavity gives rise to an enhanced light-matter interaction. Cavity quantum electrodynamics (cQED) stands for the field where the emitter is coupled with a low mode volume cavity providing 3D photon confinement [124]. The cQED is divided into weak and strong coupling regimes depending on the strength

of the emitter-photon interaction. In the weak coupling regime, the spontaneous emission rate is enhanced as compared to its vacuum level by tuning the cavity mode into resonance with the emitter. The enhancement is described by the so called Purcell effect [125]. The decay time of the emitter is reduced due to the resonant cavity mode. In the strong coupling regime, reversible energy exchange between the emitter and the cavity mode takes place and a vacuum Rabi splitting is observed. An anti-crossing of the cavity peak and the QD peak is observed in the μPL spectrum. This coherent coupling is the main target when utilizing cQED in quantum information processing [126].

Quantum dot integration into the optical cavities consisting of microdiscs, PhC cavities and micropillars has been demonstrated [65, 67, 127]. PhC cavities have very small mode volumes and high quality factor cavities have been fabricated out of both microdisc and PhC cavities. However, the light extraction and electrical contacting is more difficult than for micropillars. In this thesis, SCQDs were integrated into the micropillar cavities. The emission profile from a micropillar has appealing vertical directionality and they are easily adapted to electrical injection schemes [65].

First, a sample consisting of capped SCQDs with 2.5 μm period was fabricated on a 25 pair GaAs/AlGaAs distributed Bragg reflector (DBR) as described in section 3.3.1. An optimized patterning process was used to form 1.5 μm deep alignment marks for each SCQD, in order to align micropillars after the top DBR overgrowth [P2]. Here, the shallow pits for SCQDs were covered by optical lithography fabricated resist mask and the alignment marks were etched using UV-NIL resist as an etch mask and BCl_3/Cl_2 based chemistry and ICP-RIE. Second, another regrowth step consisting of a 20 pair GaAs/AlGaAs top DBR was applied. Third, aligned FIB induced deposition of platinum was utilized to form an etch mask for the micropillars. Circular platinum features were used in the fabrication of a SiO_2 etch mask for the final GaAs/AlGaAs dry etching. Finally, ICP-RIE etching and $SiCl_4$/Ar based chemistry were utilized to form micropillars around the SCQDs. Each SCQD was located in the middle of a 1-λ cavity consisting of GaAs. SEM image of an array of 25 micropillars is shown in Figure 3.23.

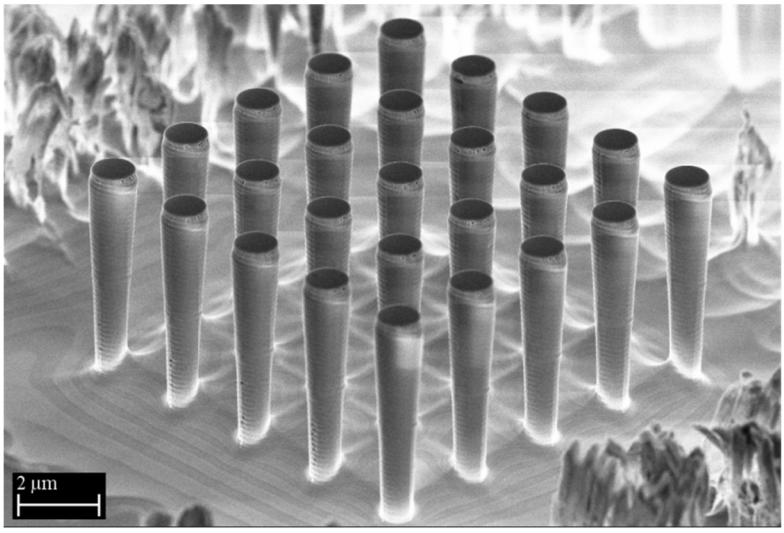

Figure 3.23: SEM image of a micropillar array, each pillar including SCQDs. The diameters of the pillars are 1 µm and the period is 2.5 µm.

Temperature tuning was utilized to spectrally align the cavity (C) peak and X peak into resonance. Temperature dependence is stronger for the X peak, as described in section 3.4.1, than for the cavity peak. Cavity peak is shifted in energy mainly due to the temperature dependent refractive index of GaAs. Figure 3.24 shows a µPL measurement of a SCQD inside a 1 µm diameter micropillar as a function of temperature. Figure 3.24(a) shows µPL spectra measured at 35 K, 45 K and 55 K and Lorentzian fits to the data for cavity (C) peak (blue curve) and for X peak (red curve). The energies of the peaks as a function of temperature are shown in the upper panel of Figure 3.24(b). Solid lines show Varshni's law and linear fits for the X and C peaks, respectively. Crossing of the lines takes place at 44 K, where the intensity of the X peak is at maximum. The lower panel in Figure 3.24(b) shows the integrated intensity of the X peak. A clear increase in the intensity was observed around 44 K as an indication of the QD-cavity coupling. However, no anti-crossing was observed, thus implicating the operation in the weak coupling regime. The estimated value for the quality factor of the cavity was in the order of 1000.

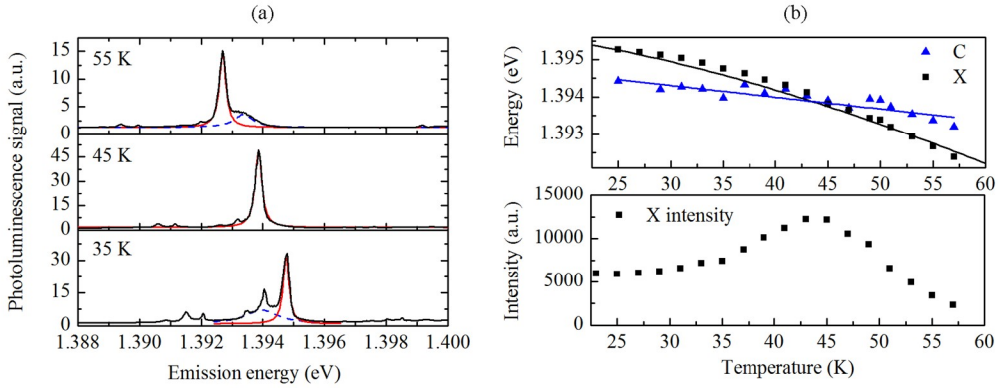

Figure 3.24: (a) µPL spectra of a SCQD inside a 1 µm diameter micropillar measured at 35 K, 45 K and 55 K and Lorentzian fits to the data for cavity (C) peak (blue dashed curve) and for X peak (red solid curve). (b) The emission energy and intensity of the X peak as a function of temperature obtained from Lorentzian fits. Upper panel shows also the energy of the cavity (C) peak. Solid lines represent fits to Varshni's law and linear fit for X and C peaks, respectively.

Chapter 4

4 Antireflection Coatings

In this chapter, design and fabrication of a nanostructured antireflection coating are described. The first two sections introduce the background of antireflective coatings and their application in the field of photovoltaics. The last section describes the properties and fabrication of a novel nanostructured antireflection coating based on high resolution, high throughput UV-NIL patterning, and its integration onto III-V semiconductor solar cells.

4.1 High efficiency solar cells

The most common solar cell technology in consumer applications is based on silicon. Silicon solar cells consist of monocrystalline (c-Si), polycrystalline (poly-Si) or amorphous silicon. Monocrystalline silicon solar cells have the highest conversion efficiencies but are more expensive than the polycrystalline ones. The typical efficiencies of silicon solar cells are in the range of 13 – 18 % [128], but the record is 25 % [11]. Solar cells based on III-V semiconductor technology, have efficiencies ranging from 29 % for GaAs cell to more than 40 % for multijunction solar cells [11]. Other types of technologies are organic and dye-sensitized solar cells, having record efficiencies of 10.7 % and 11.9 %, respectively [11].

The deployment of high-efficiency multijunction III-V semiconductor solar cells in terrestrial solar power plants has attracted increasing interest in the past few years because of the development of advanced solar concentrator systems that are able to meet grid parity. Photovoltaic concentrators are used to collect sunlight from large area to relatively small solar

cells by lenses or mirrors [129]. The aim is to reduce the area of the expensive solar cell and use less expensive lenses and mirrors. Concentration ratios (ratio between the module aperture area and the cell area) of some tens or hundreds of suns for silicon solar cells and up to 2000 suns for III-V solar cells have been used [11, 129]. Conversion efficiencies of more than 40 % have been demonstrated for three-junction III-V cells using concentrators [130, 131] and even higher efficiencies are predicted for cells with more than three junctions [132]. Recently, an American company called Solar Junction has set the new world record in solar cell efficiency, 44.0 %, under 942 suns [11].

Due to the exploitation of multiple absorption bands, multijunction solar cells exhibit a wide absorption spectrum ranging from 300 nm to beyond 1800 nm. In multijunction solar cells separate p-n junctions of different materials are used to absorb light within narrow spectral ranges. When connecting these multiple p-n junctions in series with tunnel junctions in between, a wide absorption spectrum is achieved. The utilization of materials absorbing at different wavelengths lowers the so called quantum defect, which describes the energy lost as heat in the absorption process. A schematic illustration of a triple junction solar cell and its absorption bands are presented in Figure 4.1. The absorption bands in Figure 4.1(b) are described by the schematic external quantum efficiency curves, which refer to the percentage of photons, converted into electric current at certain wavelengths, and includes the optical losses. Typical materials for light absorption are GaInP (absorbing within the spectral range of 300 – 650 nm), GaAs (650 – 850 nm), GaInAsN, InGaAs (850 – 1200 nm) and Ge (900 - 1850 nm) [11, 129, 130]. To fully exploit the potential of multijunction cells, broadband antireflection coatings should be employed to reduce the high discontinuity of the refractive index at the semiconductor-air interface. Without an antireflective coating, III-V solar cells have reflectivities typically in the order of 30 %, but the coating can reduce the reflectivity well below one percent within certain spectral range [129]. In addition to the requirement for broader antireflection coatings, multijunction solar cells are more sensitive than single-junction cells to variations of the reflectivity because of the current matching requirements [129]. In series-connected multijunction device, the subcell generating the lowest photocurrent limits the current of the entire device. The reflectance spectrum of the antireflection coating thus greatly affects the photocurrent generated by each subcell. Deviation of the coating from the optimum reflectance results in increased current mismatch.

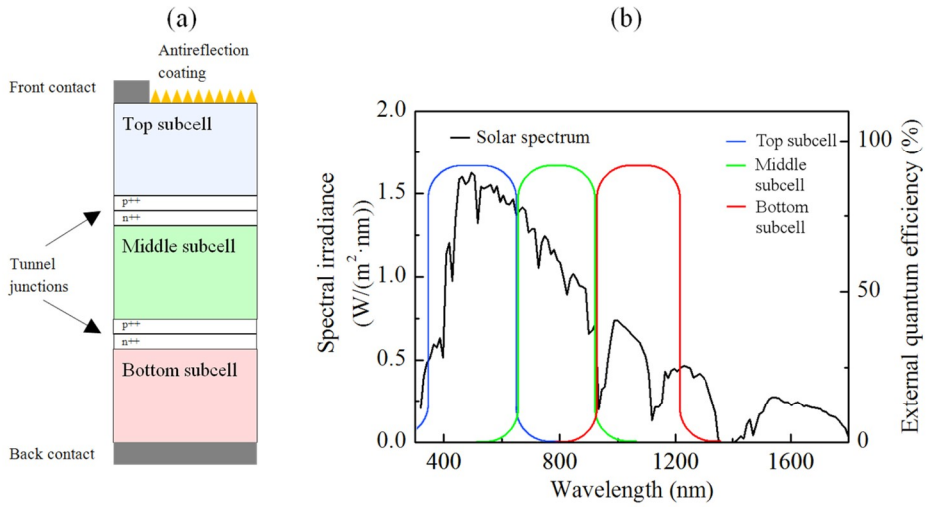

Figure 4.1. A schematic structure of a triple junction solar cell (a) and its illustrative absorption bands (b). The solar spectrum (black line) is shown on the left y-scale and the illustrative external quantum efficiencies (blue, green and red lines) on the right y-scale.

4.2 Thin film coatings

The most common thin film coatings for antireflection purposes consist of oxides, fluorides and nitrides of various materials. They can be fabricated by well-established volume production techniques such as chemical vapor deposition (CVD) or physical vapor deposition (PVD). The reflectivity can be reduced below one percent by using single or double layer dielectric coatings, but the spectral bandwidth where the reflectivity is the lowest is limited [133]. When using e.g. a double layer coating designed to have its minimum reflectivity at 600 nm with ideal refractive indices, the bandwidth where the reflectivity is below 5 % is less than 1000 nm [134]. In reality, the refractive indices cannot be chosen arbitrarily, but based on real materials with certain indices and other properties. Typical materials used in thin film antireflection coatings are Y_2O_3, Sc_2O_3, La_2O_3, Si_3N_4, SiO_2, HfO_2, ZrO_2, Ta_2O_5, TiO_2, Al_2O_3, ZnS and MgF_2 [128, 134]. The bandwidth with typical materials is in the order of a few hundred nanometers for multilayer structures [128]. Additionally, the reflectivity at large incident angle is increased compared to the reflectivity at normal incidence, which complicates their integration into a concentrator system, where the angle of incidence is increased [135]. The optimization of dielectric multilayer structures for the use as antireflection coatings in high efficiency III-V solar cells is

therefore challenging. However, thin film coatings are well suitable for silicon solar cells, which utilize spectral range from 400 nm to 1100 nm.

A two layer MgF_2 / Ta_2O_5 antireflection coating was used in solar cell reaching to 41.1 % efficiency [131]. Complex, nanoporous and co-sputtered materials have also been used as multilayer antireflection coatings. In the case of nanoporous SiO_2 the refractive index can be tuned down to 1.05 [136]. Co-sputtering enables the tuning of the refractive index by mixing two materials, such as SiO_2 and TiO_2. A six-layer antireflection coating consisting of these materials has been calculated to possess an average reflectivity of 5 % for incident angles from 0 to 90 degrees and within the spectral range of 400 – 1500 nm [135].

4.3 Nanostructured coatings

A recent approach to fabricate broadband antireflective coatings is to exploit the so called moth-eye concept and fabricate sub-wavelength nanostructures on the surface of the solar cell [137]. Antireflective properties in the eyes of insects were studied already in the 1970's [138]. Due to its sub-wavelength nature, this type of nanostructure provides a graded transition of the effective refractive index between air and the semiconductor surface, and thus, decreases efficiently the amount of reflected light in a broad wavelength range and at all incident angles [138, 139]. A schematic illustration of the graded refractive index is shown in Figure 4.2. Moth-eye antireflection structures can be fabricated on various materials by etching or molding. The fabrication of moth-eye structures on polyethylene terephthalate (PET), diamond, silicon, GaAs and GaSb layers has been demonstrated [137, 139-143].

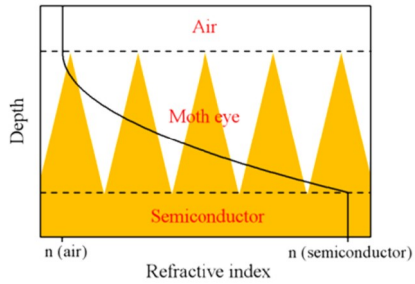

Figure 4.2: A schematic illustration of the graded refractive index from air to semiconductor induced by nanostructured coating.

The most popular technique to fabricate the moth-eye structure has been nanoimprint lithography. It is capable of producing 3D nanopatterns on large areas, which is essential in solar cell applications. The dimensions of the structures are in the order of a few hundred nanometers. Moth-eye structures producing the lowest reflectivity so far on silicon had a period of 230 nm and height of 700 nm [139]. The average reflectivity in the spectral range of 400 – 1000 nm was less than 3 % for incident angles up to 45 degrees. Even lower reflectivities were obtained for a moth-eye structure made on acrylic resin on PET substrate optimized for c-Si solar cells [140]. This structure exchibited less than one percent reflectivity in the wavelength range from 400 to 1170 nm with the following dimensions of the nanopillars: 200 nm height, 90 nm bottom width and 50 nm top width.

A performance increase from 10.4 % to 13.5 % in efficiency has been reported on poly-Si p-n junction solar cell with moth-eye coating [144]. This was mainly due to the increase in short circuit current produced by higher number of photons entering and absorbed in the p-n junction. Large scale outdoor experiment on moth-eye coated c-Si photovoltaic module yielded 5 % higher efficiency than for the uncoated one [145]. Furthermore, an increase from 27.77 % to 28.69 % in the efficiency of a GaAs solar cell induced by a moth-eye coating has been reported [146].

4.3.1 Fabrication and characterization

The fabrication of moth-eye antireflection coatings by UV-NIL process on AlInP surface was demonstrated in Ref. [P5]. AlInP has a very large band gap and high transparency. Therefore, it is widely used as a window layer on III-V multijunction solar cells in order to passivate the emitter [131]. The refractive index of AlInP is approximately three within a wide spectral range, which makes it a suitable material for grading the refractive index from air to the semiconductor solar cell, which has refractive indices around 3 – 3.5.

Three nanostructured samples (denoted as A-C) were fabricated on 1 µm thick AlInP layer grown by MBE on n-type GaAs(100) substrate. The master template was fabricated by an UV-NIL based lift-off process and consisted of nanocones in a square array [147]. The nanocone master template was, in turn, fabricated utilizing laser interference lithography patterned master template. The period of the cones was 300 nm, height was 190 nm and base diameter was 130 nm. First, the structure was transferred from UV-NIL resist (AMONIL, AMO GmbH) to SiN_x

hard mask using RIE. Second, ICP-RIE and $Cl_2/N_2/Ar$ based chemistry was utilized in AlInP etching. The dimensions of AlInP nanocones were tuned by changing the etch conditions. SEM images of the etched samples A-C are shown in Figure 4.3. The measures of the nanocones were (top diameter/base diameter/height) 30/170/370 nm (sample A), 50/220/370 nm (sample B) and 80/300/440 nm (sample C) [P5].

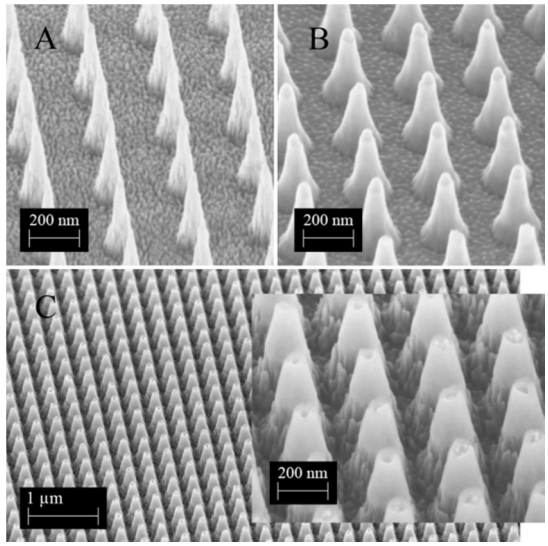

Figure 4.3: SEM images of moth-eye nanostructures on AlInP on the samples A, B and C.

The reflectivity of the nanostructured samples was measured within spectral range of 450 – 1650 nm. Figure 4.4 shows the reflectance spectra for samples A - C and for a reference sample having a planar, 1 µm thick AlInP on GaAs. The mean reflectivities within the spectral range of 450 – 1650 nm were 26.4 %, 14.6 %, 8.9 % and 2.7 % for the reference sample and samples A, B and C, respectively. The mean reflectivities were strongly reduced when the base diameter of the cones was increased. This behavior can be understood by the reduction of the flat area between the nanocones and by the reduction of the effective discontinuity of the refractive index, thus providing a smooth transition from air to semiconductor [P5].

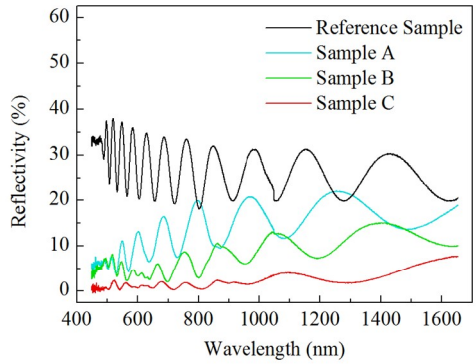

Figure 4.4: Reflectance spectra for the samples A, B, C and the reference sample.

A rather simple way to assess the optical losses induced by the AlInP nanostructure is to measure photoluminescence emitted from the underlying GaAs substrate, as we did on the sample C and the reference sample. The standard method where reflection and transmission measurements are used cannot be directly applied because of the high absorption of GaAs below 870 nm. We performed two separate measurements using excitation at 785 nm and at 532 nm. This method provides the information about the losses at the laser wavelengths and within the GaAs emission range. Corresponding PL intensities are shown in Figure 4.5(a) and (c). The measured GaAs PL intensity was clearly higher for sample C than for the reference sample for both of the excitation wavelengths. This can be interpreted as improved antireflective properties of the surface for both incident laser light and emitted PL. In order to assess the losses within the nanostructure we calculated equalized PL intensities using Equation (4.1) [P5]. This way it is possible to take into account the reflection of the incident laser beam (the first term), reflection of the GaAs PL emission (the second term) and the absorption of the laser light and PL emission in AlInP (the last term).

$$I_{PL}^{eq}(\lambda) = \frac{I_{PL}^{meas}(\lambda)}{1-R_{laser}} \times \frac{1}{1-R(\lambda)} \times \frac{1}{\exp\left[-(\alpha_{laser}+\alpha_{PL})x\right]} \tag{4.1}$$

where $I_{PL}^{eq}(\lambda)$ and $I_{PL}^{meas}(\lambda)$ are equalized and measured PL intensities, respectively, R_{laser} is the surface reflectivity at laser wavelength, $R(\lambda)$ is the wavelength dependent surface reflectivity, α_{laser} and α_{PL} are the absorption coefficients for incident laser and GaAs PL, respectively, and x is the effective thickness of the AlInP layer.

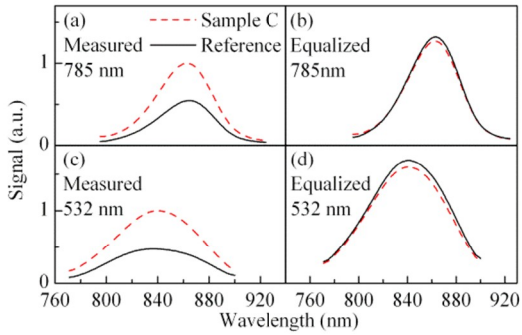

Figure 4.5: Measured and equalized GaAs PL intensities for excitations at 785 nm (a), (b) and at 532 nm (c), (d).

Wavelength dependent absorption coefficients for AlInP can be calculated from extinction coefficient measured by spectroscopic ellipsometer using Equation (4.2) [P5]. The extinction coefficient is shown in Figure 4.6(a).

$$\alpha_{laser,PL}(\lambda) = 4\pi\kappa(\lambda)/\lambda \tag{4.2}$$

where $\kappa(\lambda)$ is the extinction coefficient and λ is either the wavelength of the laser light or the PL emission. Equalized PL spectra are shown in Figure 4.5(b) and (d). After the equalization, PL spectra show almost similar behavior for both excitation wavelengths. It indicates that in addition to the absorption in AlInP, which was taken into account in Equation (4.1), there were no other major loss mechanisms, although the surface area has increased by more than a factor of three.

4.3.2 Simulation

Finite-difference time-domain (FDTD) method and a free-software package called MEEP were utilized to simulate the reflectivity of the nanostructured surfaces [148]. When using FDTD, the parameters of the structures can be applied directly without an effective index approximation, which is inevitable with many other simulation techniques [141-143]. AlInP properties were modeled by fitting complex dielectric functions to the permittivities calculated from the measured refractive index and extinction coefficient. The refractive index and the extinction coefficient measured by spectroscopic ellipsometer are shown in Figure 4.6(a). The permittivity of GaAs was obtained from the data in Ref. [149]. The spatial dimensions were acquired from AFM and SEM measurements. Figure 4.6(b) shows one block of the simulated structure for

sample C. The structure was assumed to be periodic in lateral directions. A good agreement between the measured and simulated reflectance spectra was achieved, which is shown in Figure 4.6(c). Mean values for the measured and simulated reflectivities within the spectral range of 450 – 1650 nm are summarized in Table 4.1.

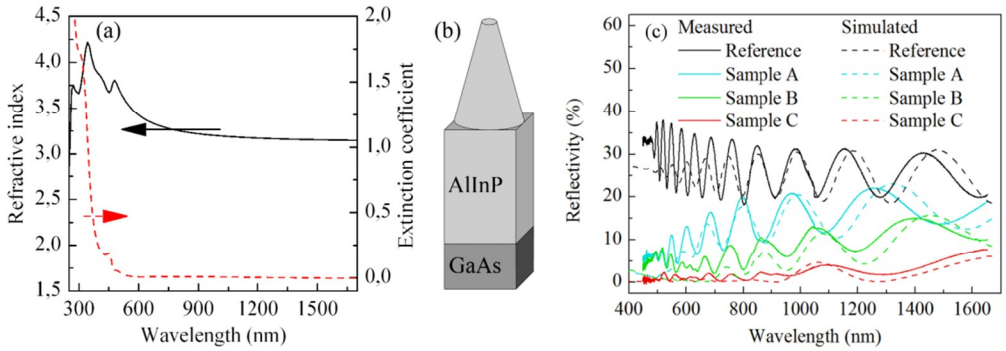

Figure 4.6: (a) Measured refractive index (solid line) and extinction coefficient (dashed line) for AlInP. (b) A schematic illustration of the simulated structure used for sample C. (c) Measured (solid lines) and simulated (dashed lines) reflectance spectra for the samples A, B, C and the reference sample.

Table 4.1: Arithmetic mean values for the measured and simulated reflectivities within the spectral range of 450 - 1650 nm for samples A, B, C and the reference sample.

	Reference	Sample A	Sample B	Sample C
Simulation	25.3 %	13.6 %	6.7 %	1.7 %
Measurement	26.4 %	14.6 %	8.9 %	2.7 %

4.3.3 Integration onto solar cells

In order to study the real performance of the nanostructured moth-eye coating, it was fabricated on the surface of a dilute nitride GaInAsN p-i-n solar cell [P6]. The solar cell was grown by MBE and it was mainly absorbing light within the spectral range of 500 – 1200 nm. Thickness of the AlInP layer was increased from typical a couple of tens of nanometers to 600 nm. This allowed the etching of the nanocones and left an intact AlInP layer underneath the cones. The effective thickness of the AlInP layer measured from the cross sectional SEM images was estimated to be around 300 nm after etching. Further optimization of the AlInP thickness would

have led to even lower effective thickness. AlInP layers can be either monolithically grown on the solar cells by MBE [P6] or by regrowth techniques using the cleaning procedures described in section 3.3.2 [150]. In addition to the structure described in section 4.3.1, we have observed that thin layers of SiN_x grown by plasma-enhanced chemical vapor deposition (PECVD) can be used for surface passivation and improving the surface morphology. Here, we used a 60 nm SiN_x layer grown directly on the nanocones. Figure 4.7 shows SEM images of SiN_x-coated moth-eye nanostructures on a solar cell surface.

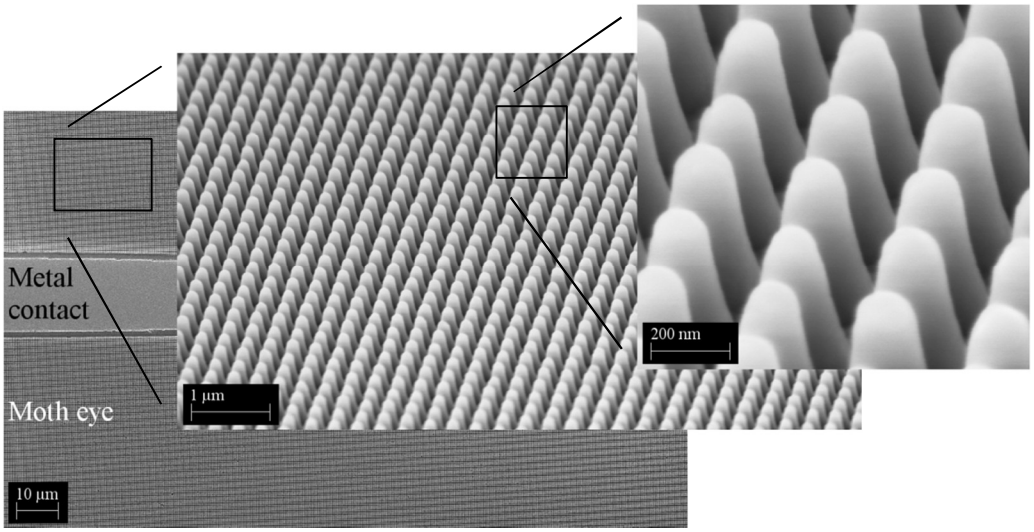

Figure 4.7: SEM images of the SiN_x coated moth-eye nanostructure on a solar cell surface. The sample is tilted in the insets.

Incident angle dependent specular reflectivity was measured from the moth-eye coated solar cell and from a reference solar cell having an uncoated AlInP surface or a standard SiN_x/SiO_2 antireflection coating. Figure 4.8(a) shows the angle dependent reflectance spectra for the moth-eye coated solar cell and reflectance spectra at 8° for uncoated and SiN_x/SiO_2 coated reference solar cell. Arithmetic mean values for the reflectivities within the spectral ranges of 320 – 1350 nm and 320 – 1800 nm are summarized in Figure 4.8(b). For near normal incidence, the mean reflectivity was reduced from 27 % for a bare AlInP surface to 13 % for SiN_x/SiO_2 coating and down to 2 % for the moth-eye-coated solar cell. SiN_x/SiO_2 coating was optimized to have minimum reflectivity at 600 nm, where also the reflectivity of the moth-eye coating was the lowest. This was advantageous since the spectral irradiance of the AM1.5G solar spectrum is the highest around 500 – 600 nm [P6]. The mean reflectivity of the moth-eye coated solar cell

was as low as 2.1 % at near normal incidence and remained below 5 % for incident angles up to 45° within the spectral range of 320 – 1800 nm. This is a valuable property in concentrator systems where the incident angle is increased by lenses or mirrors.

After the reflectivity measurements, metal contacts were processed on the solar cells by standard optical lithography and current-voltage characteristics were measured under simulated solar illumination (Oriel Instruments). Figure 4.9 shows the current-voltage measurements of the solar cells with three types of coatings. We observed an increase of 30 % in the short circuit current for the moth-eye coated solar cell when compared to an uncoated solar cell and an increase of 5.3 % when compared to a SiN_x/SiO_2 coated solar cell. The increase in current was attributed to the reduction in the reflectivity which allowed more photons to enter the active region and generate more charge carriers as compared to the reference samples. Furthermore, the current-voltage measurements implicate that the optical losses induced by the moth-eye coating are low.

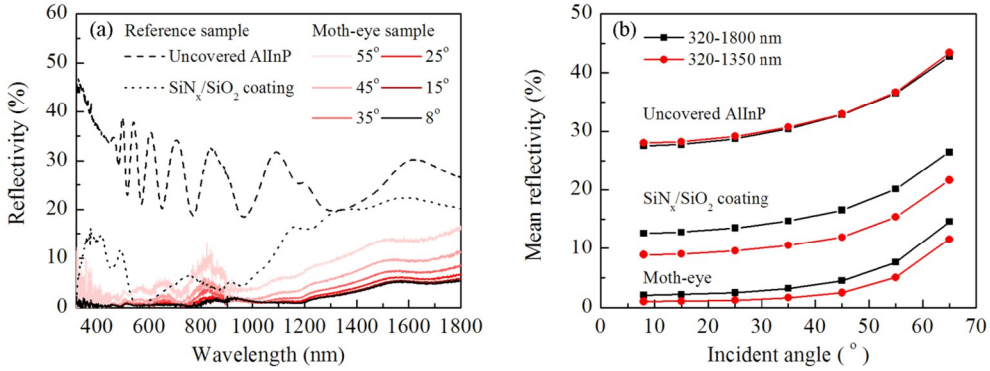

Figure 4.8: (a) Incident angle-dependent reflectivities of the moth-eye coated solar cell and reflectance spectra of the reference sample with uncovered AlInP and SiN_x/SiO_2 coating. (b) Arithmetic mean reflectivities of the moth-eye coated solar cell and reference solar cell with uncovered AlInP and SiN_x/SiO_2 coating within spectral ranges of 320 – 1800 nm and 320 – 1350 nm.

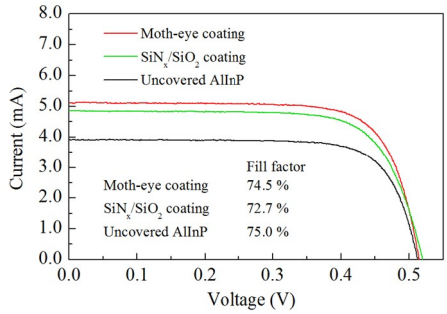

Figure 4.9: Current-voltage characteristics of the moth-eye coated GaInAsN solar cell and reference solar cell with uncovered AlInP and SiN_x/SiO_2 coatings.

In addition to a single junction solar cell, the moth-eye coating was applied on a solar cell having three junctions consisting of GaInP/GaAs/GaInAsN. The process described above was utilized in fabrication, but the UV-NIL master template was patterned by LIL at Soochow University, Suzhou, China, and etched at Suzhou Institute of Nano-Tech and Nano-Bionics, Chinese Academy of Sciences, Suzhou, China, and at ORC, Tampere, Finland. Figure 4.10 shows current-voltage characteristics of the triple junction solar cell with moth-eye coating and with an optimized TiO_2/SiO_2 antireflection coating measured under real sun exposure with intensity of 860 W/m^2 measured by a commercial pyranometer (Kipp&Zonen). The photogenerated current was increased consistent with results for single junction solar cell. It led to an improvement of 2 percentage points in efficiency, from 22 % for TiO_2/SiO_2 coated solar cell up to 24 % for the moth-eye coated solar cell calculated from the active areas. Further development in solar cell material fabrication and the integration of the moth-eye etching process along with the fabrication of metal contacts are needed to achieve record high efficiencies.

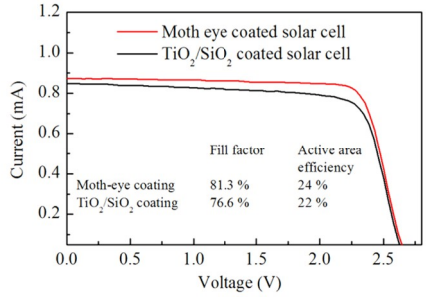

Figure 4.10: Current-voltage characteristics of the moth-eye coated triple junction solar cell and a reference solar cell with TiO_2/SiO_2 coating.

Chapter 5

5 Conclusions

The main achievements of this work were the technological development of nanoimprint lithography based patterning processes for site-controlled epitaxy of single quantum dots and for nanostructured antireflection coatings. The key parameters and properties of both applications were assessed by structural, optical and electrical measurements.

Site-controlled QDs on various pattern geometries were fabricated, the focus being on single QDs. Special issues related to surface cleaning and native oxide removal when combining UV-NIL and MBE were addressed. Structural and optical properties of single QDs in etched GaAs pits were characterized. The optical properties measured as a function of the excitation power, temperature, time and polarization indicated that the site-controlled QDs fabricated by the combination of UV-NIL and MBE are strong candidates for single photon quantum emitters. Single QD occupation probability of 90 % and exciton emission linewidths down to 32 µeV were achieved. The effect of the pattern morphology and the growth parameters provide several tuning mechanisms, but also optimization challenges for different applications. These results pave the way for large scale quantum dot based devices. Further research especially on the optimization of the electrical properties is required. For example, an additional in-situ atomic hydrogen cleaning step could still improve the operation. In terms of pattern uniformity and enhanced selectivity for the QD nucleation, the etched GaAs(111)B surface offers an attractive direction for subsequent studies.

The fabrication of the nanostructured antireflection coatings on AlInP surface by UV-NIL was demonstrated. The structuring process was aiming towards the integration with high efficiency

multijunction solar cells, in order to further improve their efficiency. AlInP was fabricated onto the solar cell surface either monolithically or by utilizing regrowth process equivalent to site-controlled QDs. The reflectivity of different pattern geometries was modeled numerically. The losses induced by the surface were assessed by photoluminescence measurements. An average reflectivity of 2.1 % within the spectral range of 320 – 1800 nm was achieved and the value remained below 5 % for incident angles up to 45°. A clear increase in the solar cell performance as compared to the regular thin film coatings was observed when integrating the nanostructured coating on a single junction and triple junction solar cells. Further development in solar cell material fabrication and improved integration of the nanostructured coating with the preparation of metal contacts is needed to achieve record high conversion efficiencies.

Bibliography

[1] R. P. Feynman, "There's plenty of room at the bottom," *Engineering and Science*, vol. 23, no. 5, pp. 22-36, 1960.

[2] J. Ramsden, *Nanotechnology: an introduction*, William Andrew Pub, 2011.

[3] S. Y. Chou, P. R. Krauss, and P. J. Renstrom, "Imprint of sub-25 nm vias and trenches in polymers," *Applied Physics Letters*, vol. 67, no. 21, pp. 3114-3116, 1995.

[4] "10 emerging technologies that will change the world," *MIT Technology review*, pp. 33-56, 2003.

[5] "International Technology Roadmap for Semiconductors, 2012 update," http://www.itrs.net/Links/2012ITRS/2012Chapters/2012Overview.pdf, Accessed: 27.3.2013.

[6] F. Hua, Y. Sun, A. Gaur, M. A. Meitl, L. Bilhaut, L. Rotkina, J. Wang, P. Geil, M. Shim, and J. A. Rogers, "Polymer imprint lithography with molecular-scale resolution," *Nano Letters*, vol. 4, no. 12, pp. 2467-2471, 2004.

[7] T. Ohta, M. Hennesey, D. Strand, D. Jablonsky, B. Walton, and B. Clark, "High Quality Film Nanoimprint Technology for Blu-Ray Disc (BD) Media," *Magnetics, IEEE Transactions on*, vol. 43, no. 2, pp. 836-839, 2007.

[8] J. H. Chang, F. S. Cheng, C. C. Chao, Y. C. Weng, S. Y. Yang, and L. A. Wang, "Direct imprinting using soft mold and gas pressure for large area and curved surfaces," *Journal of Vacuum Science & Technology A: Vacuum, Surfaces, and Films*, vol. 23, no. 6, pp. 1687-1690, 2005.

[9] J. van der Ziel, R. Dingle, R. Miller, W. Wiegmann, and W. Nordland, "Laser oscillation from quantum states in very thin GaAs-Al0. 2Ga0. 8As multilayer structures," *Applied Physics Letters*, vol. 26, pp. 463, 1975.

[10] M. Henini, *Handbook of self assembled semiconductor nanostructures for novel devices in photonics and electronics*, Elsevier Science Limited, 2008.

[11] M. A. Green, K. Emery, Y. Hishikawa, W. Warta, and E. D. Dunlop, "Solar cell efficiency tables (version 41)," *Progress in Photovoltaics: Research and Applications*, vol. 21, no. 1, pp. 1-11, 2013.

[12] U. Plachetka, M. Bender, A. Fuchs, B. Vratzov, T. Glinsner, F. Lindner, and H. Kurz, "Wafer scale patterning by soft UV-nanoimprint lithography," *Microelectronic Engineering*, vol. 73, pp. 167-171, 2004.

[13] J. Viheriälä, "Nanoimprint Lithography–A Next Generation Patterning Method for Nanophotonics," Ph.D. Thesis, Tampere University of Technology, 2010 http://URN.fi/URN:NBN:fi:tty-201008191294.

[14] J. Viheriälä, M. Viljanen, J. Kontio, T. Leinonen, J. Tommila, M. Dumitrescu, T. Niemi, and M. Pessa, "Soft stamp ultraviolet-nanoimprint lithography for fabrication of laser diodes," *Journal of Micro/Nanolithography, MEMS, and MOEMS*, vol. 8, no. 3, pp. 033004-033004, 2009.

[15] H. Schmid, B. Michel, "Siloxane polymers for high-resolution, high-accuracy soft lithography," *Macromolecules*, vol. 33, no. 8, pp. 3042-3049, 2000.

[16] J. Viheriälä, J. Tommila, T. Leinonen, M. Dumitrescu, L. Toikkanen, T. Niemi, and M. Pessa, "Applications of UV-nanoimprint soft stamps in fabrication of single-frequency diode lasers," *Microelectronic Engineering*, vol. 86, no. 3, pp. 321-324, 2009.

[17] S. H. Ahn, L. J. Guo, "Large-area roll-to-roll and roll-to-plate nanoimprint lithography: a step toward high-throughput application of continuous nanoimprinting," *ACS nano*, vol. 3, no. 8, pp. 2304-2310, 2009.

[18] T. Michaelson, S. Sreenivasan, J. Ekerdt, and C. Willson, "Step and flash imprint lithography: a new approach to high-resolution patterning," *in SPIE Conference on Emerging Lithographic Technologies Ill*, vol. 3676, pp. 379-389, 1999.

[19] T. Haatainen, J. Ahopelto, "Pattern transfer using step&stamp imprint lithography," *Physica Scripta*, vol. 67, no. 4, pp. 357, 2006.

[20] J. N. Helbert, *Handbook of VLSI Microlithography - Principles, Technology and Applications (2nd Edition)*, William Andrew Publishing/Noyes, 2001.

[21] R. Seisyan, "Nanolithography in microelectronics: A review," *Technical Physics*, vol. 56, no. 8, pp. 1061-1073, 2011.

[22] W. Hu, K. Sarveswaran, M. Lieberman, and G. H. Bernstein, "High-resolution electron beam lithography and DNA nano-patterning for molecular QCA," *Nanotechnology, IEEE Transactions on*, vol. 4, no. 3, pp. 312-316, 2005.

[23] T. Chang, M. Mankos, K. Y. Lee, and L. P. Muray, "Multiple electron-beam lithography," *Microelectronic Engineering*, vol. 57, pp. 117-135, 2001.

[24] C. Volkert, A. Minor, "Focused ion beam microscopy and micromachining," *MRS Bull*, vol. 32, no. 5, pp. 389-395, 2007.

[25] C. Lu, R. Lipson, "Interference lithography: a powerful tool for fabricating periodic structures," *Laser & Photonics Reviews*, vol. 4, no. 4, pp. 568-580, 2009.

[26] T. Bloomstein, M. F. Marchant, S. Deneault, D. E. Hardy, and M. Rothschild, "22-nm immersion interference lithography," *Optics Express*, vol. 14, no. 14, pp. 6434-6443, 2006.

[27] M. Müller, T. Fiedler, R. Gröger, T. Koch, S. Walheim, C. Obermair, and T. Schimmel, "Controlled structuring of mica surfaces with the tip of an atomic force microscope by mechanically induced local etching," *Surface and Interface Analysis*, vol. 36, no. 2, pp. 189-192, 2004.

[28] S. W. Hla, K. F. Braun, and K. H. Rieder, "Single-atom manipulation mechanisms during a quantum corral construction," *Physical Review B*, vol. 67, no. 20, pp. 201402, 2003.

[29] W. Shim, A. B. Braunschweig, X. Liao, J. Chai, J. K. Lim, G. Zheng, and C. A. Mirkin, "Hard-tip, soft-spring lithography," *Nature*, vol. 469, no. 7331, pp. 516-520, 2011.

[30] S. Lloyd, "A potentially realizable quantum computer," *Science*, vol. 261, no. 5128, pp. 1569-1571, 1993.

[31] C. H. Bennett, "Quantum cryptography using any two nonorthogonal states," *Physical Review Letters*, vol. 68, no. 21, pp. 3121-3124, 1992.

[32] A. Beige, B. G. Englert, C. Kurtsiefer, and H. Weinfurter, "Secure communication with a publicly known key," *Acta Phys.Pol.A*, vol. 101, pp. 357, 2002.

[33] K. Boström, T. Felbinger, "Deterministic secure direct communication using entanglement," *Physical Review Letters*, vol. 89, no. 18, pp. 187902, 2002.

[34] M. Pelton, Y. Yamamoto, "Ultralow threshold laser using a single quantum dot and a microsphere cavity," *Physical Review A*, vol. 59, no. 3, pp. 2418-2421, 1999.

[35] C. J. Wang, L. Y. Lin, and B. A. Parviz, "Modeling and simulation for a nano-photonic quantum dot waveguide fabricated by DNA-directed self-assembly," *Selected Topics in Quantum Electronics, IEEE Journal of*, vol. 11, no. 2, pp. 500-509, 2005.

[36] C. H. Bennett, D. P. DiVincenzo, "Quantum information and computation," *Nature*, vol. 404, no. 6775, pp. 247-255, 2000.

[37] A. Imamoglu, D. D. Awschalom, G. Burkard, D. P. DiVincenzo, D. Loss, M. Sherwin, and A. Small, "Quantum information processing using quantum dot spins and cavity QED," *Physical Review Letters*, vol. 83, no. 20, pp. 4204-4207, 1999.

[38] G. Milburn, "Quantum optical Fredkin gate," *Physical Review Letters*, vol. 62, no. 18, pp. 2124-2127, 1989.

[39] M. Atatüre, J. Dreiser, A. Badolato, A. Högele, K. Karrai, and A. Imamoglu, "Quantum-dot spin-state preparation with near-unity fidelity," *Science*, vol. 312, no. 5773, pp. 551-553, 2006.

[40] J. Elzerman, R. Hanson, L. H. W. Van Beveren, B. Witkamp, L. Vandersypen, and L. P. Kouwenhoven, "Single-shot read-out of an individual electron spin in a quantum dot," *Nature*, vol. 430, no. 6998, pp. 431-435, 2004.

[41] D. Press, T. D. Ladd, B. Zhang, and Y. Yamamoto, "Complete quantum control of a single quantum dot spin using ultrafast optical pulses," *Nature*, vol. 456, no. 7219, pp. 218-221, 2008.

[42] E. Knill, R. Laflamme, and G. J. Milburn, "A scheme for efficient quantum computation with linear optics," *Nature*, vol. 409, no. 6816, pp. 46-52, 2001.

[43] J. L. O'Brien, G. J. Pryde, A. G. White, T. C. Ralph, and D. Branning, "Demonstration of an all-optical quantum controlled-NOT gate," *Nature*, vol. 426, no. 6964, pp. 264-267, 2003.

[44] J. Petta, A. Johnson, J. Taylor, E. Laird, A. Yacoby, M. Lukin, C. Marcus, M. Hanson, and A. Gossard, "Coherent manipulation of coupled electron spins in semiconductor quantum dots," *Science*, vol. 309, no. 5744, pp. 2180-2184, 2005.

[45] T. Stace, G. J. Milburn, and C. Barnes, "Entangled two-photon source using biexciton emission of an asymmetric quantum dot in a cavity," *Physical Review B*, vol. 67, no. 8, pp. 085317, 2003.

[46] G. Chen, T. Stievater, E. Batteh, X. Li, D. Steel, D. Gammon, D. Katzer, D. Park, and L. Sham, "Biexciton quantum coherence in a single quantum dot," *Physical Review Letters*, vol. 88, no. 11, pp. 117901, 2002.

[47] O. Benson, C. Santori, M. Pelton, and Y. Yamamoto, "Regulated and entangled photons from a single quantum dot," *Physical Review Letters*, vol. 84, no. 11, pp. 2513-2516, 2000.

[48] R. Stevenson, R. Young, P. Atkinson, K. Cooper, D. Ritchie, and A. Shields, "A semiconductor source of triggered entangled photon pairs," *Nature*, vol. 439, no. 7073, pp. 179-182, 2006.

[49] A. Dousse, J. Suffczyński, A. Beveratos, O. Krebs, A. Lemaître, I. Sagnes, J. Bloch, P. Voisin, and P. Senellart, "Ultrabright source of entangled photon pairs," *Nature*, vol. 466, no. 7303, pp. 217-220, 2010.

[50] C. Salter, R. Stevenson, I. Farrer, C. Nicoll, D. Ritchie, and A. Shields, "An entangled-light-emitting diode," *Nature*, vol. 465, no. 7298, pp. 594-597, 2010.

[51] W. Gao, P. Fallahi, E. Togan, J. Miguel-Sanchez, and A. Imamoglu, "Observation of entanglement between a quantum dot spin and a single photon," *Nature*, vol. 491, no. 7424, pp. 426-430, 2012.

[52] B. G. Streetman, S. Banerjee, *Solid state electronic devices, 5th edition*, Prentice Hall, 2000.

[53] D. Leonard, M. Krishnamurthy, C. Reaves, S. Denbaars, and P. Petroff, "Direct formation of quantum-sized dots from uniform coherent islands of InGaAs on GaAs surfaces," *Applied Physics Letters*, vol. 63, no. 23, pp. 3203-3205, 1993.

[54] T. Ishikawa, S. Kohmoto, and K. Asakawa, "Site control of self-organized InAs dots on GaAs substrates by in situ electron-beam lithography and molecular-beam epitaxy," *Applied Physics Letters*, vol. 73, no. 12, pp. 1712-1714, 1998.

[55] J. Martín-Sánchez, G. Muñoz-Matutano, J. Herranz, J. Canet-Ferrer, B. Alén, Y. González, P. Alonso-González, D. Fuster, L. González, and J. Martínez-Pastor, "Single photon emission from site-controlled InAs quantum dots grown on GaAs (001) patterned substrates," *ACS nano*, vol. 3, no. 6, pp. 1513-1517, 2009.

[56] Y. Morishita, M. Ishiguro, S. Miura, and Y. Enmei, "Molecular-beam epitaxy of InAs on GaAs substrates with hole arrays patterned by focused ion beam," *Journal of Crystal Growth*, vol. 237, pp. 1291-1295, 2002.

[57] C. Schneider, M. Straub, T. Sunner, A. Huggenberger, D. Wiener, S. Reitzenstein, M. Kamp, S. Hofling, and A. Forchel, "Lithographic alignment to site-controlled quantum dots for device integration," *Applied Physics Letters*, vol. 92, no. 18, pp. 183101-183101-3, 2008.

[58] J. Skiba-Szymanska, A. Jamil, I. Farrer, M. B. Ward, C. A. Nicoll, D. J. P. Ellis, J. P. Griffiths, D. Anderson, G. A. C. Jones, and D. A. Ritchie, "Narrow emission linewidths of positioned InAs quantum dots grown on pre-patterned GaAs (100) substrates," *Nanotechnology*, vol. 22, no. 6, pp. 065302, 2011.

[59] K. D. Jöns, P. Atkinson, M. Müller, M. Heldmaier, S. M. Ulrich, O. G. Schmidt, and P. Michler, "Triggered indistinguishable single-photons with narrow linewidths from site-controlled quantum dots," *Nano Letters*, 2012.

[60] M. Baier, E. Pelucchi, E. Kapon, S. Varoutsis, M. Gallart, I. Robert-Philip, and I. Abram, "Single photon emission from site-controlled pyramidal quantum dots," *Applied Physics Letters*, vol. 84, no. 5, pp. 648-650, 2004.

[61] S. Kiravittaya, H. Heidemeyer, and O. Schmidt, "Growth of three-dimensional quantum dot crystals on patterned GaAs (001) substrates," *Physica E: Low-dimensional Systems and Nanostructures*, vol. 23, no. 3, pp. 253-259, 2004.

[62] H. S. Chang, C. M. Hsu, W. Y. Chen, T. P. Hsieh, J. I. Chyi, and T. M. Hsu, "High extractive single-photon emissions from InGaAs quantum dots on a GaAs pyramid-like multifaceted structure," *Nanotechnology*, vol. 19, no. 4, pp. 045714, 2008.

[63] S. Birudavolu, N. Nuntawong, G. Balakrishnan, Y. Xin, S. Huang, S. Lee, S. Brueck, C. Hains, and D. Huffaker, "Selective area growth of InAs quantum dots formed on a patterned GaAs substrate," *Applied Physics Letters*, vol. 85, no. 12, pp. 2337-2339, 2004.

[64] A. Strittmatter, A. Schliwa, J. H. Schulze, T. Germann, A. Dreismann, O. Hitzemann, E. Stock, I. Ostapenko, S. Rodt, and W. Unrau, "Lateral positioning of InGaAs quantum dots using a buried stressor," *Applied Physics Letters*, vol. 100, no. 9, pp. 093111-093111-3, 2012.

[65] C. Schneider, T. Heindel, A. Huggenberger, T. Niederstrasser, S. Reitzenstein, A. Forchel, S. Hofling, and M. Kamp, "Microcavity enhanced single photon emission from an electrically driven site-controlled quantum dot," *Applied Physics Letters*, vol. 100, no. 9, pp. 091108-091108-4, 2012.

[66] T. Sünner, C. Schneider, M. Strauß, A. Huggenberger, D. Wiener, S. Höfling, M. Kamp, and A. Forchel, "Scalable fabrication of optical resonators with embedded site-controlled quantum dots," *Optics Letters*, vol. 33, no. 15, pp. 1759-1761, 2008.

[67] P. Gallo, M. Felici, B. Dwir, K. Atlasov, K. Karlsson, A. Rudra, A. Mohan, G. Biasiol, L. Sorba, and E. Kapon, "Integration of site-controlled pyramidal quantum dots and photonic crystal membrane cavities," *Applied Physics Letters*, vol. 92, no. 26, pp. 263101-263101-3, 2008.

[68] J. Tommila, "The development of nanoimprint lithography for nanophotonic applications," Master's thesis, Tampere University of Technology, 2009.

[69] S. M. Rossnagel, J. J. Cuomo, and W. D. Westwood, *Handbook of plasma processing technology: fundamentals, etching, deposition, and surface interactions*, William Andrew Publishing/Noyes, 1990.

[70] C. Surdu-Bob, S. Saied, and J. Sullivan, "An X-ray photoelectron spectroscopy study of the oxides of GaAs," *Applied Surface Science*, vol. 183, no. 1, pp. 126-136, 2001.

[71] T. Van Buuren, M. Weilmeier, I. Athwal, K. Colbow, J. Mackenzie, T. Tiedje, P. Wong, and K. Mitchell, "Oxide thickness effect and surface roughening in the desorption of the oxide from GaAs," *Applied Physics Letters*, vol. 59, no. 4, pp. 464-466, 1991.

[72] Y. Asaoka, "Desorption process of GaAs surface native oxide controlled by direct Ga-beam irradiation," *Journal of Crystal Growth*, vol. 251, no. 1, pp. 40-45, 2003.

[73] O. Tereshchenko, S. Chikichev, and A. Terekhov, "Atomic structure and electronic properties of HCl–isopropanol treated and vacuum annealed GaAs (100) surface," *Applied Surface Science*, vol. 142, no. 1, pp. 75-80, 1999.

[74] P. Laukkanen, M. Kuzmin, R. Perälä, R. L. Vaara, and I. Väyrynen, "Scanning tunneling microscopy study of GaAs (1 0 0) surface prepared by HCl-isopropanol treatment," *Applied Surface Science*, vol. 206, no. 1, pp. 2-7, 2003.

[75] H. C. Kan, R. Ankam, S. Shah, K. Micholsky, T. Tadayyon-Eslami, L. Calhoun, and R. Phaneuf, "Evolution of patterned GaAs (001) during homoepitaxial growth: Size versus spacing," *Physical Review B*, vol. 73, no. 19, pp. 195410, 2006.

[76] A. Balzarotti, "The evolution of self-assembled InAs/GaAs (001) quantum dots grown by growth-interrupted molecular beam epitaxy," *Nanotechnology*, vol. 19, no. 50, pp. 505701, 2008.

[77] P. Atkinson, O. G. Schmidt, S. P. Bremner, and D. A. Ritchie, "Formation and ordering of epitaxial quantum dots," *Comptes Rendus Physique*, vol. 9, no. 8, pp. 788-803, 2008.

[78] A. Hartmann, L. Loubies, F. Reinhardt, and E. Kapon, "Self-limiting growth of quantum dot heterostructures on nonplanar {111} B substrates," *Applied Physics Letters*, vol. 71, no. 10, pp. 1314-1316, 1997.

[79] K. Leifer, E. Pelucchi, S. Watanabe, F. Michelini, B. Dwir, and E. Kapon, "Narrow (= 4 meV) inhomogeneous broadening and its correlation with confinement potential of pyramidal quantum dot arrays," *Applied Physics Letters*, vol. 91, no. 8, pp. 081106-081106-3, 2007.

[80] M. Felici, P. Gallo, A. Mohan, B. Dwir, A. Rudra, and E. Kapon, "Site-Controlled InGaAs Quantum Dots with Tunable Emission Energy," *Small*, vol. 5, no. 8, pp. 938-943, 2009.

[81] T. Hakkarainen, J. Tommila, A. Schramm, A. Tukiainen, R. Ahorinta, M. Dumitrescu, and M. Guina, "Structural characterization of InAs quantum dot chains grown by molecular beam epitaxy on nanoimprint lithography patterned GaAs (100)," *Nanotechnology*, vol. 22, no. 29, pp. 295604, 2011.

[82] T. Hakkarainen, J. Tommila, A. Schramm, A. Tukiainen, R. Ahorinta, M. Dumitrescu, and M. Guina, "Structural and optical properties of InAs quantum dot chains grown on nanoimprint lithography structured GaAs with different pattern orientations," *Applied Physics Letters*, vol. 97, no. 17, pp. 173107-173107-3, 2010.

[83] T. Hakkarainen, V. Polojärvi, A. Schramm, J. Tommila, and M. Guina, "The influence of post-growth annealing on the optical properties of InAs quantum dot chains grown on pre-patterned GaAs (100)," *Nanotechnology*, vol. 23, no. 11, pp. 115702, 2012.

[84] T. Hakkarainen, A. Schramm, J. Tommila, and M. Guina, "The effect of InGaAs strain-reducing layer on the optical properties of InAs quantum dot chains grown on patterned GaAs (100)," *Journal of Applied Physics*, vol. 111, no. 1, pp. 014306-014306-6, 2012.

[85] S. Lee, K. Malloy, L. Dawson, and S. Brueck, "Selective growth and associated faceting and lateral overgrowth of GaAs on a nanoscale limited area bounded by a SiO mask in molecular beam epitaxy," *Journal of Applied Physics*, vol. 92, pp. 6567, 2002.

[86] A. Tukiainen, J. Viheriälä, T. Niemi, T. Rytkönen, J. Kontio, and M. Pessa, "Selective growth experiments on gallium arsenide (100) surfaces patterned using UV-nanoimprint lithography," *Microelectronics Journal*, vol. 37, no. 12, pp. 1477-1480, 2006.

[87] A. Tukiainen, J. Tommila, A. Aho, A. Schramm, J. Viheriala, R. Ahorinta, M. Dumitrescu, M. Pessa, and M. Guina, "Selective growth of GaAs nanostructures and subsequent guided self-assembly of InAs quantum dots on nanoimprint lithography patterned SiO2/GaAs substrates," *Journal of Crystal Growth*, vol. 323, no. 1, pp. 201-205, 2011.

[88] W. Metaferia, J. Tommila, C. Junesand, H. Kataria, C. Hu, M. Guina, T. Niemi, and S. Lourdudoss, "Selective area heteroepitaxy through nanoimprint lithography for large area InP on Si," *Physica Status Solidi C*, vol. 9, no. 7, pp. 1610-1613, 2012.

[89] W. Metaferia, J. Tommila, H. Kataria, C. Junesand, Y. Sun, M. Guina, T. Niemi, and S. Lourdudoss, "Selective area heteroepitaxy of InP nanopyramidal frusta on Si for nanophotonics," *in International Conference on Indium Phosphide and Related Materials (IPRM)*, pp. 81-84, 2012.

[90] M. D. Birowosuto, H. Sumikura, S. Matsuo, H. Taniyama, P. J. van Veldhoven, R. Nötzel, and M. Notomi, "Fast Purcell-enhanced single photon source in 1,550-nm telecom band from a resonant quantum dot-cavity coupling," *Nature Scientific Reports*, vol. 2, pp. 321, 2012.

[91] I. Itskevich, M. Skolnick, D. Mowbray, I. Trojan, S. Lyapin, L. Wilson, M. Steer, M. Hopkinson, L. Eaves, and P. Main, "Excited states and selection rules in self-assembled InAs/GaAs quantum dots," *Physical Review B*, vol. 60, no. 4, pp. 2185-2188, 1999.

[92] I. Saïdi, K. Sellami, M. Yahyaoui, C. Testelin, and K. Boujdaria, "Electron and hole energy levels in InAs/GaAs quantum dots: Size and magnetic field effects," *Journal of Applied Physics*, vol. 109, no. 3, pp. 033703-033703-7, 2011.

[93] N. Tang, "Effect of size non-uniformity on photoluminescence from ensembles of InAs quantum dots embedded in GaAs," *Journal of Materials Science*, vol. 42, no. 16, pp. 6913-6916, 2007.

[94] C. Santori, M. Pelton, G. Solomon, Y. Dale, and Y. Yamamoto, "Triggered single photons from a quantum dot," *Physical Review Letters*, vol. 86, no. 8, pp. 1502-1505, 2001.

[95] E. Dekel, D. Gershoni, E. Ehrenfreund, J. M. Garcia, and P. M. Petroff, "Carrier-carrier correlations in an optically excited single semiconductor quantum dot," *Physical Review B*, vol. 61, no. 16, pp. 11009, 2000.

[96] J. Finley, A. Ashmore, A. Lemaître, D. Mowbray, M. Skolnick, I. Itskevich, P. Maksym, M. Hopkinson, and T. Krauss, "Charged and neutral exciton complexes in individual self-assembled In(Ga)As quantum dots," *Physical Review B*, vol. 63, no. 7, pp. 073307, 2001.

[97] J. Finley, D. Mowbray, M. Skolnick, A. Ashmore, C. Baker, A. Monte, and M. Hopkinson, "Fine structure of charged and neutral excitons in InAs-Al0.6Ga0.4As quantum dots," *Physical Review B*, vol. 66, no. 15, 2002.

[98] M. Bayer, A. Forchel, "Temperature dependence of the exciton homogeneous linewidth in In0.60Ga0.40As/GaAs self-assembled quantum dots," *Physical Review B*, vol. 65, no. 4, pp. 041308, 2002.

[99] K. Hennessy, A. Badolato, M. Winger, D. Gerace, M. Atatüre, S. Gulde, S. Fält, E. L. Hu, and A. Imamoglu, "Quantum nature of a strongly coupled single quantum dot–cavity system," *Nature*, vol. 445, no. 7130, pp. 896-899, 2007.

[100] J. Tommila, A. Schramm, T. V. Hakkarainen, E. Heinonen, M. Dumitrescu, and M. Guina, "Properties of InAs Quantum Dots in Nanoimprint Lithography Patterned GaAs Pits," *in Conference on Lasers and Electro-Optics, CLEO: 2013, San Jose, CA*, 2013.

[101] K. Brunner, G. Abstreiter, G. Böhm, G. Tränkle, and G. Weimann, "Sharp-line photoluminescence and two-photon absorption of zero-dimensional biexcitons in a GaAs/AlGaAs structure," *Physical Review Letters*, vol. 73, no. 8, pp. 1138-1141, 1994.

[102] S. Kaiser, T. Mensing, L. Worschech, F. Klopf, J. Reithmaier, and A. Forchel, "Optical spectroscopy of single InAs/InGaAs quantum dots in a quantum well," *Applied Physics Letters*, vol. 81, no. 26, pp. 4898-4900, 2002.

[103] B. Alloing, C. Zinoni, V. Zwiller, L. Li, C. Monat, M. Gobet, G. Buchs, A. Fiore, E. Pelucchi, and E. Kapon, "Growth and characterization of single quantum dots emitting at 1300 nm," *Applied Physics Letters*, vol. 86, no. 10, pp. 101908-101908-3, 2005.

[104] R. Thompson, R. Stevenson, A. Shields, I. Farrer, C. Lobo, D. Ritchie, M. Leadbeater, and M. Pepper, "Single-photon emission from exciton complexes in individual quantum dots," *Physical Review B*, vol. 64, no. 20, pp. 201302, 2001.

[105] C. Santori, G. S. Solomon, M. Pelton, and Y. Yamamoto, "Time-resolved spectroscopy of multiexcitonic decay in an InAs quantum dot," *Physical Review B*, vol. 65, no. 7, pp. 073310, 2002.

[106] Y. Varshni, "Temperature dependence of the energy gap in semiconductors," *Physica*, vol. 34, no. 1, pp. 149-154, 1967.

[107] K. Odonnell, X. Chen, "Temperature dependence of semiconductor band gaps," *Applied Physics Letters*, vol. 58, no. 25, pp. 2924-2926, 1991.

[108] I. Vurgaftman, J. Meyer, and L. Ram-Mohan, "Band parameters for III–V compound semiconductors and their alloys," *Journal of Applied Physics*, vol. 89, no. 11, pp. 5815-5875, 2001.

[109] Y. Huang, H. Qiang, F. H. Pollak, G. Pettit, P. Kirchner, J. Woodall, H. Stragier, and L. B. Sorensen, "Temperature dependence of the photoreflectance of a strained layer (001) InGaAs/GaAs single quantum well," *Journal of Applied Physics*, vol. 70, pp. 7537, 1991.

[110] W. Ouerghui, A. Melliti, M. Maaref, and J. Bloch, "Dependence on temperature of homogeneous broadening of InGaAs/InAs/GaAs quantum dot fundamental transitions," *Physica E: Low-dimensional Systems and Nanostructures*, vol. 28, no. 4, pp. 519-524, 2005.

[111] N. Cade, H. Gotoh, H. Kamada, H. Nakano, S. Anantathanasarn, and R. Nötzel, "Optical characteristics of single InAs⁄InGaAsP⁄InP (100) quantum dots emitting at 1.55 μm," *Applied Physics Letters*, vol. 89, pp. 181113, 2006.

[112] E. Selcuk, A. Y. Silov, and R. Notzel, "Single InAs quantum dot arrays and directed self-organization on patterned GaAs (311) B substrates," *Applied Physics Letters*, vol. 94, no. 26, pp. 263108-263108-3, 2009.

[113] T. Tran, A. Muller, C. Shih, P. Wong, G. Balakrishnan, N. Nuntawong, J. Tatebayashi, and D. Huffaker, "Single dot spectroscopy of site-controlled InAs quantum dots nucleated on GaAs nanopyramids," *Applied Physics Letters*, vol. 91, no. 13, pp. 133104-133104-3, 2007.

[114] D. Gammon, E. Snow, B. Shanabrook, D. Katzer, and D. Park, "Fine structure splitting in the optical spectra of single GaAs quantum dots," *Physical Review Letters*, vol. 76, no. 16, pp. 3005-3008, 1996.

[115] R. Seguin, A. Schliwa, S. Rodt, K. Pötschke, U. Pohl, and D. Bimberg, "Size-dependent fine-structure splitting in self-organized InAs/GaAs quantum dots," *Physical Review Letters*, vol. 95, no. 25, pp. 257402, 2005.

[116] A. Huggenberger, S. Heckelmann, C. Schneider, S. Hofling, S. Reitzenstein, L. Worschech, M. Kamp, and A. Forchel, "Narrow spectral linewidth from single site-controlled In (Ga) As quantum dots with high uniformity," *Applied Physics Letters*, vol. 98, no. 13, pp. 131104-131104-3, 2011.

[117] R. Young, R. Stevenson, A. Shields, P. Atkinson, K. Cooper, D. Ritchie, K. Groom, A. Tartakovskii, and M. Skolnick, "Inversion of exciton level splitting in quantum dots," *Physical Review B*, vol. 72, no. 11, pp. 113305, 2005.

[118] B. Gerardot, S. Seidl, P. Dalgarno, R. J. Warburton, D. Granados, J. M. García, K. Kowalik, O. Krebs, K. Karrai, and A. Badolato, "Manipulating exciton fine structure in quantum dots with a lateral electric field," *Applied Physics Letters*, vol. 90, no. 4, pp. 041101-041101-3, 2007.

[119] S. Seidl, B. Gerardot, P. Dalgarno, K. Kowalik, A. Holleitner, P. Petroff, K. Karrai, and R. Warburton, "Statistics of quantum dot exciton fine structure splittings and their polarization orientations," *Physica E: Low-dimensional Systems and Nanostructures*, vol. 40, no. 6, pp. 2153-2155, 2008.

[120] G. Bester, S. Nair, and A. Zunger, "Pseudopotential calculation of the excitonic fine structure of million-atom self-assembled In1-xGaxAs/GaAs quantum dots," *Physical Review B*, vol. 67, no. 16, pp. 161306, 2003.

[121] W. Langbein, P. Borri, U. Woggon, V. Stavarache, D. Reuter, and A. Wieck, "Control of fine-structure splitting and biexciton binding in InxGa1-xAs quantum dots by annealing," *Physical Review B*, vol. 69, no. 16, pp. 161301, 2004.

[122] D. Ellis, R. Stevenson, R. Young, A. Shields, P. Atkinson, and D. Ritchie, "Control of fine-structure splitting of individual InAs quantum dots by rapid thermal annealing," *Applied Physics Letters*, vol. 90, no. 1, pp. 011907-011907-3, 2007.

[123] R. Stevenson, R. Young, P. See, D. Gevaux, K. Cooper, P. Atkinson, I. Farrer, D. Ritchie, and A. Shields, "Magnetic-field-induced reduction of the exciton polarization splitting in InAs quantum dots," *Physical Review B*, vol. 73, no. 3, pp. 033306, 2006.

[124] S. Reitzenstein, A. Forchel, "Quantum dot micropillars," *Journal of Physics D: Applied Physics*, vol. 43, no. 3, pp. 033001, 2010.

[125] E. M. Purcell, "Spontaneous Emission Probabilities at Radio Frequencies," *Physical Review*, vol. 69, pp. 681, 1946.

[126] J. Reithmaier, G. Sek, A. Loffler, C. Hofmann, S. Kuhn, S. Reitzenstein, L. Keldysh, V. Kulakovskii, T. Reinecke, and A. Forchel, "Strong coupling in a single quantum dot-semiconductor microcavity system," *Nature*, vol. 432, no. 7014, pp. 197-200, 2004.

[127] A. Kiraz, P. Michler, C. Becher, B. Gayral, A. Imamoglu, L. Zhang, E. Hu, W. Schoenfeld, and P. Petroff, "Cavity-quantum electrodynamics using a single InAs quantum dot in a microdisk structure," *Applied Physics Letters*, vol. 78, no. 25, pp. 3932-3934, 2001.

[128] C. E. Valdivia, E. Desfonds, D. Masson, S. Fafard, A. Carlson, J. Cook, T. J. Hall, and K. Hinzer, "Optimization of antireflection coating design for multijunction solar cells and concentrator systems," *Proc.SPIE7099*, vol. 709915, pp. 709915-709910, 2008.

[129] A. Luque, S. Hegedus, *Handbook of Photovoltaic Science and Engineering (2nd Edition)*, John Wiley & Sons, 2011.

[130] R. King, D. Law, K. Edmondson, C. Fetzer, G. Kinsey, H. Yoon, R. Sherif, and N. Karam, "40% efficient metamorphic GaInP⁄GaInAs⁄Ge multijunction solar cells," *Applied Physics Letters*, vol. 90, pp. 183516, 2007.

[131] W. Guter, J. Schone, S. P. Philipps, M. Steiner, G. Siefer, A. Wekkeli, E. Welser, E. Oliva, A. W. Bett, and F. Dimroth, "Current-matched triple-junction solar cell reaching 41.1% conversion efficiency under concentrated sunlight," *Applied Physics Letters*, vol. 94, no. 22, pp. 223504-223504-3, 2009.

[132] R. R. King, D. C. Law, K. M. Edmondson, C. M. Fetzer, G. S. Kinsey, H. Yoon, D. D. Krut, J. H. Ermer, R. A. Sherif, and N. H. Karam, "Advances in high-efficiency III-V multijunction solar cells," *Advances in OptoElectronics*, vol. 2007, 2007.

[133] E. Hecht, *Optics, 4th edition*, Addison Wesley, 2002.

[134] D. J. Aiken, "High performance anti-reflection coatings for broadband multi-junction solar cells," *Solar Energy Materials and Solar Cells*, vol. 64, no. 4, pp. 393-404, 2000.

[135] M. F. Schubert, F. W. Mont, S. Chhajed, D. J. Poxson, J. K. Kim, and E. F. Schubert, "Design of multilayer antireflection coatings made from co-sputtered and low-refractive-index materials by genetic algorithm," *Optics express*, vol. 16, no. 8, pp. 5290-5298, 2008.

[136] J. Xi, M. F. Schubert, J. K. Kim, E. F. Schubert, M. Chen, S. Lin, W. Liu, and J. A. Smart, "Optical thin-film materials with low refractive index for broadband elimination of Fresnel reflection," *Nature Photonics*, vol. 1, no. 3, pp. 176-179, 2007.

[137] J. DeNatale, P. Hood, J. Flintoff, and A. Harker, "Fabrication and characterization of diamond moth-eye antireflective surfaces on Ge," *Journal of Applied Physics*, vol. 71, no. 3, pp. 1388-1393, 1992.

[138] P. Clapham, M. Hutley, "Reduction of lens reflexion by the “Moth-eye” principle," *Nature (London)*, vol. 244, pp. 281-282, 1973.

[139] Q. Chen, G. Hubbard, P. A. Shields, C. Liu, D. W. Allsopp, W. N. Wang, and S. Abbott, "Broadband moth-eye antireflection coatings fabricated by low-cost nanoimprinting," *Applied Physics Letters*, vol. 94, no. 26, pp. 263118-263118-3, 2009.

[140] N. Yamada, O. N. Kim, T. Tokimitsu, Y. Nakai, and H. Masuda, "Optimization of anti-reflection moth-eye structures for use in crystalline silicon solar cells," *Progress in Photovoltaics: Research and Applications*, vol. 19, no. 2, pp. 134-140, 2011.

[141] C. Sun, P. Jiang, and B. Jiang, "Broadband moth-eye antireflection coatings on silicon," *Applied Physics Letters*, vol. 92, no. 6, pp. 061112-061112-3, 2008.

[142] C. Sun, B. J. Ho, B. Jiang, and P. Jiang, "Biomimetic subwavelength antireflective gratings on GaAs," *Optics Letters*, vol. 33, no. 19, pp. 2224-2226, 2008.

[143] W. Min, A. P. Betancourt, P. Jiang, and B. Jiang, "Bioinspired broadband antireflection coatings on GaSb," *Applied Physics Letters*, vol. 92, no. 14, pp. 141109-141109-3, 2008.

[144] J. Chen, K. Sun, "Enhancement of the light conversion efficiency of silicon solar cells by using nanoimprint anti-reflection layer," *Solar Energy Materials and Solar Cells*, vol. 94, no. 3, pp. 629-633, 2010.

[145] N. Yamada, T. Ijiro, E. Okamoto, K. Hayashi, and H. Masuda, "Characterization of antireflection moth-eye film on crystalline silicon photovoltaic module," *Optics Express*, vol. 19, no. 102, pp. A118-A125, 2011.

[146] K. Han, J. Shin, W. Yoon, and H. Lee, "Enhanced performance of solar cells with anti-reflection layer fabricated by nano-imprint lithography," *Solar Energy Materials and Solar Cells*, vol. 95, no. 1, pp. 288-291, 2011.

[147] J. M. Kontio, J. Simonen, J. Tommila, and M. Pessa, "Arrays of metallic nanocones fabricated by UV-nanoimprint lithography," *Microelectronic Engineering*, vol. 87, no. 9, pp. 1711-1715, 2010.

[148] A. F. Oskooi, D. Roundy, M. Ibanescu, P. Bermel, J. Joannopoulos, and S. G. Johnson, "MEEP: A flexible free-software package for electromagnetic simulations by the FDTD method," *Computer Physics Communications*, vol. 181, no. 3, pp. 687-702, 2010.

[149] S. Zollner, "Optical constants and critical-point parameters of GaAs from 0.73 to 6.60 eV," *Journal of Applied Physics*, vol. 90, no. 1, pp. 515-517, 2001.

[150] J. Tommila, V. Polojärvi, A. Tukiainen, J. Salmi, J. Puustinen, A. Aho, S. Ranta, T. Niemi, and M. Guina, "Moth-Eye Antireflection Coatings Fabricated by Nanoimprint Lithography on Dilute Nitride Solar Cell," *in 26th European Photovoltaic Solar Energy Conference and Exhibition*, pp. 367-369, 2011.

P1

Publication 1

J. Tommila, A. Tukiainen, J. Viheriälä, A. Schramm, T. Hakkarainen, A. Aho, P. Stenberg, M. Dumitrescu and M. Guina, "Nanoimprint lithography patterned GaAs templates for site-controlled InAs quantum dots," *Journal of Crystal Growth*, vol. 323, no. 1, pp. 183-186, 2011.

Nanoimprint lithography patterned GaAs templates for site-controlled InAs quantum dots

J. Tommila[a], A. Tukiainen[a], J. Viheriälä[a], A. Schramm[a], T. Hakkarainen[a], A. Aho[a], P. Stenberg[b], M. Dumitrescu[a] and M. Guina[a]

[a]*Optoelectronics Research Centre, Tampere University of Technology, FIN-33101 Tampere, Finland*

[b]*University of Eastern Finland, Department of Physics and Mathematics, FI-80101 Joensuu, Finland*

Abstract

We report on the development of a soft UV-nanoimprint lithography (UV-NIL) based process to fabricate nanopatterned templates for epitaxy of site-controlled Stranski-Krastanov grown quantum dots. Surface cleaning and chemical native oxide removal processes are analyzed in detail. The quality of the surface is studied by means of scanning electron microscopy, atomic force microscopy and photoluminescence analysis. To evaluate the suitability of the process for fabricating high optical quality site-controlled quantum dots, we have investigated the photoluminescence signal of the near-surface quantum well and overgrown quantum dots. We present the successful growth of optically active, site-controlled InAs quantum dots, both in the ensemble and single-dot regime, by molecular beam epitaxy on UV-NIL patterned GaAs surfaces using only chemical cleaning prior the growth.

Keywords

A1. Nanostructures, A1. Low dimensional structures, A1. Surface structure, A1. Surface processes, A3. Molecular beam epitaxy, B2. Semiconducting III-V materials.

1. Introduction

Semiconductor quantum dots (QDs) are expected to be the building blocks for future information technology platforms. In order to exploit the opportunities offered by the QD technology in advanced devices, such as single-photon emitters, it is essential to control the lateral position of the individual QD by defining the nucleation sites [1]. Nanoimprint lithography (NIL) [2] and especially its modification soft UV-NIL, which utilizes soft stamps and UV-curable polymers, is an attractive nanopatterning method for QD templates [3] because it is a low-cost, high resolution technique and offers high design freedom. Nanopatterns with 2 nm features [4] and high throughput [5,6] have been demonstrated earlier by NIL. Polymers used in UV-NIL differ in their chemical composition from those typically used in traditional nanopatterning methods (electron beam lithography, interference lithography). This causes specific concerns for achieving epi-ready surfaces, *i.e.* polymers are insoluble to solvents. Some NIL polymers contain inorganic additives that additionally complicate *ex situ* surface cleaning of the process residuals.

In this paper, we report on the development of UV-NIL process for patterning GaAs substrates, which are used as templates in seeded Stranski-Krastanov growth of QDs. The all important surface treatments before molecular beam epitaxy (MBE) overgrowth of QDs are discussed. In order to prove the suitability of UV-NIL patterned templates for epitaxy, we have grown optically active single and ensemble InAs QDs by MBE on the processed GaAs surface.

2. Sample preparation and experiments

The patterning was performed on n-type GaAs(100) wafers, which had an undoped MBE grown structure on top. It consisted of a GaAs buffer layer, an AlGaAs layer acting as a barrier for the photo-generated carriers and a GaAs layer. The pattering was made by utilizing soft UV-NIL process, which is described in detail in Ref. [7]. Two silicon master templates were used. The first one consisted of circular holes in a square array with period of 180 nm and diameter of 90 nm (fabricated by AMO GmbH). The second one (fabricated at University of Eastern Finland) consisted of circular holes in a square array with periods of 0.5 µm, 1 µm, 1.5 µm and 2 µm and diameters of 100 nm and 150 nm. The patterned areas were 1 x 1 mm^2. The patterning was done with an EVG 620 mask aligner (EV Group) on mr-UVCur06 (Micro Resist Technology GmbH) UV-NIL resist, which was spin coated on GaAs surface using TI-prime (MicroChemicals GmbH) as an adhesion promoter. Oxygen plasma and reactive ion etching (RIE, Oxford Instruments Plc) were used for residual etching to expose GaAs surface from the hole areas. GaAs etching was based on BCl_3/Ar chemistry and inductively coupled plasma reactive ion etching (ICP-RIE). A smooth, low-damage GaAs etching recipe was developed based on Refs. [8-10]. After GaAs etching, the residual mr-UVCur06 resist was removed by oxygen plasma (ICP-RIE). After the process, the final cleaning and native oxide removal was made by chemical treatments including isopropyl alcohol (IPA) rinse before and after the chemical etch consisting of solutions of HCl, IPA and NH_4OH. Prior to the overgrowth, the patterned samples were thermally annealed in the MBE chamber at 590 °C for 5 min. A 30 nm GaAs buffer was grown on top of the patterned structure at 470 °C. InAs QDs were grown on the high density pattern (180 nm period) at 540 °C, with an InAs coverage and growth rate of 1.8 monolayers (ML) and 0.05 ML/s,

respectively. Growth-interrupted MBE [11] was utilized in case of the pattern with longer periods. Here, 1.8 ML InAs was deposited in 8 periods, each consisting of 4 s growth and 2 s growth interruption, at a growth temperature of 540 °C with open arsenic valve. For photoluminescence (PL) studies, the QDs were capped by 20 nm and 50 nm GaAs grown at 540 °C and at 590 °C, respectively, and 50 nm AlGaAs grown at 590 °C. Room temperature PL (RT-PL) was measured by an Accent RPM2000 PL mapping tool using an excitation wavelength of 532 nm. Low temperature PL (LT-PL) on QD ensembles was measured at 20 K with a setup consisting of an Ar-ion excitation laser (λ = 480 nm), a monochromator and an InGaAs detector. µ-PL measurements were performed at 10 K using continuous-wave Ti:sapphire laser (λ = 700 nm) for excitation and a microscope objective for laser beam focusing (2 µm spot size). The PL signal was collected through the same objective and analyzed with a 46 cm long monochromator and N_2-cooled Si CCD detector. The spectral resolution of the setup was 80 µeV.

The surface cleaning steps were analyzed in detail in order to achieve high quality GaAs surface suitable for MBE regrowth. We measured PL of a near-surface quantum well (QW) in order to evaluate the impacts of the oxygen plasma cleaning step after GaAs etching [12,13]. The samples were prepared by growing an InGaAs QW structure emitting at 990 nm on n-type GaAs(100) substrates. The QW was separated from the surface by 50 nm GaAs layer. The GaAs surface was exposed to oxygen plasma in ICP-RIE with various etching conditions. Subsequently, a chemical native oxide removal was performed. Finally, the PL was measured by the Accent RPM2000 PL mapper.

The chemical cleaning and native oxide removal was studied by measuring PL from self-assembled InAs QDs closely located to the processed surface. First, an above mentioned GaAs, AlGaAs, GaAs structure was grown by MBE. Then the samples were immersed in IPA, HCl or NH_4OH containing solutions. Subsequently, the samples were loaded into the MBE chamber and annealed at 590 °C for 5 min. A GaAs buffer layer of 5 nm was grown on the processed surface. InAs QDs were grown at 505 °C with a coverage and growth rate of 2.1 ML and 0.05 ML/s, respectively. Subsequently, the QDs were capped by GaAs and AlGaAs. The PL signals of the InAs QDs were measured by the Accent RPM2000 PL mapper.

3. Results and discussion

The PL peak intensities of the near-surface QWs were measured at 990 nm both before plasma etching and after ICP-RIE etching and chemical oxide removal. The plasma environment and ion bombardment create surface states, which enhance the surface recombinations and thus, decrease the PL from the near-surface QW. Figure 1 shows the ratios of the PL peak intensities by varying the pressure (Fig. 1(a)), the RIE power (Fig. 1(b)), and the etch duration (Fig. 1(c)). The bias voltage between plasma and the sample is shown on the right side y-scale for each of the samples. Constant parameters for the etching process were: oxygen flow of 20 sccm, ICP source power of 300 W and table temperature of 25 °C. The chamber pressure was 120 mTorr, the RIE chuck power was 40 W, and the etch duration was 5 min unless otherwise stated. The bias voltage decreases with increasing pressure, and the ions bombarding the surface have less energy. Thus, the ions induce more damage to the surface with low operating pressures than with higher ones, which leads to the observed decrease in the PL intensity with decreasing

pressure. The same effect is mainly responsible for the decrease in PL intensity with increasing power. Here, the variations in the bias voltage are larger, which also leads to higher variations in the PL intensity. Furthermore, prolonged etch durations increase the PL intensity (Fig. 1(c)), which can be caused by passivation, removal of surface impurities, and saturation of the surface oxide formation as the etching proceeds. In addition to the PL properties, the capability of removing the resist completely has to be taken into account when choosing the etch parameters. Raising the pressure above 120 mTorr or lowering the RIE chuck power below 40 W left some residuals of the resist on the surface according to atomic force microscope (AFM) measurements.

Figure 2 shows the measured PL intensities of the InAs QDs grown on chemically treated surfaces. The deteriorated surface induces dislocations and other defects to the regrown GaAs, which degrade the optical quality of the overgrown QDs. Especially, the non-uniform and thick native oxide layer on GaAs causes pits and severe surface roughening after the annealing in the MBE chamber [14-16]. The chemical etching removes the native oxides and therefore an increase in PL intensity can be attributed to better surface quality and oxide removal prior to MBE overgrowth. 3 M solution of HCl in isopropyl alcohol (HCl:IPA) is shown to increase the PL intensity by a factor of four as compared to regular HCl etch. HCl:IPA was reported to leave arsenic rich GaAs surface [17,18]. Combining HCl:IPA treatment with dilute $NH_4OH:H_2O$ (1:5) yields even higher PL signal. The sample was rinsed with water between the chemicals. The highest PL signal was achieved by repeating HCl:IPA, $NH_4OH:H_2O$, HCl:IPA treatment cycle three times.

Figure 3 shows SEM and AFM images as well as a cross section of the UV-NIL fabricated template for short-period, site-controlled QD growth before epitaxy. Well-shaped, defect-free holes with diameter and depth of 90 nm and 20 nm, respectively, were observed. The root mean square surface roughness measured on separate samples by AFM for BCl_3/Ar and O_2 etched surfaces were 0.20 nm and 0.18 nm, respectively.

Figure 4(a) shows site-controlled InAs QDs with 180 nm period. Several holes were occupied by two or three QDs instead of a single QD. These multiple QDs were slightly smaller than the single QDs. PL spectra of buried QDs in nanoholes and QDs outside the pattern on the planar surface are shown in Fig. 4(b). The PL intensity from the QDs on nanopatterned region is comparable to the PL from unpatterned region, which indicates that the BCl_3/Ar based GaAs etching produces only minor damage to the crystal. The QD density on planar surface was intended to match the density of the holes in patterned area. However, the QD density on the unpatterned surface ($1 \cdot 10^{10}$ dots/cm^{-2}) was slightly higher than on the patterned surface ($7 \cdot 10^{9}$ dots/cm^{-2}), which explains part of the PL intensity difference between the patterned and unpatterned surfaces in Fig. 4(b). The PL spectra clearly show recombination from the ground state and the first exited state. The wavelengths of the ground state and first excited state recombination determined by Gaussian fits for RT-PL spectra were 1091 nm and 1039 nm, and 1119 nm and 1065 nm, for the nanopatterned and unpatterned surfaces, respectively. The ground state linewidths (FWHM) at RT for the nanopatterned and unpatterned surfaces were 52.5 nm and 54.0 nm, respectively. The multiple QDs might be the main reason for the wavelength difference of about 30 nm between nanopatterned and unpatterned surface [3,19,20]. The longer migration length of indium atoms on planar surface might provide the formation

of larger QDs on unpatterned surface as compared to the nanopatterned surface. Also the capping process, which was not optimized and performed at relatively high temperature, could affect differently on the QDs on patterned and unpatterned surfaces. Detailed investigation of these effects is the object of further research. The shell character of the QD PL spectra was confirmed by power dependent LT-PL measurements at 20 K from the nanopatterned surface shown in Fig. 4(c). The integrated intensities for Gaussian fitted peaks for ground state (GS), first excited state (E1) and second excited state (E2) are shown in the inset. The ground state shows saturation at the highest excitation powers.

Figure 5(a) shows single site-controlled InAs QDs that are separated by 1.5 μm. These low density QDs are fabricated by growth-interrupted MBE growth, which extends the migration time and length of indium atoms on the surface and makes the growth more selective to the shallow holes on the surface. Furthermore, desorption of indium from the surface is more pronounced during growth-interrupted MBE leading to the reduced QD density. With both types of patterns (short period in Fig. 4(a) and long period in Fig. 5(a)), practically no QDs were located between the holes, indicating a strong localization of the QDs on the holes. Figure 5(b) shows ensemble LT-PL measurements of the site-controlled QDs with 1.5 μm period and QDs outside the pattern on the planar surface. The unpatterned reference sample exhibits a strong wetting layer (WL) peak and very weak QD PL, which indicates that the QD density is extremely low on the planar surface. The nanopatterned sample shows an enhanced QD PL emission at 918 nm, shorter than the unpatterned reference sample, emitting at 938 nm. This is similar behavior to the short period QDs (Fig. 4). The short PL wavelength is attributed to the QD capping at

540 °C that reduces the QD height during the GaAs overgrowth. The inset in Fig. 5(b) shows power-dependent μ-PL spectra of a single QD on the 1.5 μm period pattern indicating single exciton recombination (X). The mean linewidth for the single QD PL calculated from Lorentzian fits for 16 different locations was 100 μeV, which was very close to the resolution limit of the system.

4. Conclusions

Detailed preparation steps of UV-NIL based patterning processes for seeded Stranski-Krastanov growth of QDs have been presented. Issues related to surface cleaning and native oxide removal were discussed. Successful growth of optically active, site-controlled InAs quantum dots, both in the ensemble and single-dot regime, was demonstrated using only chemical cleaning prior the growth. Future work will focus on tuning the optical properties of the individual QD on the nanopattern and embedding a single QD inside a microcavity.

Acknowledgments

The authors would like to thank Prof. Eli Kapon, Dr. Pascal Gallo and Romain Carron from École polytechnique fédérale de Lausanne for the help in μ-PL measurements and Mr. Ville Polojärvi for his help with LT-PL measurements. The work was supported by the Finnish Academy projects NANOTOMO (#118066) and DAUNTLESS (#123951). J. Tommila acknowledges the National Graduate School in Nanoscience (NGS-NANO) and the Pirkanmaa Regional Fund of the Finnish Cultural Foundation for the financial support. T. Hakkarainen acknowledges the National Graduate School in Materials Physics (NGSMP).

References

[1] T. Ishikawa, S. Kohmoto, K. Asakawa, Appl. Phys. Lett. 73 (1998) 1712-1714.

[2] S. Y. Chou, P. R. Krauss, P. J. Renstrom, Appl. Phys. Lett. 67 (1995) 3114-3116.

[3] Chien-Chia Cheng, K. Meneou, K. Y. Cheng, Appl. Phys. Lett. 95 (2009) 173108-1-173108-3

[4] F. Hua, Y. Sun, A. Gaur, M. A. Meitl, L. Bilhaut, L. Rotkina, J. Wang, P. Geil, M. Shim, J. A. Rogers, A. Shim, Nano Lett. 4 (2004) 2467-2471.

[5] J.-H. Chang, F.-S. Cheng, C.-C. Chao, Yu.-C. Weng, S.-Y. Yang, L. A. Wang, J. Vac. Sci. Technol. A 23 (2005) 1687-1690.

[6] T. Ohta, M. Hennesey, D. Strand, D. Jablonsky, B. Walton, B. Clark, IEEE Trans. Magn. 43 (2007) 836-839.

[7] J. Viheriälä, J. Tommila, T. Leinonen, M. Dumitrescu, L. Toikkanen, T. Niemi, M. Pessa, Microelectron. Eng. 86 (2009) 321-324.

[8] T. Maeda, J.W. Lee, R.J. Shul, J. Han, J. Hong, E.S. Lambers, S.J. Pearton, C.R. Abernathy, W.S. Hobson, Appl. Surf. Sci. 143 (1999) 174-182.

[9] F. N. Timofeev, S. A. Gurevich, V. B. Smirnitskii, L. B. Gladyshevax, B. S. Yavich and A. Usikov, Semicond. Sci. Technol. 11 (1996) 797-800.

[10] J.W. Lee, W.T. Lim, I.K. Baek, S.R. Yoo, M.H. Jeon, G.S Cho, S.J. Pearton, J. Electron. Mater. 33 (2004) 358-363.

[11] A. Balzarotti, Nanotechnol. 19 (2008) 505701.

[12] L. G. Deng, M. Rahman, J. A. van den Berg, C. D. W. Wilkinson, Appl. Phys. Lett. 75 (1999) 211-213.

[13] B. S. Ooi, A. C. Bryce, C. D. W. Wilkinson, J. H. Marsh, Appl. Phys. Lett. 64 (1994) 598-600.

[14] Y. Asaoka, T. Kanebishi, N. Sano, T. Kaneko, J. Cryst. Growth 251 (2003) 40-45.

[15] G. W. Smith, A. J. Pidduck, C. R. Whitehouse, J. L. Glasper, A. M. Keir, C. Pickering, Appl. Phys. Lett. 59 (1991) 3282-3284.

[16] T. Van Buuren, M. K. Weilmeier, I. Athwal, K. M. Colbow, J. A. Mackenzie, T. Tiedje, P. C. Wong, K. A. R. Mitchell, Appl. Phys. Lett. 59 (1991) 464-466.

[17] O. E. Tereshchenko, S. I. Chikichev, A. S. Terekhov, Appl. Surf. Sci. 142 (1999) 75-80.

[18] O. E. Tereshchenko, A. S. Terekhov, D. Paget, P. Chiaradia, J. E. Bonnet, R. Belkhou, A. Taleb-Ibrahimi, Surf. Sci. 507-510 (2002) 411-416.

[19] M. Grundmann, N. N. Ledentsov, O. Stier, D. Bimberg, V. M. Ustinov, P. S. Kop'ev, Zh. I. Alferov, Appl. Phys. Lett. 68 (1996) 979-981.

[20] N. Tang, J. Mater. Sci. 42 (2007) 6913–6916.

Figures

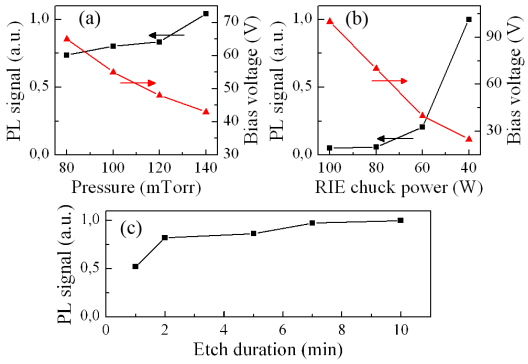

Fig. 1. PL peak intensities (squares) at 990 nm after the chemical treatment by varying the chamber pressure (a) (RIE chuck power 40 W and etch duration 5 min), RIE power (b) (pressure 120 mTorr and etch duration 5 min) and etch duration (c) (pressure 120 mTorr and RIE chuck power 40 W). The bias voltages (triangles) are shown on the right y-scale.

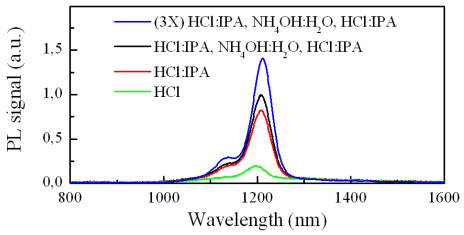

Fig. 2. PL spectra of InAs QDs grown on chemically treated surfaces.

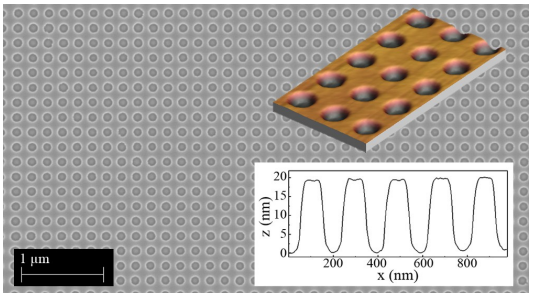

Fig. 3. SEM image of the UV-NIL fabricated template before epitaxy. Insets are showing an AFM micrograph and a cross section of the template.

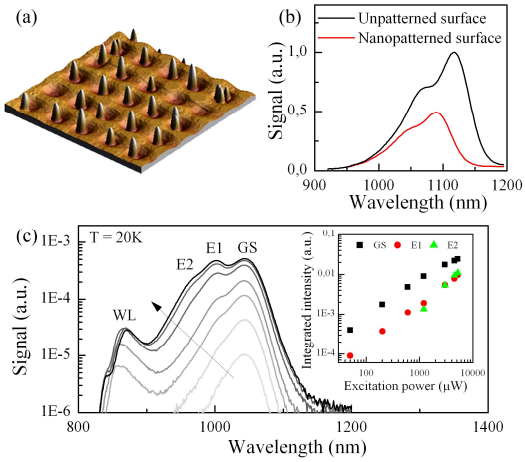

Fig. 4. (a) AFM micrograph of site-controlled InAs QDs on UV-NIL patterned surface. (b) PL spectra of the site-controlled QDs and QDs outside the pattern. (c) Power dependent (from 50 μW to 5.2 mW) low temperature PL spectra of the site-controlled QDs. The inset in (c) shows the integrated intensities of Gaussian fitted peaks as a function of excitation power.

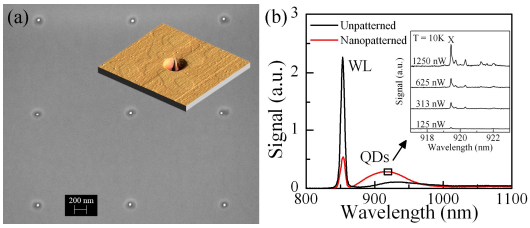

Fig. 5. (a) SEM image of the low density InAs QDs with 1.5 μm period. Inset shows an AFM micrograph of a single QD. (b) Low temperature PL spectra of the reference sample and the nanopatterned sample with 1.5 μm period. Inset shows power dependent μ-PL spectra of a single QD on the pattern.

Publication 2

P2

J. Tommila, A. Schramm, T. V. Hakkarainen, M. Dumitrescu, and M. Guina, ”Size-dependent properties of single InAs quantum dots grown in nanoimprint lithography patterned GaAs pits,” *Nanotechnology*, vol. 24, 235204 (5pp), 2013.

Nanotechnology **24** (2013) 235204 (5pp) doi:10.1088/0957-4484/24/23/235204

Size-dependent properties of single InAs quantum dots grown in nanoimprint lithography patterned GaAs pits

J Tommila, A Schramm, T V Hakkarainen, M Dumitrescu and M Guina

Optoelectronics Research Centre, Tampere University of Technology, PO Box 692, FIN-33101, Tampere, Finland

E-mail: juha.tommila@tut.fi

Received 17 January 2013, in final form 5 April 2013
Published 15 May 2013
Online at stacks.iop.org/Nano/24/235204

Abstract
We report on the structural and optical properties of single InAs quantum dots (QDs) formed in etched GaAs pits with different dimensions. The site-controlled QDs were fabricated by molecular beam epitaxy on GaAs(001) surfaces patterned by nanoimprint lithography. We show that the properties of the QDs can be modified by varying the dimensions of the etched GaAs pits. Increasing the pit size resulted in larger QDs and thus in longer photoluminescence wavelengths. However, the fine structure splitting remained unaffected. A photoluminescence linewidth of 41 μeV and average fine structure splitting of 15.7 μeV were obtained for exciton recombination in the single site-controlled QDs.

(Some figures may appear in colour only in the online journal)

1. Introduction

Owing to their tunable atomic-like optical and electrical properties, the utilization of single semiconductor quantum dots (QDs) for quantum information processing has been demonstrated within several concepts, such as quantum cryptography and quantum computing [1–3]. Precise control of the lateral position of single QDs, simultaneously with the control of their optical and electrical properties, is a prerequisite for applications based on QDs as single [4, 5] or entangled photon sources [6, 7]. Deterministic lateral positioning of InAs QDs on GaAs surfaces has been achieved by various lithography techniques and regrowth procedures [8–10], and triggered indistinguishable single photons from state-of-the-art site-controlled QDs (SCQDs) has been reported [11]. However, lithographically defined surface patterns not only determine the QD positions but also affect the QD properties, such as emission energy and linewidth of the exciton recombination. The QD size and, in particular, its height mainly define the emission energy of the excitonic transition in the dot. For InAs QDs, the energy is reported to range from 1.4 eV, for very shallow QDs, to 0.8 eV for large QDs [12]. A narrow emission linewidth is desired when coupling an emission state and an optical cavity mode [13]. Furthermore, the exciton fine structure splitting (FSS), which has to be minimized in order to produce pairs of entangled photons by biexciton–exciton cascade [7, 14], is affected by the fabrication process. The FSS is caused by the electron–hole exchange interaction and typically increases with increasing lateral asymmetry [15]. Typical linewidth and FSS values for SCQDs fabricated on GaAs(001) surfaces have been reported to vary in the range of 25–100 μeV [16–19], for linewidth, and 20–60 μeV [17, 18], for FSS. Postgrowth methods, including thermal annealing, and applying magnetic or electric field, have been used to control these properties [20–22]. However, these methods have a limited tuning range and often adversely affect several properties at once.

In this paper, we use soft UV-nanoimprint lithography (UV-NIL) combined with molecular beam epitaxy (MBE) to fabricate SCQDs. In particular, our study aims at investigating the structural and optical properties of single site-controlled InAs quantum dots formed in etched GaAs pits with different dimensions. The SCQDs were characterized by atomic force microscopy (AFM) and micrometre-scale photoluminescence (μPL) experiments. We show that the QD properties can be

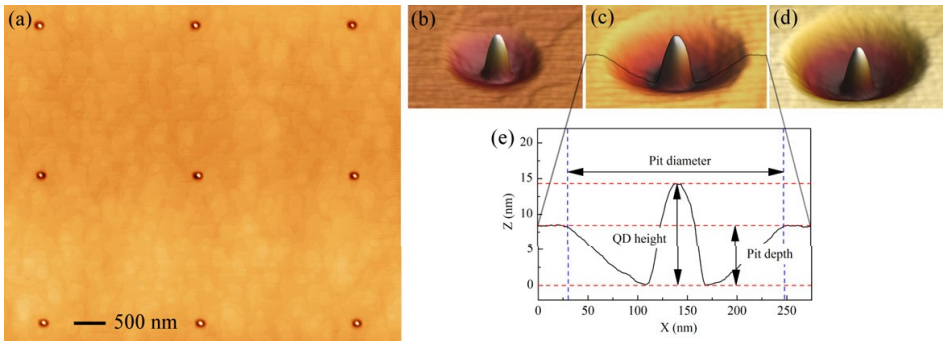

Figure 1. (a) AFM image of an array of surface SCQDs in pits with period of 2.5 μm and diameter of 100 nm after patterning. (b)–(d) 3D AFM images of SCQDs in pits with diameters of 165 nm, 220 nm and 250 nm, respectively. The heights of the QDs were 13.2 nm, 14.4 nm and 15.8 nm for (b), (c) and (d), respectively. (e) A cross section of the QD in the pit shown in (c), and definitions for QD height, pit depth and pit diameter.

influenced not only by the growth parameters, but also by the pattern, in our case by different sizes of the etched GaAs pits.

2. Experimental details

The site-controlled InAs quantum dots were fabricated on a patterned GaAs(001) wafer by MBE. First, we grew a distributed Bragg reflector consisting of 25 pairs of AlGaAs/GaAs layers. Second, soft UV-NIL was applied to pattern the GaAs surface. The patterned layer on the stamp consisted of antiadhesion coated OrmoStamp (Micro resist technology GmbH) and the patterning was performed using EVG 620 mask aligner (EV Group). UV-NIL resists (mr-UVCur06, Micro resist technology GmbH) was used as an etch mask. Two optimized dry etching processes based on BCl_3/Ar chemistry and BCl_3/Cl_2 chemistry were utilized to form pits for QD nucleation and alignment marks, respectively, in a single UV-NIL step. The pits were positioned in a square array with a period of 2.5 μm and had diameters of 80, 100 and 120 nm, and a depth of 15–20 nm. After the patterning, a chemical cleaning and native oxide removal were performed and the samples were loaded into the MBE chamber. The patterning and cleaning processes are described in more detail in [23]. Finally, a 30 nm GaAs buffer layer and 1.8 ML of InAs were grown at 470 °C and 540 °C, respectively. The InAs growth rate was 0.05 μm h^{-1}. For surface measurements, a template consisting of only one pair of AlGaAs/GaAs was used and the sample was unloaded from the MBE chamber after the QD growth. For μPL studies, the QDs were capped by 20 nm and 50 nm of GaAs grown at 540 °C and at 590 °C, respectively, and a subsequent 50 nm AlGaAs layer was grown at 590 °C. The structure was finalized by a 10 nm GaAs layer. The first part of the capping was performed at the same temperature as the QD growth and once the QDs were safely covered by GaAs, the temperature was increased to 590 °C.

AFM was used to study the surface samples. For μPL measurements, the sample consisting of capped SCQDs was loaded into a low vibration closed-cycle helium cryostat and cooled down to 5 K. Nonresonant optical excitation at 532 nm was used, and the laser beam was focused on the sample with a 50× high NA objective. The spot diameter on the sample was approximately 1 μm. For intensity images and sample alignment, a diverging lens was used to increase the diameter of the laser spot on the sample to 30 μm. The emitted signal was collected by the same objective and dispersed with a 0.75 m spectrometer equipped with a 1800 lines mm^{-1} grating and a cooled Si CCD camera. The spectral resolution of the system was 30 μeV. In polarization-resolved measurements, we used a linear polarizer and a rotating half wave plate in front of the entrance slit of the spectrometer.

3. Results and discussion

For a first overview, we present in figure 1(a) an AFM image of an array of surface SCQDs with period of 2.5 μm. Figures 1(b)–(d) show AFM images of surface SCQDs in pits with diameters of 165 nm, 220 nm and 250 nm, respectively. The corresponding heights of the SCQDs were 13.2, 14.4 and 15.8 nm. An exemplary line scan of the SCQD in figure 1(c) and the definitions of the QD height, pit depth and pit diameter are shown in figure 1(e). In order to study the influence of the pit size on the SCQD properties, we measured the dimensions of several pits and heights of single surface SCQDs by AFM after the growth of the GaAs buffer layer and InAs QDs. The depth and diameter of the pit as a function of the initial pit diameter after patterning are shown in figure 2(a). The dimensions were obtained from measurements of about ten pits corresponding to every initial diameter. We observed that the pit diameters roughly doubled during the overgrowth of the 30 nm GaAs layer. Furthermore, the depths of the pits were reduced more for small pits than for the larger ones. The standard deviations for pit depth and diameter after the buffer growth were 0.3–0.6 nm and 3.5–6.9 nm, respectively. Figures 2(b) and (c) show the QD height as a function of pit diameter and depth, respectively. The QD height was clearly dependent on the size of the pit and it increased with increasing pit depth and diameter. This was attributed

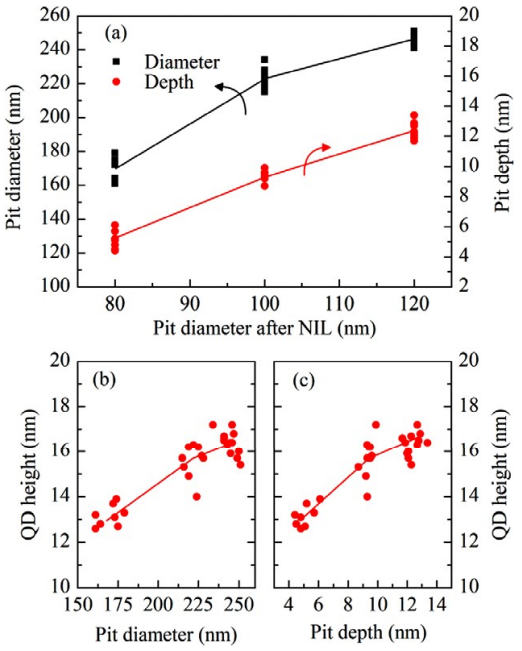

Figure 2. (a) The depth and diameter of the pits after GaAs buffer growth as a function of the initial pit diameter after patterning. QD height as a function of the pit diameter (b) and depth (c). Solid lines indicate the average values.

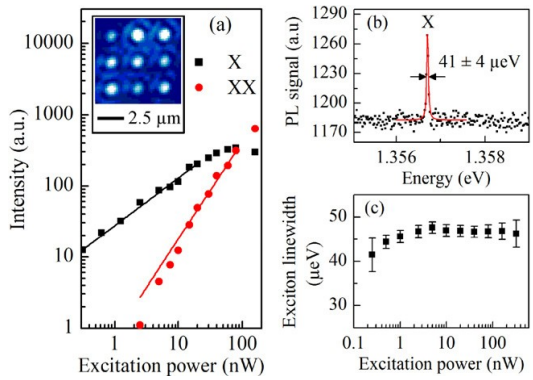

Figure 3. (a) Integrated intensities as a function of laser power for X and XX peaks for a single SCQD. Solid lines show the fitted power dependences for the peaks. The inset shows a PL intensity image of the capped SCQDs measured within the spectral range of 875–1000 nm. (b) The PL spectrum of the SCQD measured at 7 K and at 0.25 nW excitation power. The Lorentzian fit to the exciton peak shows a linewidth of 41 μeV. (c) The exciton linewidth as a function of the excitation power.

to an enhanced accumulation of indium into the bottom of the pit. Lower surface energy caused by the concave surface curvature assists indium migration towards the bottom of the pit [24]. Thus, the total amount of indium forming the QD was proportional to the size of the pit. The standard deviation for QD height was 0.5–0.9 nm. A precise measurement of the QD diameter was not possible from AFM scans, but the diameter is expected to increase with increasing QD height and the aspect ratio to remain constant. The estimated diameter of the QDs was 30–40 nm. Scanning electron microscope (SEM) images were used to calculate the single QD occupancy as a function of the pit size from the surface sample. The probability of having a single SCQD in a pit was 39%, 70% and 22% for 80 nm, 100 nm and 120 nm pits, respectively. The pits having diameters of 80 nm and not singly occupied were mainly empty, whereas the pits with diameters of 120 nm had mainly double QDs. This was consistent with the results presented for electron beam lithography patterned GaAs [16, 24]. Spontaneous formation of QDs in between the pits occurred only on defect sites and was in the order of one interstitial QD per 25 SCQDs.

In order to evaluate the influence of the pit size on the optical properties, the PL spectra of several embedded single SCQDs were measured by μPL experiments. First, intensity images were utilized for sample alignment. The inset in figure 3(a) shows a PL intensity image of capped SCQDs. The intensity was measured within the spectral range of 875–1000 nm using a high-pass filter in order to cut-off the emission from the wetting layer and the substrate. Second, we used power and polarization dependent measurements in order to identify the peaks related to excitonic (X) and biexcitonic (XX) recombinations. The integrated PL intensities as a function of the excitation power for the emission peaks of an exemplary single SCQD are shown in figure 3(a). The solid lines in the figure represent fitting the data to the relation $I \propto P^n$, where P is the excitation power. We obtained values for n of 0.7 and 1.4 for X and XX peaks, respectively. Similar deviations from theoretically estimated values, i.e. $I \propto P$ for X and $I \propto P^2$ for XX, have been previously reported [25, 26]. However, the fact that the intensities of the XX peaks are proportional to the square of the intensities of the X peaks, as well as the symmetric polarization dependences of the peak wavelengths confirm the identification of the peaks [15, 25, 27, 28]. The biexciton binding energy was 2.1 meV. Additionally, one relatively strong peak in the spectrum was related to a charged exciton (not shown), since the value for n was close to the one for the X peak, and the peak wavelength was polarization independent [29]. A PL spectrum of the same SCQD measured at 7 K and at 0.25 nW excitation power is shown in figure 3(b). The Lorentzian fit to the exciton peak shows a full width at half maximum (FWHM) value of 41 μeV, which is comparable to self-assembled QDs [30] and recent results of SCQDs [16–18]. Figure 3(c) shows the exciton linewidth as a function of the excitation power. The linewidth increased from 41 to 47 μeV with increasing laser power. The increase of the linewidth has been previously reported and attributed to spectral diffusion due to a charge carrier background [17, 31].

Figure 4 shows the energy and width of the PL peak related to the excitonic transition (X) as a function of the initial pit diameter. Solid lines indicate the average values for each pit diameter. The measurements were performed at 40 K in order to increase the intensity related to

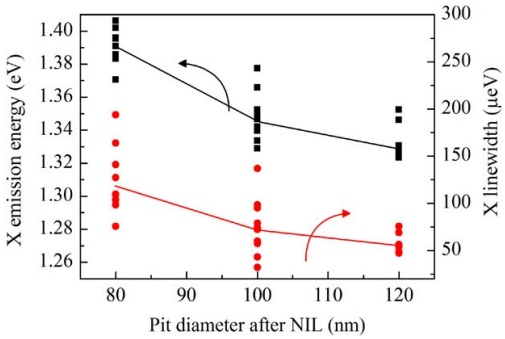

Figure 4. The energy and linewidth of the PL peak related to the exciton transition (X) as a function of the initial pit diameter. Solid lines indicate the average values for each pit diameter.

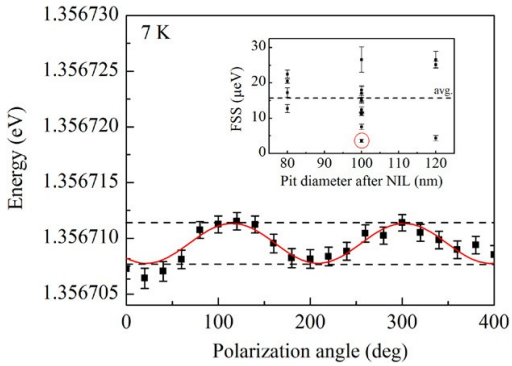

Figure 5. Peak energies of Lorentzian fits to exciton peaks at different polarization angles for a typical SCQD emitting at 914 nm. The excitation power was 10 nW. The solid line presents a sinusoidal fit, from which the FSS value is calculated and marked by a red circle in the inset. The inset shows FSS values for 17 exciton emission lines from single SCQDs as a function of pit diameter and the average value of 15.7 μeV. The error bars indicate the error in fitting to the data.

exciton recombinations [32]. The peaks were identified by excitation power and polarization dependent measurements as described earlier. We observed that the emission energy was decreasing with increasing pit diameter. This is explained by the increasing QD size with increasing pit dimensions, as expected from the surface QD measurements. It has to be noted that the QD height was strongly reduced during the high-temperature capping, which also caused In/Ga intermixing. However, the relative size distribution is expected to be preserved. Furthermore, the linewidths of the exciton peaks were reduced with increasing pit diameter. This is attributed to the spectral diffusion caused by charged defects in the QD environment. The distance between the defects and QDs is supposed to increase with increasing pit diameter, thus reducing the linewidth, in qualitative agreement with the calculations in [28] and the results presented for QDs in etched mesas [30]. The average values for the linewidths at 40 K were 123 μeV, 75 μeV and 57 μeV for 80 nm, 100 nm and 120 nm pits, respectively. These values are expected to decrease by about 25% if the temperature is lowered from 40 K, as shown in [32]. A minor part of the linewidth broadening is caused by the FSS discussed in the next paragraph [28].

Polarization dependent measurements performed at 5–7 K revealed a small FSS in the exciton related peaks. The peak energies of Lorentzian fits to exciton peaks at different linear polarization angles for a typical SCQD emitting at 914 nm are shown in figure 5. The PL spectrum and the power dependent measurements of the same dot are shown in figure 3. The FSS is calculated from the sinusoidal fit to the data. The XX peak showed polarization dependence with a 90° phase shift with respect to the X peak. The inset in figure 5 shows the corresponding FSS values for 17 exciton emission lines from single SCQDs as a function of the initial pit size. The values range from 27 μeV down to 4 μeV, which is very close to the resolution limit of this method [22]. The mean value was 15.7 μeV, which is among the lowest values for self-assembled QDs on a GaAs(001) surface [33–35]. The low FSS value suggests that the strain-induced piezoelectric effect and the elongation of the QDs are small, since these are the main sources of FSS [33]. Here, we have used very high capping temperature, which symmetrizes the lateral potential of the exciton [20] and reduces strain due to In/Ga intermixing [36]. However, even QDs with cylindrical in-plane symmetry are reported to have nonzero FSS due to reduced atomistic symmetry [37]. Interestingly, we did not observe any dependence of the FSS on the pit size or the emission energy. This is probably due to the fact that the FSS values are very small as compared to the typical 0–500 μeV range and at these emission energies, i.e. for small QDs, small FSS is expected [33, 38]. Additionally, the emission energy dependent FSS is mainly caused by piezoelectricity, which is weak for small QDs [33]. More detailed studies are required in order to thoroughly evaluate the origin of the FSS.

4. Conclusions

We have assessed the interplay between the diameters of pits used for patterned growth of QDs, and the properties of single QDs. In addition to single QD occupancy, this information is a key parameter when designing a device consisting of single SCQDs. The results indicate that by choosing a suitable pit size for this type of SCQD, the optical properties and single QD occupancy can be optimized and low values for the linewidth and FSS of the excitonic transition can be achieved.

Acknowledgments

The research was carried out within the Academy of Finland projects DAUNTLESS (decision number 123951), PhotonicQCA (263594) and ERA.NET project QuadSys (264971). JT acknowledges the National Doctoral Programme in Nanoscience (NGS-NANO), the Ulla Tuominen Foundation and Jenny and Antti Wihuri Foundation for the financial support. AS acknowledges funding from the Academy of

Finland within the project 138940. TVH acknowledges financial support from the Finnish National Graduate School in Materials Physics. The authors would like to thank Mr Wei Zhang, Soochow University, Suzhou, China, for his help in μPL measurements.

References

[1] Waks E, Inoue K, Santori C, Fattal D, Vuckovic J, Solomon G S and Yamamoto Y 2002 *Nature* **420** 762–2
[2] Santori C, Fattal D, Vuckovic J, Solomon G S and Yamamoto Y 2002 *Nature* **419** 594–7
[3] Knill E, Laflamme R and Milburn G J 2001 *Nature* **409** 46–52
[4] Michler P, Kiraz A, Becher C, Schoenfeld W, Petroff P, Zhang L, Hu E and Imamoglu A 2000 *Science* **290** 2282–5
[5] Schneider C, Heindel T, Huggenberger A, Niederstrasser T, Reitzenstein S, Forchel A, Hofling S and Kamp M 2012 *Appl. Phys. Lett.* **100** 091108
[6] Salter C, Stevenson R, Farrer I, Nicoll C, Ritchie D and Shields A 2010 *Nature* **465** 594–7
[7] Stevenson R M, Young R J, Atkinson P, Cooper K, Ritchie D A and Shields A J 2006 *Nature* **439** 179–82
[8] Martiín-Saínchez J, Muñoz-Matutano G, Herranz J, Canet-Ferrer J, Alén B, González Y, Alonso-González P, Fuster D, González L and Martiínez-Pastor J 2009 *ACS Nano* **3** 1513–7
[9] Felici M, Gallo P, Mohan A, Dwir B, Rudra A and Kapon E 2009 *Small* **5** 938–43
[10] Schneider C, Straub M, Sunner T, Huggenberger A, Wiener D, Reitzenstein S, Kamp M, Hofling S and Forchel A 2008 *Appl. Phys. Lett.* **92** 183101
[11] Jöns K, Atkinson P, Müller M, Heldmaier M, Ulrich S, Schmidt O and Michler P 2012 *Nano Lett.* **13** 126–30
[12] Tang N 2007 *J. Mater. Sci.* **42** 6913–6
[13] Hennessy K, Badolato A, Winger M, Gerace D, Atature M, Gulde S, Falt S, Hu E L and Imamoglu A 2007 *Nature* **445** 896–9
[14] Benson O, Santori C, Pelton M and Yamamoto Y 2000 *Phys. Rev. Lett.* **84** 2513–6
[15] Gammon D, Snow E S, Shanabrook B V, Katzer D S and Park D 1996 *Phys. Rev. Lett.* **76** 3005–8
[16] Schneider C, Huggenberger A, Gschrey M, Gold P, Rodt S, Forchel A, Reitzenstein S, Höfling S and Kamp M 2012 *Phys. Status Solidi* a **209** 2379–86
[17] Huggenberger A, Heckelmann S, Schneider C, Hofling S, Reitzenstein S, Worschech L, Kamp M and Forchel A 2011 *Appl. Phys. Lett.* **98** 131104
[18] Skiba-Szymanska J *et al* 2011 *Nanotechnology* **22** 065302
[19] Schramm A, Tommila J, Hakkarainen T V, Tukiainen A, Dumitrescu M, Mews A, Kipp T and Guina M 2012 *Nanotechnology* **23** 175701
[20] Langbein W, Borri P, Woggon U, Stavarache V, Reuter D and Wieck A D 2004 *Phys. Rev.* B **69** 161301
[21] Stevenson R M, Young R J, See P, Gevaux D G, Cooper K, Atkinson P, Farrer I, Ritchie D A and Shields A J 2006 *Phys. Rev.* B **73** 033306
[22] Gerardot B, Seidl S, Dalgarno P, Warburton R J, Granados D, García J M, Kowalik K, Krebs O, Karrai K and Badolato A 2007 *Appl. Phys. Lett.* **90** 041101
[23] Tommila J, Tukiainen A, Viheriälä J, Schramm A, Hakkarainen T, Aho A, Stenberg P, Dumitrescu M and Guina M 2011 *J. Cryst. Growth* **323** 183–6
[24] Atkinson P, Schmidt O G, Bremner S P and Ritchie D A 2008 *C.R. Phys.* **9** 788–803
[25] Alloing B, Zinoni C, Zwiller V, Li L, Monat C, Gobet M, Buchs G, Fiore A, Pelucchi E and Kapon E 2005 *Appl. Phys. Lett.* **86** 101908
[26] Kaiser S, Mensing T, Worschech L, Klopf F, Reithmaier J and Forchel A 2002 *Appl. Phys. Lett.* **81** 4898–900
[27] Ellis D, Stevenson R, Young R, Shields A, Atkinson P and Ritchie D 2007 *Appl. Phys. Lett.* **90** 011907
[28] Abbarchi M, Troiani F, Mastrandrea C, Goldoni G, Kuroda T, Mano T, Sakoda K, Koguchi N, Sanguinetti S and Vinattieri A 2008 *Appl. Phys. Lett.* **93** 162101
[29] Finley J J, Mowbray D J, Skolnick M S, Ashmore A D, Baker C, Monte A F G and Hopkinson M 2002 *Phys. Rev.* B **66** 153316
[30] Bayer M and Forchel A 2002 *Phys. Rev.* B **65** 041308
[31] Berthelot A, Favero I, Cassabois G, Voisin C, Delalande C, Roussignol P, Ferreira R and Gérard J M 2006 *Nature Phys.* **2** 759–64
[32] Tommila J, Strelow C, Schramm A, Hakkarainen T V, Dumitrescu M, Kipp T and Guina M 2012 *Nanoscale Res. Lett.* **7** 313
[33] Seguin R, Schliwa A, Rodt S, Pötschke K, Pohl U W and Bimberg D 2005 *Phys. Rev. Lett.* **95** 257402
[34] Treu J, Schneider C, Huggenberger A, Braun T, Reitzenstein S, Hofling S and Kamp M 2012 *Appl. Phys. Lett.* **101** 022102
[35] Seidl S, Gerardot B D, Dalgarno P A, Kowalik K, Holleitner A W, Petroff P M, Karrai K and Warburton R J 2008 *Physica* E **40** 2153–5
[36] Tartakovskii A I *et al* 2004 *Phys. Rev.* B **70** 193303
[37] Bester G, Nair S and Zunger A 2003 *Phys. Rev.* B **67** 161306
[38] Young R J, Stevenson R M, Shields A J, Atkinson P, Cooper K, Ritchie D A, Groom K M, Tartakovskii A I and Skolnick M S 2005 *Phys. Rev.* B **72** 113305

Publication 3

P3

J. Tommila, C. Strelow, A. Schramm, T. V. Hakkarainen, M. Dumitrescu, T. Kipp and M. Guina, “The influence of temperature on the photoluminescence properties of single InAs quantum dots grown on patterned GaAs,” *Nanoscale Research Letters*, vol. 7, no. 313, pp. 1-4, 2012.

Nanoscale Research Letters
a SpringerOpen Journal

NANO EXPRESS Open Access

The influence of temperature on the photoluminescence properties of single InAs quantum dots grown on patterned GaAs

Juha Tommila[1*], Christian Strelow[2], Andreas Schramm[1], Teemu V Hakkarainen[1], Mihail Dumitrescu[1], Tobias Kipp[2] and Mircea Guina[1]

Abstract: We report the temperature-dependent photoluminescence of single site-controlled and self-assembled InAs quantum dots. We have used nanoimprint lithography for patterning GaAs(100) templates and molecular beam epitaxy for quantum dot deposition. We show that the influence of the temperature on the photoluminescence properties is similar for quantum dots on etched nanopatterns and randomly positioned quantum dots on planar surfaces. The photoluminescence properties indicate that the prepatterning does not degrade the radiative recombination rate for the site-controlled quantum dots.

Keywords: III-V semiconductors, InAs, Quantum dots, Site-controlled quantum dots, Molecular beam epitaxy, Nanoimprint lithography

PACS: 78, optical properties, condensed-matter spectroscopy and other interactions of radiation and particles with condensed matter, 78.67.-n, optical properties of low-dimensional, mesoscopic, and nanoscale materials and structures, 78.67.Hc, quantum dots

Background

Single semiconductor quantum dots (QDs) are the building blocks for future information processing platforms, such as quantum cryptography and quantum computing [1-3]. QDs have been exploited as single [4,5] and entangled photon sources [6,7]. In order to enable such applications, the QDs should be fabricated at well-defined positions, rendering impractical the standard epitaxial processes that would result in randomly positioned QDs. The control of QD position can be achieved by creating preferential nucleation sites via patterning the deposited surface. Site-controlled quantum dots (SCQDs) have been fabricated utilizing various patterning techniques [8-12] combined with molecular beam epitaxy (MBE) or metalorganic vapor phase epitaxy. The optical properties of single QDs are easily deteriorated by defects, which are induced during the patterning and subsequent overgrowth. The defects cause nonradiative recombination channels, which degrade the QD photoluminescence (PL). Measuring the optical properties of a QD as a function of temperature provides a method to assess the quality of the QDs.

In this paper, we study the temperature-dependent PL of single SCQDs fabricated on a nanoimprint lithography patterned GaAs(100) surface. We compare their PL properties to the ones of single self-assembled quantum dots (SAQDs) grown on unpatterned surface.

Methods

The InAs QD sample was fabricated on a GaAs(100) substrate by combination of MBE and soft ultraviolet nanoimprint lithography (UV-NIL). First, a GaAs buffer layer, an AlGaAs barrier layer and a GaAs layer were grown by MBE. Second, the sample was patterned *ex situ* by UV-NIL using mr-UVCur06 (Micro Resist Technology GmbH, Berlin, Germany) as an etch mask and an EVG-620 (EV Group, St. Florian am Inn, Austria) mask aligner. The patterned area consisted of holes with a diameter of 100 nm arranged in a square lattice with the period of 1.5 μm. After patterning, the sample was chemically cleaned, and the native oxides were removed using IPA-, HCl-, and NH_4OH-based solutions. The process is described in more detail in [13]. After chemical treatment, the sample was

* Correspondence: juha.tommila@tut.fi
[1]Optoelectronics Research Centre, Tampere University of Technology, Korkeakoulunkatu 3, Tampere, FIN-33720, Finland
Full list of author information is available at the end of the article

loaded into the MBE reactor, and a 30-nm GaAs buffer layer was grown at 470°C. Growth-interrupted MBE [13,14] at 540°C was used to form single SCQDs in the patterned holes and low density SAQDs randomly positioned outside the patterned area. Finally, the QDs were capped by 20 and 50 nm of GaAs grown at 540°C and at 590°C, respectively, and 50-nm AlGaAs grown at 590°C. The structure was finished by a 10-nm GaAs layer.

Micro-PL (μPL) measurements were performed at various temperatures up to 70 K using a continuous-wave laser emitting at 532 nm for excitation and a microscope objective (numerical aperture = 0.8) for diffraction-limited laser beam focusing and PL light collection. The PL signal was dispersed by a 50-cm spectrometer containing a 1,200 lines/mm grating and detected by a cooled Si CCD camera. The spectral resolution of the setup was 66 μeV.

Results and discussion

In order to evaluate the large scale optical quality of the sample, we added a diverging lens into the beam of the excitation laser in the μPL setup. The widened illumination field had a diameter of about 30 μm on the sample. Figure 1 shows PL intensity images from the edge of the patterned area within the spectral range of 850 to 1,000 nm at temperatures of 5, 40, and 70 K. Regularly spaced (1.5-μm period) bright spots illustrate PL emission from single SCQDs. Spots outside the array originate from SAQDs. For the lowest temperature (Figure 1a), the whole PL image is affected by a relatively strong background. Spectrally resolved measurements confirm its origin in the wetting layer (WL) emission, which is typical for low density QDs [15]. At low temperatures, the photoexcited carriers are trapped and recombined in the WL at localizing potentials induced by irregularities in WL [16]. The effect was confirmed by the fine structure of the WL PL (not shown). At 40 K (measurement shown in Figure 1b), the emission from WL is reduced because of the thermal escape of the carriers from the localizing potentials and a very thin WL typical for this growth technique [17]. An array of intense PL spots from the single SCQDs with 1.5-μm period is observed. When the sample was heated up to 70 K (measurement shown in Figure 1c), the PL emission from some individual QDs decreased due to thermal escape of carriers from the QD states and decreased carrier population in the WL acting as a carrier reservoir for QDs [16]. In spite of the slight deviations in uniformity, most of the SCQDs exhibit bright luminescence even at relatively high temperatures, indicating a low amount of nonradiative recombination processes.

Further on, we performed μPL measurements with focused excitation within a temperature range of 5 to 70 K for randomly selected bright SCQDs within the pattern as well as for SAQDs outside the patterned area. Figure 2a,b shows typical sets of single QD emission spectra of a SCQD and a SAQD, respectively, at temperatures from 5 to 70 K. At high temperatures, only single exciton (X)-related peaks are visible in the spectrum, whereas at lower temperatures, also emission from biexciton and charged exciton states is observed. Figure 3 shows the peak energies of the exciton transitions (marked with X in Figure 2) for SCQD and SAQD as a function of temperature. The energies obey the temperature dependency of the InAs band gap energy as obtained by Varshni's law (solid lines), which is shifted in energy [18-20]. The integrated intensities of the single exciton PL for SCQD and SAQD are shown in the inset of Figure 3. The increase in intensity around 50 K is attributed to the increased amount of carriers transferred to the QD from the WL [16]. Figure 4 shows the linewidth of the exciton transition as a function of temperature calculated from Lorentzian fits to the exciton peak. The exciton linewidths for SCQD and SAQD show very similar temperature dependencies. At low temperatures, i.e., 5 to 30 K, the linewidth appears to be limited by the spectral resolution of 66 μeV of the measurement setup, but it increases rapidly to 250 μeV when increasing the temperature from 40 to 70 K. The

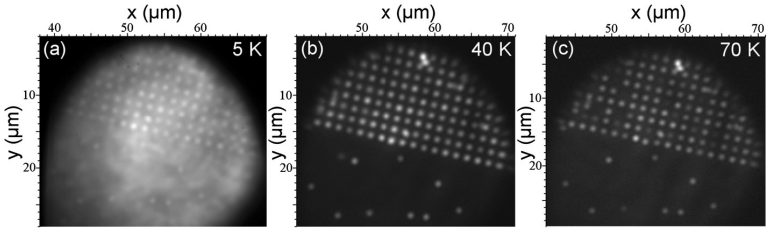

Figure 1 PL intensity images from the edge of the patterned area. Intensity within the spectral range of 850 to 1,000 nm was measured at temperatures of 5 K (**a**), 40 K (**b**), and 70 K (**c**). The excitation power and wavelength were 1.77 μW and 532 nm, respectively.

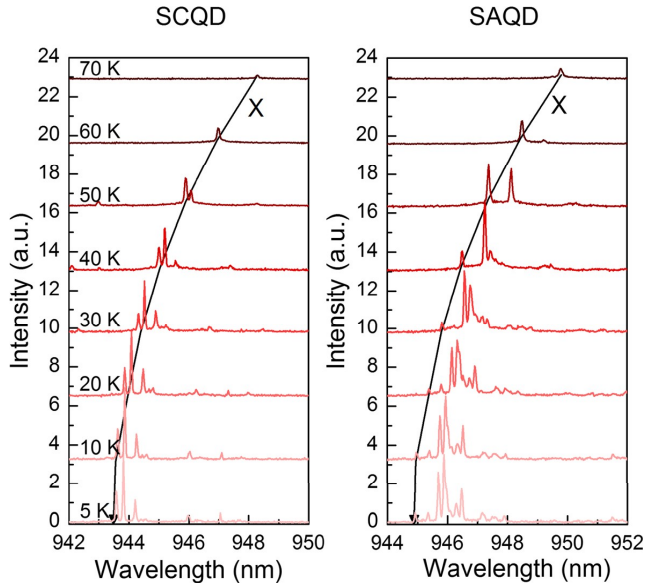

Figure 2 Single QD emission spectra for SCQD (a) and SAQD (b) at temperatures 5 to 70 K. The spectra are vertically shifted for clarity. The excitation power was 2 nW.

linewidth broadening is mainly caused by phonon scattering [21] and is in good agreement with previous results for SAQDs [22] and SCQDs [23,24].

Conclusions

We have studied the influence of temperature on the PL properties of single site-controlled InAs QDs fabricated by a combination of soft UV-NIL and MBE. We have shown that the QDs in etched holes emitting at 945 nm have temperature-dependent PL properties similar to the self-assembled QDs grown on planar surface. The PL properties indicate that the defects induced by the patterning do not degrade significantly the emission of the site-controlled QDs. Thus, soft UV-NIL-positioned QDs are considerable candidates for fabricating large-scale optoelectronic devices.

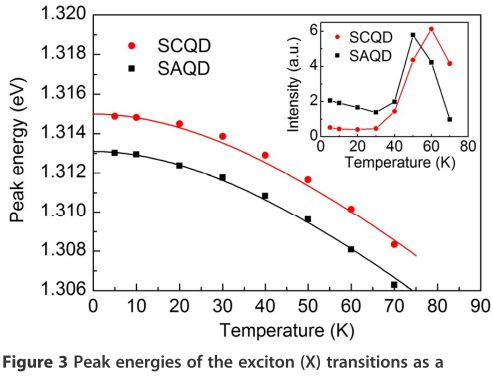

Figure 3 Peak energies of the exciton (X) transitions as a function of temperature. Solid lines indicate the slope of the temperature dependency of the InAs band gap energy obtained by Varshni's law. The parameters are $\alpha = 0.27$ meV/K and $\beta = 135$ K. The inset shows the integrated PL intensities of the exciton transitions.

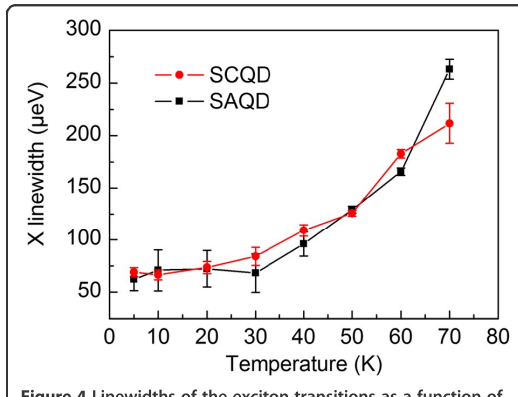

Figure 4 Linewidths of the exciton transitions as a function of temperature. The linewidths are obtained from Lorentzian fits to the exciton peak. Error bars indicate the error of Lorentzian fits.

Abbreviations

MBE: Molecular beam epitaxy; PL: Photoluminescence; μPL: Micro-photoluminescence; QD: Quantum dot; SAQD: Self-assembled quantum dot; SCQD: Site-controlled quantum dot; UV-NIL: Ultraviolet nanoimprint lithography; WL: Wetting layer; X: Single exciton.

Competing interests

The authors declare that they have no competing interests.

Authors' contributions

JT carried out UV-NIL patterning, participated in design and data analysis, and drafted the manuscript. AS and TVH carried out the MBE growths and participated in design. CS and TK performed the PL measurements. MD and MG conceived of the study and participated in its design and coordination. All authors read and approved the final manuscript.

Acknowledgments

The research was carried out within the Academy of Finland project DAUNTLESS (decision number 123951). JT acknowledges the National Doctoral Programme in Nanoscience (NGS-NANO), the Vilho, Yrjö and Kalle Väisälä Foundation and the Industrial Research Fund at Tampere University of Technology (Tuula and Yrjö Neuvo fund) for the financial support. AS acknowledges funding from the Academy of Finland within the project 138940. TVH acknowledges financial support from the Finnish National Graduate School in Materials Physics, Jenny and Antti Wihuri Foundation, and Finnish Foundation for Technology Promotion. CS and TK acknowledge funding from the Deutsche Forschungsgemeinschaft via project KI 1257/1.

Author details

[1]Optoelectronics Research Centre, Tampere University of Technology, Korkeakoulunkatu 3, Tampere, FIN-33720, Finland. [2]Institute of Physical Chemistry, University of Hamburg, Grindelallee 117, Hamburg 20146, Germany.

Received: 4 May 2012 Accepted: 6 June 2012
Published: 19 June 2012

References

1. Waks E, Inoue K, Santori C, Fattal D, Vuckovic J, Solomon GS, Yamamoto Y: **Quantum cryptography with a single photon turnstile.** *Nature* 2002, **420:**762.
2. Santori C, Fattal D, Vuckovic J, Solomon GS, Yamamoto Y: **Indistinguishable photons from a single-photon device.** *Nature* 2002, **419:**594–597.
3. Knill E, Laflamme R, Milburn GJ: **A scheme for efficient quantum computation with linear optics.** *Nature* 2001, **409:**46–52.
4. Michler P, Kiraz A, Becher C, Schoenfeld WV, Petroff PM, Zhang L, Hu E, Imamoğlu A: **A quantum dot single-photon turnstile device.** *Science* 2000, **290:**2282–2285.
5. Schneider C, Heindel T, Huggenberger A, Niederstrasser TA, Reitzenstein S, Forchel A, Höfling S, Kamp M: **Microcavity enhanced single photon emission from an electrically driven site-controlled quantum dot.** *Appl Phys Lett* 2012, **100:**091108–1–091108–4.
6. Salter CL, Stevenson RM, Farrer I, Nicoll CA, Ritchie DA, Shields AJ: **An entangled-light-emitting diode.** *Nature* 2010, **465:**594–597.
7. Mohan A, Felici M, Gallo P, Dwir B, Rudra A, Faist J, Kapon E: **Polarization-entangled photons produced with high-symmetry site-controlled quantum dots.** *Nat Photonics* 2010, **4:**302–306.
8. Martín-Sánchez J, Muñoz-Matutano G, Herranz J, Canet-Ferrer J, Alén B, González Y, Alonso-González P, Fuster D, González L, Martínez-Pastor J, Briones F: **Single photon emission from site-controlled InAs quantum dots grown on GaAs(001) patterned substrates.** *ACS Nano* 2009, **3:**1513–1517.
9. Felici M, Gallo P, Mohan A, Dwir B, Rudra A, Kapon E: **Site-controlled InGaAs quantum dots with tunable emission energy.** *Small* 2009, **5:**938–943.
10. Schneider C, Strauß M, Sünner T, Huggenberger A, Wiener D, Reitzenstein S, Kamp M, Höfling S, Forchel A: **Lithographic alignment to site-controlled quantum dots for device integration.** *Appl Phys Lett* 2008, **92:**183101–1–183101–3.
11. Wang Zh M, Seydmohamadi Sh, Lee JH, Salamo GJ: **Surface ordering of (In, Ga) As quantum dots controlled by GaAs substrate indexes.** *Appl Phys Lett* 2004, **85:**5031–5033.
12. Lee JH, Wang Zh M, Black WT, Kunets VP, Mazur YI, Salamo GJ: **Spatially localized formation of InAs quantum dots on shallow patterns regardless of crystallographic directions.** *Adv Funct Mater* 2007, **17:**3187–3193.
13. Tommila J, Tukiainen A, Viheriälä J, Schramm A, Hakkarainen TV, Aho A, Stenberg P, Dumitrescu M, Guina M: **Nanoimprint lithography patterned GaAs templates for site-controlled InAs quantum dots.** *J Cryst Growth* 2011, **323:**183–186.
14. Balzarotti A: **The evolution of self-assembled InAs/GaAs(001) quantum dots grown by growth-interrupted molecular beam epitaxy.** *Nanotechnology* 2008, **19:**505701.
15. Leon R, Fafard S: **Structural and radiative evolution in quantum dots near the $In_xGa_{1-x}As$/GaAs Stranski-Krastanow transformation.** *Phys Rev B* 1998, **58:**R1726–R1729.
16. Larsson LA, Larsson M, Moskalenko ES, Holtz PO: **Temperature and magnetic field effects on the transport controlled charge state of a single quantum dot.** *Nanoscale Res Lett* 2010, **5:**1150–1155.
17. Cho NK, Ryu SP, Song JD, Choi WJ, Lee JI, Jeon H: **Comparison of structural and optical properties of InAs quantum dots grown by migration-enhanced molecular-beam epitaxy and conventional molecular-beam epitaxy.** *Appl Phys Lett* 2006, **88:**133104–1–133104–3.
18. O'Donnell KP, Chen X: **Temperature dependence of semiconductor band gaps.** *Appl Phys Lett* 1991, **58:**2924–2926.
19. Vurgaftman I, Meyer JR, Ram-Mohan LR: **Band parameters for III–V compound semiconductors and their alloys.** *J Appl Phys* 2001, **89:**5815–5875.
20. Huang YS, Qiang H, Pollak FH, Pettit GD, Kirchner PD, Woodall JM, Stragier H, Sorensen LB: **Temperature dependence of the photoreflectance of a strained layer (001) $In_{0.21}Ga_{0.79}As$/GaAs single quantum well.** *J Appl Phys* 1991, **70:**7537–7542.
21. Ouerghui W, Melliti A, Maaref MA, Bloch J: **Dependence on temperature of homogeneous broadening of InGaAs/InAs/GaAs quantum dot fundamental transitions.** *Physica E* 2005, **28:**519–524.
22. Cade NI, Gotoh H, Kamada H, Nakano H, Anantathanasarn S, Nötzel R: **Optical characteristics of single InAs/InGaAsP/InP (100) quantum dots emitting at 1.55 μm.** *Appl Phys Lett* 2006, **89:**181113–1–181113–3.
23. Selçuk E, Yu Silov A, Nötzel R: **Single InAs quantum dot arrays and directed self-organization on patterned GaAs (311) B substrates.** *Appl Phys Lett* 2009, **94:**263108–1–263108–3.
24. Tran T, Muller A, Shih CK, Wong PS, Balakrishnan G, Nuntawong N, Tatebayashi J, Huffaker DL: **Single dot spectroscopy of site-controlled InAs quantum dots nucleated on GaAs nanopyramids.** *Appl Phys Lett* 2007, **91:**133104–1–133104–3.

doi:10.1186/1556-276X-7-313
Cite this article as: Tommila *et al.*: The influence of temperature on the photoluminescence properties of single InAs quantum dots grown on patterned GaAs. *Nanoscale Research Letters* 2012 **7**:313.

Publication 4

A. Schramm, J. Tommila, C. Sterlow, T.V. Hakkarainen, A. Tukiainen, M. Dumitrescu, A. Mews, T. Kipp and M. Guina, “Large array of single, site-controlled InAs quantum dots fabricated by UV-nanoimprint lithography and molecular beam epitaxy,” *Nanotechnology*, vol. 23, 175701 (4pp), 2012

P4

Nanotechnology **23** (2012) 175701 (4pp) doi:10.1088/0957-4484/23/17/175701

Large array of single, site-controlled InAs quantum dots fabricated by UV-nanoimprint lithography and molecular beam epitaxy

A Schramm[1], J Tommila[1], C Strelow[2], T V Hakkarainen[1], A Tukiainen[1], M Dumitrescu[1], A Mews[2], T Kipp[2] and M Guina[1]

[1] Optoelectronics Research Centre, Tampere University of Technology, PO Box 692 FIN-33101 Tampere, Finland
[2] Institute of Physical Chemistry, University of Hamburg, Grindelallee 117, DE-20146 Hamburg, Germany

E-mail: andreas.schramm@tut.fi

Received 20 December 2011
Published 5 April 2012
Online at stacks.iop.org/Nano/23/175701

Abstract
We present the growth of single, site-controlled InAs quantum dots on GaAs templates using UV-nanoimprint lithography and molecular beam epitaxy. A large quantum dot array with a period of 1.5 μm was achieved. Single quantum dots were studied by steady-state and time-resolved micro-photoluminescence experiments. We obtained single exciton emission with a linewidth of 45 μeV. In time-resolved experiments, we observed decay times of about 670 ps. Our results underline the potential of nanoimprint lithography and molecular beam epitaxy to create large-scale, single quantum dot arrays.

(Some figures may appear in colour only in the online journal)

1. Introduction

Coherently strained InAs quantum dots (QDs) are very promising candidates for developing components required in future information processing systems [1]. These applications are rendered possible by the unique properties of QDs, such as narrow emission linewidth and wide wavelength tunability [2, 3], the ability to emit single photons on demand [4], or the possibility to tune the carrier spins [5]. For novel devices, that exploit these advantageous features, the possibility to accurately control the lateral positions of individual QDs is highly desirable [6]. By applying molecular beam epitaxy this can be achieved by defining the nucleation sites for the impinging adatoms using patterning processes. Recently, great attention has been paid to devise suitable techniques in order to pattern substrates prior to the QD deposition, e.g., using electron beam lithography [6–12], focused ion beam techniques [13–15], atomic force microscope lithography [16], or exploiting strain-related effects in order to organize the QDs [17].

In our fabrication approach we use a combination of molecular beam epitaxy (MBE) and nanoimprint lithography (NIL), in particular its modification soft UV-NIL [18], for substrate patterning. Very recently, UV-NIL has been shown to be an attractive method for fabricating QD templates [19–21], since it is a low-cost, large-scale, high resolution nano-patterning technique [22] and offers large freedom of design. We report on the fabrication of large arrays of single site-controlled InAs QDs with nearest-neighbor distances that allow for an individual optical addressing. We study the PL emission of single site-controlled QDs with spatial, spectral, and temporal resolution. Our experiments show the possibilities of using UV-NIL and MBE for creating large arrays of single QDs with narrow linewidths.

2. Experimental procedures

The samples were grown on GaAs(100) substrates in a solid-source MBE system equipped with a valved cracker for As_2. After the growth of a GaAs buffer, an AlGaAs carrier

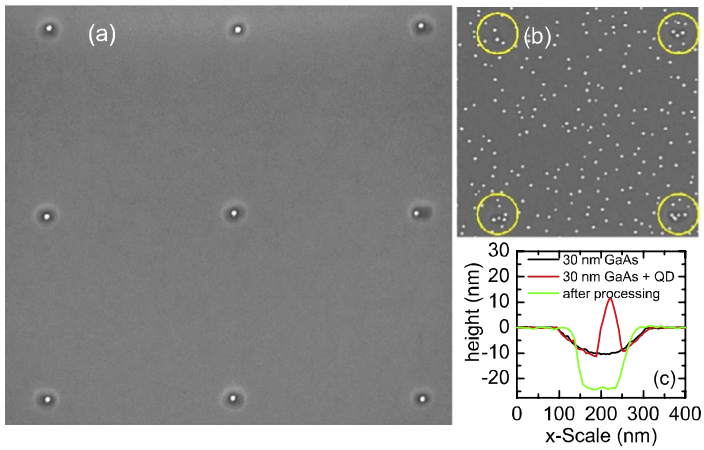

Figure 1. (a) SEM image of single InAs QDs grown in the growth-interrupted fashion on a NIL structured hole pattern with a period of 1.5 μm. (b) SEM image of a sample on which QDs were deposited continuously on a NIL structured hole pattern with a period of 1.5 μm. The yellow circles mark the positions of the NIL holes. (c) Linescans through the pre-defined holes after the 30 nm GaAs buffer layer either with or without an InAs QD and before the growth of the GaAs buffer layer, directly after processing.

blocking barrier, and a GaAs layer, the samples were taken out and the patterning was made by utilizing a soft UV-NIL process, which is described in detail in [23]. The silicon master for our NIL process consisted of circular holes of 100 nm in diameter in a square array with 1.5 μm period. The patterned area was 1×1 mm^2. The patterning process was performed with an EVG 620 mask aligner. The hole etching was based on BCl_3/Ar chemistry and inductively coupled plasma reactive ion etching (ICP-RIE). After the process, the final cleaning and native oxide removal was carried out by chemical treatments including isopropyl alcohol (IPA) rinse before and after the chemical etch with solutions of HCl, IPA and NH_4OH [23]. Prior to the overgrowth, the patterned samples were annealed in the MBE chamber at 590 °C for 5 min in order to thermally desorb the native oxide layer. For the growth of site-controlled InAs QDs, a 30 nm GaAs layer was deposited on top of the patterned structure at 470 °C. The QDs were grown in a growth-interrupted fashion [24] by depositing 1.8 monolayers of InAs in nine periods, each consisting of 4 s of growth and 2 s of growth interruption (GI) with an open arsenic valve, at 540 °C and with a growth rate of 0.05 μm h^{-1}. For PL studies, the QDs were subsequently capped by 20 nm and 50 nm GaAs grown at 540 °C and at 590 °C, respectively. The growth was finished by a 50 nm AlGaAs carrier blocking layer and a 10 nm GaAs cap layer. Surface QD samples without any capping layers, grown with exactly the same parameters as the sample with embedded QDs, were evaluated by scanning electron microscopy (SEM) and atomic force microscopy (AFM). Micro-PL measurements on capped samples with embedded QDs were performed with a home-built low-temperature laser-scanning confocal microscope. The sample was mounted in a closed-cycle optical cryostat allowing for temperatures between 4 and 100 K. For excitation, either a diode-pumped solid-state cw laser at 532 nm or a pulsed tunable Ti:sapphire laser with 75.4 MHz repetition rate and pulse lengths of 200–300 fs was used. Here, the wavelength was fixed at 850 nm in order to fill the QDs via quasi-resonant excitation into the wetting layer. The excitation light was brought onto the sample through a microscope objective (100×, NA = 0.8) either as a diffraction-limited spot or widened up by an additional lens for wide-field illumination. The PL light was collected by the same objective and brought either to a 0.5 m spectrograph equipped with a Peltier-cooled CCD camera for spectroscopy and wide-field imaging, or to an avalanche photodiode for time correlated single photon counting (TCSPC) for time-resolved measurements. The time resolution of the system measured as the FWHM of the laser signal was 80 ps. The spectrograph contained dispersive gratings as well as an optional mirror for imaging. For imaging and time-resolved measurements, optical filters allowed selection of a wavelength range of interest and cut off the scattered laser light as well as the GaAs bulk emission before detection.

3. Results and discussion

For a first overview, we present the topographical results of two surface samples, i.e., QD samples without any capping layers. In figure 1(a) we show a SEM image of site-controlled QDs which are arranged in a square lattice of 1.5 μm period, each singly occupying one pre-defined hole. From a very large-scale SEM image (not shown here) displaying 315 NIL structured holes, we observe that more than 90% of the holes are occupied by a single QD. In order to achieve low-density, single site-controlled QDs, their areal density has to match the areal density of the prepatterned holes, i.e., in our case, 3.6×10^7 cm^{-2}. This was accomplished by the above described growth procedure in which indium desorption [25] and ripening effects [24] during the growth interruptions strongly

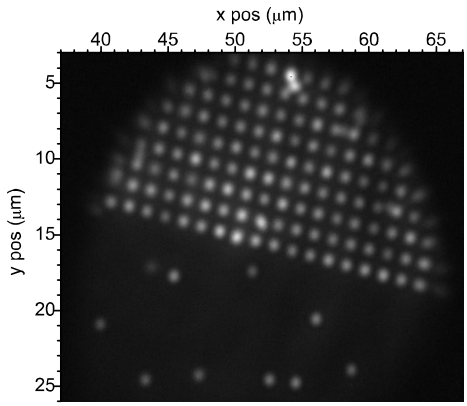

Figure 2. Large-scale PL image of single QDs with a period of 1.5 μm at the edge of the patterned area obtained at $T = 40$ K with an excitation power and wavelength of 1.77 μW and 532 nm, respectively.

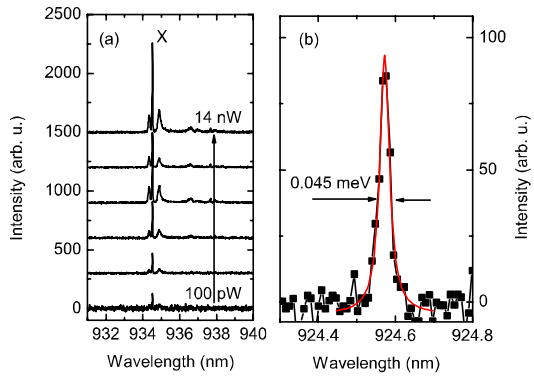

Figure 3. (a) Power-dependent micro-PL spectra of a single QD at $T = 4.7$ K. The spectra are vertically shifted for clarity. (b) Linewidth of an exciton emission.

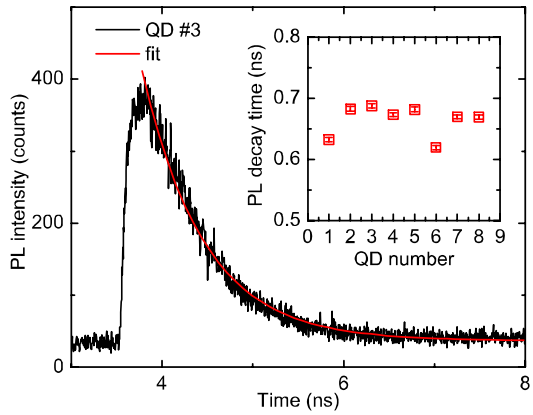

Figure 4. Time-resolved micro-PL measurements of a single, site-controlled QD. The red line is single exponential fits to the measurements. The inset shows the PL decay times of several site-controlled QDs obtained from single exponential fits. The excitation wavelength and power were 850 nm and 350 nW, respectively.

reduced the QD density. For comparison, figure 1(b) shows a sample on which the QDs were deposited continuously resulting in a QD density of 5.5×10^9 cm^{-2}. Here, several QDs are occupying each prepatterned hole (marked by circles) and a large number of QDs lie between the holes. Figure 1(c) depicts a linescan of a single site-controlled QD together with linescans (i) after patterning but before the overgrowth with GaAs and (ii) after the 30 nm GaAs buffer regrowth but before QD deposition. Before regrowth the holes exhibit a depth of about 25 nm and a maximum diameter of 100 nm. After the regrowth step the depth and diameter have changed to about 10 nm and 200 nm, respectively. From the QD linescans we observe that not all QDs are growing in the center of the hole, which can be explained by a slightly increased number of monolayer steps at the sidewalls due to faceting. This enhances the accumulation of indium atoms closer to the walls than the center and results in off-centered QDs.

In the following we assess the optical properties of the site-controlled QDs by means of micro-PL techniques. In figure 2(a) we present a spatially resolved PL image of the embedded QDs, close to the edge of the patterned area, grown with exactly the same parameters as the sample with surface QDs in figure 1(a). The PL image was obtained by a wide-field illumination for excitation and by imaging the PL light between 850 and 1000 nm onto the CCD camera. This method enables us to observe PL emission from each individual QD over an area as large as 25 μm in diameter. The optical QD array nearly perfectly reproduces the patterned array. Only a very few light spots occur within the pre-defined regular pattern. The intensity of the QDs in the patterned area shows variations due to the statistical nature of the QDs. Furthermore, the used temperature of 40 K may lead to slight differences in non-radiative losses of each individual QD. However, this temperature was the best compromise between reducing PL emission from the wetting layer and displaying that all QDs are optically active. Removing the widening lens before the microscope objective and using the laser scanner we were able to perform confocal spectroscopy on individual QDs inside the patterned area.

Power-dependent micro-PL spectra of an individual site-controlled QD are shown in figure 3(a). A narrow line, arising from the exciton (X) is observed at the lowest excitation power of 0.1 nW. Increasing the excitation power leads to the evolution of multiple PL lines in the spectra, typical for single QDs [26]. A typical exciton linewidth as obtained in figure 3(b) is 45 μeV which is in the range of previously reported results of site-controlled grown InAs QDs on e-beam patterned GaAs templates [11, 12].

In order to further evaluate the optical quality of the site-controlled QDs we employed time-resolved micro-PL measurements. In figure 4 we show the results from TCSPC measurements on a single QD in the array. In these experiments, by using a 925 nm long-pass filter in front of the avalanche photodiode, only the light from the s shell

of the QD is measured. The temporal PL behavior of the s-shell emission can be sufficiently approximated by a single exponential function with one decay time. In figure 4 we obtain a typical decay time of 682 ps for the site-controlled QD. In order to improve the statistics, we measured the decay times of nine QDs inside the array as shown in the inset of figure 4. All QDs have similar decay times close to the average of 669 ps that are in correspondence with previous reports about self-assembled, single QDs [26, 27] and self-assembled QD ensembles [28–30]. The slight differences of decay times again arise from the statistical nature of the QDs. In general, measurements of the decay times should represent a sensitive method to disclose structural differences between QDs since these differences should impact the non-radiative recombination channels. Our experiment shows that the patterning process does not significantly influence the QD PL dynamics with respect to self-assembled QDs [26, 27]. This proves the suitability of UV-NIL and MBE as a promising combination for the fabrication of site-controlled single QDs of high optical quality.

4. Conclusion

In conclusion, the growth of a large array of site-controlled, single InAs QDs on UV-NIL prepared GaAs templates was demonstrated. The site-controlled QDs were arranged in a square lattice of 1.5 μm period. Single quantum dots were studied by spatially resolved and power-dependent micro-PL experiments proving the high optical quality of the site-controlled InAs QDs with typical emission spectra and exciton linewidths of about 45 μeV. Time-resolved micro-PL experiments revealed similar temporal behavior for site-controlled quantum dots with respect to self-assembled ones in the literature. The optical quality, the spacing and the regularity of our site-controlled QDs, achieved by the combination of UV-NIL and MBE, indicate the possibility of creating large arrays of single quantum emitters, which could be a basis for advanced optoelectronic quantum devices.

Acknowledgments

The authors acknowledge funding from the Academy of Finland via Dauntless (123951) and Droplet (138940) and from the Finnish National Graduate Schools in Materials Physics and Nanotechnology. We thank Stefanie Kietzmann for help during the optical measurements. CS and TK acknowledge funding from the Deutsche Forschungsgemeinschaft via project KI 1257/1.

References

[1] Grundmann M 2002 *Nano-Optoelectronics* (Berlin: Springer)
[2] Grundmann M, Christen J, Ledentsov N N, Böhrer J and Bimberg D 1995 *Phys. Rev. Lett.* **74** 4043
[3] Zrenner A 2000 *J. Chem. Phys.* **112** 7790
[4] Yuan Z, Kardynal B, Stevenson R, Shields A, Lobo C, Cooper K, Beattie N, Ritchie D and Pepper M 2002 *Science* **295** 102
[5] Cortez S, Krebs O, Laurent S, Senes M, Marie X, Voisin P, Ferreira R, Bastard G, Gérard J M and Amand T 2002 *Phys. Rev. Lett.* **89** 207401
[6] Schmidt O G 2007 *Lateral Alignment of Epitaxial Quantum Dots* (Berlin: Springer)
[7] Ishikawa T, Nishimura T, Kohmoto S and Asakawa K 2000 *Appl. Phys. Lett.* **76** 167
[8] Schneider C, Strauß M, Sünner T, Huggenberger A, Wiener D, Reitzenstein S, Kamp M, Höfling S and Forchel A 2008 *Appl. Phys. Lett.* **92** 183101
[9] Atkinson P, Kiravittaya S, Benyoucef M, Rastelli A and Schmidt O G 2008 *Appl. Phys. Lett.* **93** 101908
[10] Mereni L O, Dimastrodonato V, Young R J and Pelucchi E 2009 *Appl. Phys. Lett.* **94** 223121
[11] Huggenberger A, Heckelmann S, Schneider C, Höfling S, Reitzenstein S, Worschech L, Kamp M and Forchel A 2011 *Appl. Phys. Lett.* **98** 131104
[12] Skiba-Szymanska J *et al* 2011 *Nanotechnology* **22** 065302
[13] Karmous A, Cuenat A, Ronda A, Berbezier I, Atha S and Hull R 2004 *Appl. Phys. Lett.* **85** 6401
[14] Mehta M, Reuter D, Melnikov A, Wieck A D and Remhof A 2007 *Appl. Phys. Lett.* **91** 123108
[15] Lee J Y, Noordhoek M J, Smereka P, McKay H and Millunchick J M 2009 *Nanotechnology* **20** 285305
[16] Hyon C K, Choi S C, Song S H, Hwang S W, Son M H, Ahn D, Park Y J and Kim E K 2000 *Appl. Phys. Lett.* **77** 2607
[17] Hakkarainen T, Schramm A, Tukiainen A, Ahorinta R, Toikkanen L and Guina M 2010 *Nanoscale Res. Lett.* **5** 1892
[18] Viheriälä J, Viljanen M R, Kontio J, Leinonen T, Tommila J, Dumitrescu M, Niemi T and Pessa M 2009 *J. Micro/Nanolith. MEMS MOEMS* **8** 033004
[19] Cheng C C, Meneou K and Cheng K Y 2009 *Appl. Phys. Lett.* **95** 173108
[20] Hakkarainen T, Tommila J, Schramm A, Tukiainen A, Ahorinta R, Dumitrescu M and Guina M 2010 *Appl. Phys. Lett.* **97** 173107
[21] Lausecker E, Brehm M, Grydlik M, Hackl F, Bergmair I, Mühlberger M, Fromherz T, Schäffler F and Bauer G 2011 *Appl. Phys. Lett.* **98** 143101
[22] Viheriälä J, Rytkönen T, Niemi T and Pessa M 2008 *Nanotechnology* **19** 015302
[23] Tommila J, Tukiainen A, Viheriälä J, Schramm A, Hakkarainen T, Aho A, Stenberg P, Dumitrescu M and Guina M 2011 *J. Cryst. Growth* **323** 183
[24] Balzarotti A 2008 *Nanotechnology* **19** 505701
[25] Heyn C 2002 *Phys. Rev.* B **66** 075307
[26] Thompson R M, Stevenson R M, Shields A J, Farrer I, Lobo C J, Ritchie D A, Leadbeater M L and Pepper M 2001 *Phys. Rev.* B **64** 201302(R)
[27] Santori C, Solomon G S, Pelton M and Yamamoto Y 2002 *Phys. Rev.* B **65** 073310
[28] Colocci M, Vinattieri A, Lippi L, Bogani F, Rosa-Clot M, Taddei S, Bosacchi A, Franchi S and Frigeri P 1999 *Appl. Phys. Lett.* **74** 564
[29] Malik S, Ru E C L, Childs D and Murray R 2001 *Phys. Rev.* B **63** 155313
[30] Langbein W, Borri P, Woggon U, Stavarache V, Reuter D and Wieck A D 2004 *Phys. Rev.* B **70** 033301

Publication 5

J. Tommila, V. Polojärvi, A. Aho, A. Tukiainen, J. Viheriälä, J. Salmi, A. Schramm, J. M. Kontio, A. Turtiainen, T. Niemi and M. Guina, "Nanostructured broadband antireflection coatings on AlInP fabricated by nanoimprint lithography," *Solar Energy Materials and Solar Cells*, vol. 94, no. 10, pp. 1845-1848, 2010.

Nanostructured broadband antireflection coatings on AlInP fabricated by nanoimprint lithography

J. Tommila, V. Polojärvi, A. Aho, A. Tukiainen, J. Viheriälä, J. Salmi, A. Schramm, J. M. Kontio, A. Turtiainen, T. Niemi and M. Guina

Optoelectronics Research Centre, Tampere University of Technology, FIN-33101 Tampere, Finland

Abstract

We report the fabrication of moth-eye antireflection nanostructures on AlInP compound commonly used as a window layer in high efficiency multijunction solar cells. The broadband antireflective nanostructures were fabricated by nanoimprint lithography directly on molecular beam epitaxy grown AlInP/GaAs surface. At normal incidence the structures exhibited an average reflectivity of 2.7 % measured in a spectral range from 450 nm to 1650 nm. Photoluminescence measurements of the emission from GaAs substrate suggest that the optical losses associated with the moth-eye pattern are low. Nanoimprint lithography offers a cost-effective approach to fabricate broadband antireflection coatings required in III-V high-efficiency multijunction solar cells.

Keywords

Nanoimprint lithography, multijunction photovoltaic cell, antireflection coating, moth-eye

1. Introduction

The deployment of high-efficiency multijunction III-V semiconductor solar cells (SCs) in terrestrial solar power plants has attracted increasing interest in the past few years, owing to the development of advanced solar concentrator systems that are able to meet grid parity. Conversion efficiencies of more than 40 % have been demonstrated for three-junction III-V cells using concentrators [1,2] and higher efficiencies are predicted for cells with more than three junctions [3]. Due to the exploitation of multiple absorption bands, such devices exhibit a wide absorption spectrum ranging from 300 nm to beyond 1800 nm. To fully exploit the potential of multijunction cells broadband antireflection (AR) coatings should be employed to mitigate the high discontinuity of refractive index at the semiconductor-air interface. In addition to the requirement for broader AR coatings, multijunction solar cells are more sensitive than single-junction cells to variation of the reflectivity because of current matching requirements; deviation of the coating from the optimum reflectance results in increased current mismatch. The optimization of widely used dielectric multilayer interference structures for use as AR coatings in high efficiency III-V solar cells is therefore challenging [1,4-7]. A more recent approach to fabricate broadband AR coatings is to exploit the so called moth-eye concept and fabricate sub-wavelength nanostructures on the surface of the SC [8,9]. This type of nanostructure provides a graded transition of the effective refractive index between the air and semiconductor surface, and thus, decreases effectively the amount of reflected light in a broad wavelength range and at all angles [8,9]. Moth-eye AR

structures have been fabricated on silicon, GaAs, and GaSb substrates [9-12], however no estimations of the losses in these structures were reported.

In this letter, we demonstrate moth-eye antireflection coatings fabricated by high-resolution low-cost nanoimprint lithography (NIL) on molecular beam epitaxy (MBE) grown AlInP/GaAs structure. AlInP has a very large band gap and high transparency. Therefore, it is usually added as a front window on III-V multijunction SC in order to passivate the emitter [1]. We show that the reflection from the AlInP/air interface can be strongly suppressed by using nanopatterned surfaces. Additionally, we present a method to estimate the losses caused by the surface pattern. Minimizing the losses in the nanostructure is essential in order to reach high-efficiencies by maximizing the transmission of light to the absorbing layers.

2. Material and methods

The semiconductor layers were deposited by molecular beam epitaxy (MBE). First, a 100 nm GaAs buffer was grown on n-type GaAs(100) substrate at a growth temperature of T_{sub}=580 ^{o}C. Then the temperature was lowered to T_{sub}=480 ^{o}C and a 1 µm thick AlInP layer was grown. The moth-eye nanopatterns were fabricated by means of soft UV-nanoimprint lithography (UV-NIL). Details of the technique can be found elsewhere [13,14]. The master template consisted of nanocones in a square array with a period of 300 nm, height of 190 nm and base diameter of 130 nm. The nanocones were fabricated by lift-off process described in [14]. We used SiN_x as an etch mask for AlInP etching. The cone pattern was transferred from imprinted UV-NIL resist (AMONIL, AMO GmbH) to the SiN_x using dry etching and CHF_3/Ar based chemistry. Inductively

coupled plasma reactive ion etching (ICP-RIE, Oxford Instruments Plc) was utilized for AlInP etching. The measures of the resulting AlInP cones were (top diameter/base diameter/height) 30/170/370 nm (sample A), 50/220/370 nm (sample B), and 80/300/440 nm (sample C). Fig. 1 shows the scanning electron microscope (SEM) images of AlInP nanocones corresponding to the samples A, B and C, respectively. The dimensions were tuned by changing the etching conditions. The AlInP etching was based on $Cl_2/N_2/Ar$ chemistry and it was performed at low pressure of 3.0 mTorr and elevated temperature of 200 ^{o}C. The gas flows for $Cl_2/N_2/Ar$ were 10/15/2 sccm, respectively. The applied RIE chuck power was 50 W and the ICP source power was 750 W. Sample A was etched in one ICP-RIE step, whereas sample B had three and sample C had six separate etch steps with the same etching conditions. The base diameter of the cones was increased by repeating the short (20 – 40 s) etch steps. The broadening of the base was due to the passivation of the cone walls, especially between the steps, and is less present for the single step process (sample A). The residual AlInP layer under the cones was measured from the cross sections by SEM and varied between 500 and 700 nm for the three samples. In addition, we fabricated one un-etched reference structure consisting of 1 μm AlInP layer on top of a GaAs substrate.

The reflectivity of the samples was measured at normal incidence by using broadband light source and a CCD (for the spectral range from 450 nm to 1100 nm) or an InGaAs detector array (for the spectral range from 1000 nm to 1650 nm) and a silver mirror for the reflectivity calibration. The reflectance spectra were measured by Accent RPM2000 photoluminescence (PL) and reflectance mapping tool. The reflectance of the moth-eye structures with sub-wavelength periodicity is often modeled by a uniform layer

with a graded index of refraction. The graded index can be approximated, for example, by calculating the volume fraction of the high-index material in thin vertical slices of the cone layer [10-12]. This approximation leads to the modeling of the layer as a stack of thin films which is a relatively straightforward structure to calculate. We decided to simulate the reflectance spectra using a finite-difference time-domain (FDTD) method [15] which allows us to apply parameters of the fabricated structures without effective index approximations.

3. Results and discussion

Fig. 2 shows the measured (solid lines) reflectance spectra at normal incidence for the samples A, B, and C, and for the un-etched reference sample. The reference sample exhibits an average reflectivity of 26.4 % over the measured spectral range. The lowest reflectivity was observed for the sample C with an average reflectivity of only 2.7 %. Sample C has no flat area between the nanocones, and therefore has graded refractive index without remarkable discontinuity when moving from the air to the semiconductor. Sample A exhibits an average reflectivity of 14.6 %. Even though the reflection is clearly suppressed, the small base diameter and flat areas between the nanocones leads to reflection. The cone height is the same in the samples A and B but the flat area is decreased by almost 25 % in the sample B and its mean reflectivity is 8.9 %. The reflectivity of the sample C was also measured at an angle of 21 degrees from the normal incidence for the spectral range from 500 nm to 1000 nm. The measured reflectivity at this small angle did not show any clear deviation from the reflectivity at normal incidence

which is in good agreement with the angle-dependent reflectivity measurements by Q. Chen *et al*. [9].

Dashed lines in Fig. 2 show the simulated reflectance spectra for each of the samples. The FDTD simulations were performed using the spatial dimensions measured by SEM and atomic force microscope (AFM). The materials were modeled for the simulations by fitting imaginary dielectric functions to the measured permittivities. The permittivity of AlInP was derived from the refractive index and extinction coefficient measured by a spectroscopic ellipsometer. The measured data and a schematic illustration of one block of the simulated structure used for sample C are shown in Fig. 3. In the simulation, the blocks were repeated periodically in the lateral dimensions. The dielectric function of GaAs was modeled using the data from [16]. The arithmetic average values for the spectral range from 450 nm to 1650 nm for simulated reflectivities and the corresponding measured values are summarized in Table 1. All the measurements agree well with the simulated results being in the range of one to two percentage units from the corresponding measurements. The simulated values are lower than the measured ones partly due to the silver mirror used as a reference in the measurements. Other main factors that could lead to differences between the simulations and measurements are the imperfect model of the dielectric function near the edge of the absorption band and the roughness of the etched surfaces.

To estimate the losses associated with the moth-eye nanostructure we measured the photoluminescence signal emitted from the underlying GaAs substrate. The PL spectra were measured by the same Accent RPM2000 which was used for the reflectivity measurements. The standard methods to assess the losses of thin films by measuring the

reflection and transmission cannot be directly used for materials with high absorption. In the case of GaAs substrate the absorption is high at wavelengths below 870 nm. In addition, the measurement of the transmission would require the use of polished substrates. Fig. 4(a) and 4(c) show the average GaAs PL spectra for the sample C and the reference sample using excitation wavelengths 785 nm and 532 nm, respectively. For both excitation wavelengths the measured PL intensity is higher for the nanostructured sample C than for the reference structure confirming the AR property of the surface. In order to estimate the losses in the nanostructure we equalized the PL intensities for the two excitation wavelengths. We took into account the reflections from the surface and the material losses within the AlInP layer. The equalized PL intensity can be written as:

$$I_{PL}^{eq}(\lambda) = \frac{I_{PL}^{meas}(\lambda)}{1-R_{laser}} \times \frac{1}{1-R(\lambda)} \times \frac{1}{\exp\left[-(\alpha_{laser}+\alpha_{PL})x\right]}. \qquad (1)$$

The first term on the right hand side takes into account the reflection of the laser used in excitation. The second term takes into account the wavelength dependent reflectivity for the PL light emitted from the GaAs layer. The measured reflectivities shown in Fig. 2 were used. The last term takes into account the absorption of the excitation laser light and the emitting PL light in the AlInP layer. The absorption coefficients in AlInP for the laser light α_{laser} and the PL light α_{PL} have been derived from the extinction coefficient κ using

$$\alpha_{laser,PL}(\lambda) = 4\pi\kappa(\lambda)/\lambda, \qquad (2)$$

where λ is either the excitation wavelength or the PL wavelength. The extinction coefficient was measured with a spectroscopic ellipsometer. The effective thickness x of the AlInP layer is 30 % thinner in the sample C than in the reference sample. It was estimated as a volume fraction between the nanostructured AlInP layer and the uniform layer.

After the equalization the PL spectra from the reference sample and the nanostructured sample C are almost similar as shown in Fig. 4(b) and 4(d). This is indeed expected if the absorption corresponding to the AlInP layer is the only loss mechanism leading to the difference between the reference and moth-eye structure. The larger difference for the equalized PL signals corresponding to 532 nm excitation (Fig. 4(d)) as compared to excitation at 785 nm (Fig. 4(b)) may be attributed to the approximations made on determining the effective thickness of the AlInP layer and to increased surface effects, such as scattering and surface recombination. Furthermore, we can conclude that, although the surface area has increased by more than a factor of three, the patterning does not cause remarkable losses, which would be seen as a large difference between the equalized PL spectra shown in Fig. 4(b) and 4(d). In the PL measurements the light is transmitted twice through the nanostructure in contrast to a single transmission of sunlight through the AR structure in SC applications. Thus, the patterning induced losses are expected to be lower in SC applications than observed in the PL measurement. We also point out that the sample C contains more than 500 nm of bulk AlInP beneath the nanocones. This residual layer could be significantly thinner in an optimized solar cell design to decrease the material losses for the short wavelength range of the solar spectrum.

4. Conclusion

We have demonstrated UV-NIL patterned moth-eye AR coatings on AlInP/GaAs semiconductor surface. An average reflectivity of 2.7 % was achieved for wide spectral range of 450 nm – 1650 nm. FDTD simulations correlate well with the measured

reflectance spectra. Using PL measurements we have shown that the surface recombination and patterning induced losses are low. Future work will focus on assessing the performance of tandem III-V solar cells comprising NIL-based moth-eye AR coatings patterned onto the AlInP window layer.

Acknowledgments

The work is supported by the Finnish Funding Agency for Technology and Innovation (TEKES) project Solar III-V (#40120/09). J. Tommila acknowledges the National Graduate School in Nanoscience (NGS-NANO) and the Pirkanmaa Regional Fund of the Finnish Cultural Foundation for the financial support. J. M. Kontio acknowledges the graduate school of Tampere University of Technology.

References

[1] W. Guter, J. Schöne, S. P. Philipps, M. Steiner, G. Siefer, A. Wekkeli, E. Welser, E. Oliva, A. W. Bett, F. Dimroth, Current-matched triple-junction solar cell reaching 41.1% conversion efficiency under concentrated sunlight, Appl. Phys. Lett. 94 (2009) 223504.

[2] R. R. King, D. C. Law, K. M. Edmondson, C. M. Fetzer, G. S. Kinsey, H. Yoon, R. A. Sherif, N. H. Karam, 40% efficient metamorphic GaInP/GaInAs/Ge multijunction solar cells, Appl. Phys. Lett. 90 (2007) 183516.

[3] R. R. King, D. C. Law, K. M. Edmondson, C. M. Fetzer, G. S. Kinsey, H. Yoon, D. K. Krut, J. H. Ermer, R. A. Sherif, N. H. Karam, Advances in High-Efficiency III-V Multijunction Solar Cells, Advances in OptoElectronics 2007 (2007) 29523.

[4] A. Luque, S. Hegedus, Handbook of Photovoltaic Science and Engineering, John Wiley & Sons, 2003.

[5] C. E. Valdivia, E. Desfonds, D. Masson, S. Fafard, A. Carlson, J. Cook, T. J. Hall, K. Hinzer, Optimization of antireflection coating design for multi-junction solar cells and concentrator systems, Proceedings of SPIE - The International Society for Optical Engineering 7099 (2008) 709915-1.

[6] D. J. Aiken, High performance anti-reflection coatings for broadband multi-junction solar cells, Solar Energy Materials & Solar Cells 64 (2000) 393-404.

[7] M. F. Schubert, F. W. Mont, S. Chhajed, D. J. Poxson, J. K. Kim, E. F. Schubert, Design of multilayer antireflection coatings made from co-sputtered and low-refractive-index materials by genetic algorithm, Opt. Express 16 (2008) 5290-5298.

[8] P. B. Clapham, M. C. Hutley, Reduction of Lens Reflection by the “Moth Eye” Principle, Nature (London) 244 (1973) 281-282.

[9] Q. Chen, G. Hubbard, P. A. Shields, C. Liu, D. W. E. Allsopp, W. N. Wang, S. Abbott, Broadband moth-eye antireflection coatings fabricated by low-cost nanoimprinting, Appl. Phys. Lett. 94 (2009) 263118.

[10] C.-H. Sun, P. Jiang, B. Jiang, Broadband moth-eye antireflection coatings on silicon, Appl. Phys. Lett. 92 (2008) 061112.

[11] C.-H. Sun, B. J. Ho, B. Jiang, P. Jiang, Biomimetic subwavelength antireflective gratings on GaAs, Opt. Lett. 33 (2008) 2224-2226.

[12] W.-L. Min, A. P. Betancourt, P. Jiang, B. Jiang, Bioinspired broadband antireflection coatings on GaSb, Appl. Phys. Lett. 92 (2008) 141109.

[13] J. Viheriälä, J. Tommila, T. Leinonen, M. Dumitrescu, L. Toikkanen, T. Niemi, M. Pessa, Applications of UV-nanoimprint soft stamps in fabrication of single-frequency diode lasers, Microelectron. Eng. 86 (2009) 321-324.

[14] J. M. Kontio, J. Simonen, J. Tommila, M. Pessa, Arrays of metallic nanocones fabricated by UV-nanoimprint lithography, Microelectron. Eng. 87 (2010) 1711-1715.

[15] F. Oskooi, D. Roundy, M. Ibanescu, P. Bermel, J. D. Joannopoulos, S. G. Johnson, MEEP: A flexible free-software package for electromagnetic simulations by the FDTD method, Computer Physics Communications 181 (2010) 687-702.

[16] S. Zollner, Optical constants and critical-point parameters of GaAs from 0.73 to 6.60 eV, J. of Appl. Phys. 90 (2001) 515-517.

Tables

Table 1. Measured and simulated arithmetic average reflectivities for the spectral range from 450 to 1650 nm for the reference sample and nanostructured samples.

	Reference	**A**	**B**	**C**
Simulation	25.3%	13.6%	6.7%	1.7%
Measurement	26.4%	14.6%	8.9%	2.7%

Figures

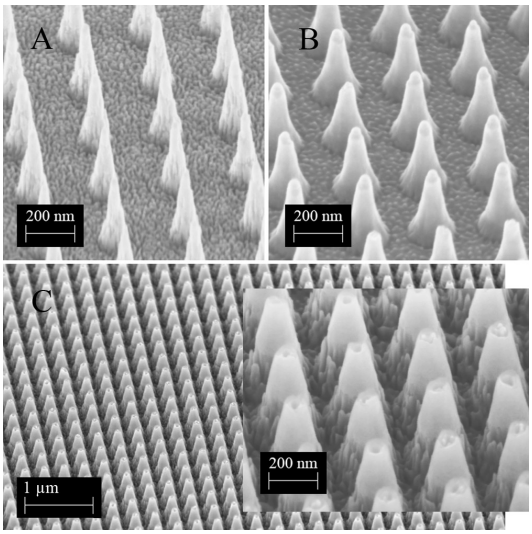

Fig. 1. Scanning electron microscope images of the AlInP nanocones on the samples A, B and C.

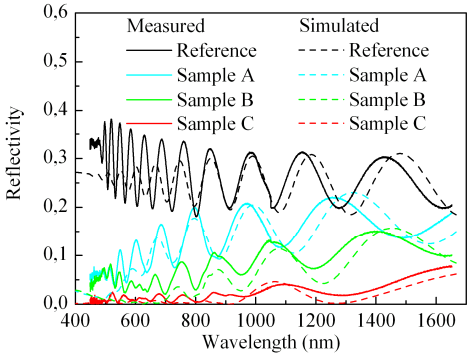

Fig. 2. Measured (solid lines) and simulated (dashed lines) reflectance spectra for the samples A, B, C and the reference sample.

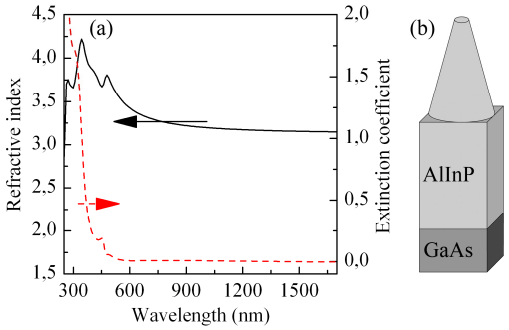

Fig. 3. (a) Measured refractive index (solid line) and extinction coefficient (dashed line) for AlInP. (b) A schematic illustration of the simulated structure used for sample C.

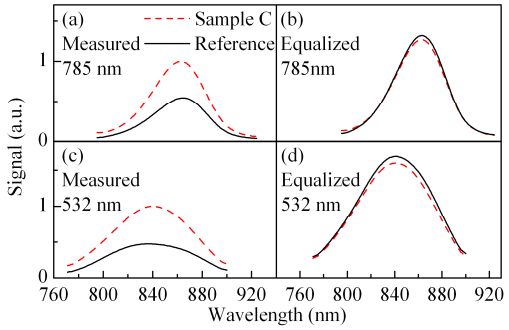

Fig. 4. Measured and equalized (Equation (1)) PL intensities for excitation at 785 nm (a), (b) and at 532 nm (c), (d).

Publication 6

J. Tommila, A. Aho, A. Tukiainen, V. Polojärvi, J. Salmi, T. Niemi and M. Guina, “Moth-eye antireflection coating fabricated by nanoimprint lithography on 1 eV dilute nitride solar cell,” *Progress in Photovoltaics: Research and Applications*, vol. 21, no. 5, pp. 1158–1162, 2013.

Tampereen teknillinen yliopisto
PL 527
33101 Tampere

Tampere University of Technology
P.O.B. 527
FI-33101 Tampere, Finland

ISBN 978-952-15-3139-2
ISSN 1459-2045